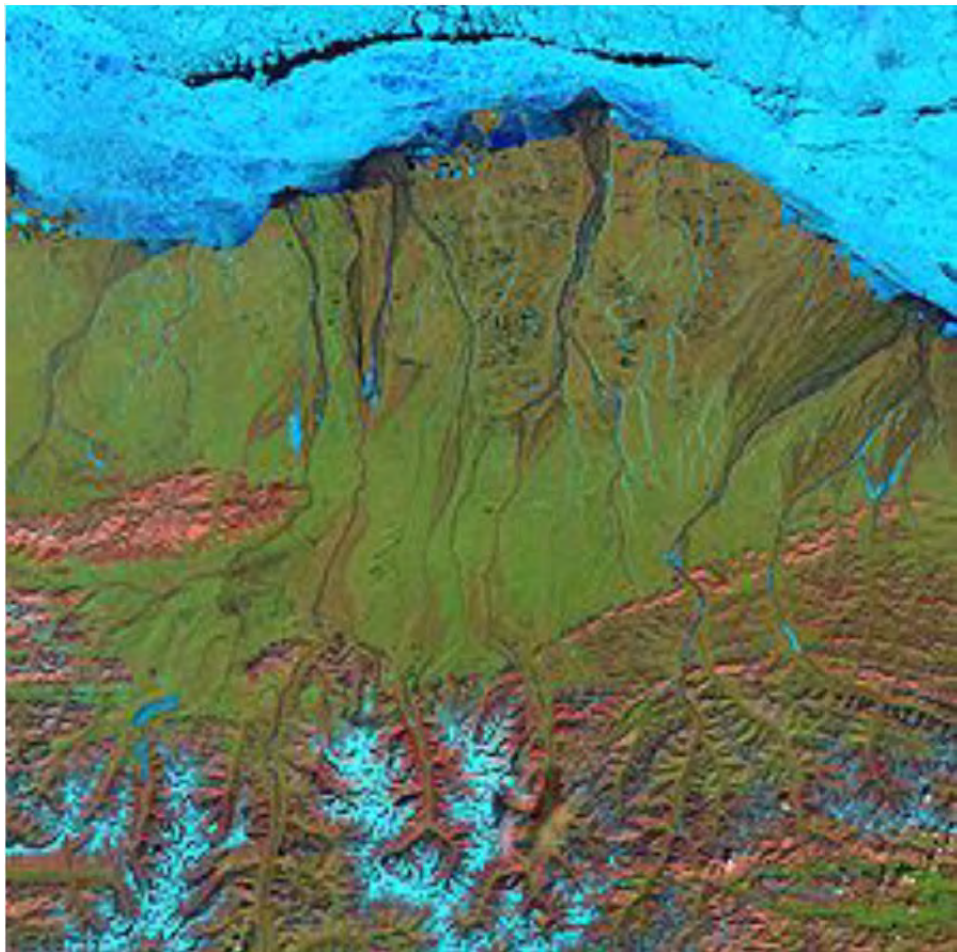


Adaptation of an Arctic Circulation Model



U.S. Department of the Interior
Bureau of Ocean Energy Management
Name of Region
www.boem.gov

Adaptation of an Arctic Circulation Model

**Enrique N. Curchitser, Rutgers University, New Brunswick, NJ
Kate Hedstron, University of Alaska, Fairbanks, AK
Seth Danielson, University of Alaska, Fairbanks, AK
Tom Weingartner, University of Alaska, Fairbanks, AK**

**Prepared under BOEM Contract
M10PC00116
by
Rutgers University
14 College Farm Road
New Brunswick, NJ 08901**

**Published by
U.S. Department of the Interior
Bureau of Ocean Energy Management
Headquarters, Environmental Studies Program**

**Herndon, VA
August, 2013**

DISCLAIMER

This report was prepared under contract between the Bureau of Ocean Energy Management (BOEM) and Rutgers University. This report has been technically reviewed by BOEM, and it has been approved for publication. Approval does not signify that the contents necessarily reflect the views and policies of BOEM, nor does mention of trade names or commercial products constitute endorsement or recommendation for use. It is, however, exempt from review and compliance with BOEM editorial standards.

REPORT AVAILABILITY

The report is available in compact disc format from the Bureau of Ocean Energy Management, Environmental Studies Program, at the address below at no charge by referencing OCS Study BOEM 2013-202, or it may be downloaded from the boem.gov website through the [Environmental Studies Program Information System \(ESPIS\)](#). You may inspect copies at selected Federal Depository Libraries (see <http://catalog.gpo.gov/fdlpdir/FDLPdir.jsp>). You will also be able to obtain this report also from the National Technical Information Service at <http://www.ntis.gov/products/publications.aspx> or at the address below in the near future.

U.S. Department of the Interior
Bureau of Ocean Energy Management
Environmental Studies Program
381 Elden Street
MS HE3115
Herndon, VA 20170-4817

U.S. Department of Commerce
National Technical Information Service
5285 Port Royal Road
Springfield, Virginia 22161
Phone: (703) 605-6040
Fax: (703) 605-6900
Email: bookstore@ntis.gov

CITATION

Curchitser, E.N., K. Hedstrom, S. Danielson, and T. Weingartner. 2013. Adaptation of an Arctic Circulation Model. U.S. Department of the Interior, Bureau of Ocean Energy Management, Environmental Studies Program, Headquarters, Herndon, VA. OCS Study BOEM 2013-202. 82 pp.

Abstract

This document is the final report for the U.S. Department of the Interior, Bureau of Ocean Energy Management (BOEM) Contract M10PC00116, Adaptation of an Arctic Circulation Model. The primary aim of the work done under this award was to use a state-of-the-art coupled circulation sea ice numerical ocean model to simulate several decades of the currents in the Chukchi and Beaufort Seas, which can be used as inputs to oil-spill models. This document reviews the basic oceanography of the region of interest, describes the relevant details of the models and their implementation for this particular problem, and describes the model-data comparisons that have been performed as part of this current award.

Contents

Acronyms and abbreviations	viii
1 Introduction	1
1.1 Background: The Chukchi and Beaufort Seas	1
2 Scientific and technical approaches	10
2.1 The coupled ocean-sea ice model	10
2.2 Arctic Implementation	12
2.2.1 Atmospheric forcing	12
2.2.2 Initial and boundary conditions	14
2.2.3 Albedo	15
2.2.4 Other model details	15
2.2.5 The model runs	15
3 Model-data comparisons	16
3.1 The data	16
3.2 Methodology	18
3.3 Model-data comparisons	18
3.3.1 Velocity	18
3.3.2 Temperature and Salinity	24
3.3.3 Sea Ice	34
4 Summary remarks	43
A Appendix: Monthly mean hindcast fields	46
A.1 Sea surface height	47
A.2 Velocities	49
A.3 Temperature at 5 m depth	53
A.4 Salinity at 5 m depth	55
A.5 Vertical cross-sections of velocity at 150°W	57
A.6 Vertical cross-sections of temperature at 150°W	59
A.7 Vertical cross-sections of salinity at 150°W	61
A.8 Vertical cross-sections of velocity at 71°N	63
A.9 Vertical cross-sections of temperature at 71°N	65
A.10 Vertical salinity cross-sections at 71°N	67

List of Figures

1	Idealized schematic of the circulation in the Chukchi and Beaufort seas. Maximum and minimum ice edges are approximations of the summer ice minimum over 1979-2002.	2
2	Chukchi sea schematic with labeled places and bathymetric features. Contours are plotted at 25 m, 50 m, 100 m 150 m, 200 m, 500 m, 1000 m, 2000 m and 3000 m depths.	3
3	Mean near-bottom currents measured by rotary current meters by year-long mooring deployments.	5
4	Observed monthly mean annual cycles in the western Arctic atmosphere-ocean system.	6
5	Modeled (blue) and observed (red) velocities at Chukchi Sea mooring C2.	7
6	Model domain showing bathymetry on top (meters) and telescoping resolution on bottom (kilometers).	13
7	Current meter and temperature/salinity time series mooring sites selected for comparisons.	17
8	Observed and modeled velocities at mooring MA3.	20
9	Modeled and observed velocities at Beaufort shelf mooring Dinkum.	22
10	Modeled and observed velocities at Chukchi shelf mooring MK1.	23
11	Chukchi and Beaufort flow field as represented by the moored observations and the model at the 19 comparison sites in Table 2.	25
12	Modeled (blue) and observed (red) water temperature (T) and salinity (S) at Bering Strait mooring MA3.	29
13	Modeled (blue) and observed (red) water temperature (T) and salinity (S) at Western Chukchi mooring MF2.	30
14	Modeled (blue) and observed (red) water temperature (T) and salinity (S) at Barrow Canyon mooring MK1.	31
15	Modeled (blue) and observed (red) water temperature (T) and salinity (S) at Beaufort shelf mooring Dinkum.	32
16	Predicted ice thickness and the difference between the predicted thickness and that observed by the IceSat satellite.	35
17	Monthly observed ice concentration and model-observed difference.	36
18	Mean observed ice concentration and model-observed RMSE.	37
19	Mean observed ice concentration and model-observed STD difference.	38
20	Mean observed ice concentration and model observed cross-correlation for the 1985–2005 Run05 hindcast.	39
21	Area weighted sea ice concentration time series.	41
22	Sea ice onset at 71°N for 166°W (top) and 168°W (bottom).	42
23	Transports averaged over the 1985–2005 Run05 hindcast for January and August.	44
24	Hindcast monthly mean sea surface height (SSH) maps for the Chukchi Sea.	47
25	Hindcast monthly mean vertically averaged velocity vectors from the Chukchi Sea.	49

26	Hindcast monthly mean vertically averaged velocity vectors from the North-east Chukchi Sea.	51
27	Hindcast monthly mean temperatures at 5 m depth in the Chukchi and Beaufort Seas.	53
28	Hindcast monthly mean salinity at 5 m depth in the Chukchi and Beaufort Seas.	55
29	Hindcast monthly mean horizontal velocity components at 150°W in the Beaufort Sea.	57
30	Hindcast monthly mean temperatures at 150°W in the Beaufort Sea.	59
31	Hindcast monthly mean salinity at 150°W in the Beaufort Sea.	61
32	Hindcast monthly mean horizontal velocity components at 71°N in the Chukchi Sea.	63
33	Hindcast monthly mean temperatures at 71°N in the Chukchi Sea.	65
34	Hindcast monthly mean salinity at 71°N in the Chukchi Sea.	67

List of Tables

1	Snow and ice albedo values.	15
2	Mooring sites selected for comparisons.	19
3	Statistics of the current meter moorings and model hindcasts at the mooring locations.	26
4	Statistics of the current meter moorings and model hindcasts for August and September.	27
5	Statistics of the current meter moorings and model hindcasts for February and March.	28
6	Statistics of winter and late summer temperature and salinity mooring data and model hindcasts.	33

Acronyms and abbreviations

ACC	Alaska Coastal Current
BOEM	Bureau of Ocean Energy Management
CORE	Coordinated Ocean-Ice Reference Experiment
EVP	Elastic Viscous Plastic [a rheology]
GLS	Generic Length Scale
KE	Kinetic Energy
MEKE	Mean Eddy Kinetic Energy
MKE	Mean Kinetic Energy
MKS	Meter, Kilogram, Second
MPI	Message Passing Interface
NEP	Northeast Pacific [a regional model hindcast]
NetCDF	Network Common Data Format
NSIDC	National Snow and Ice Data Center
PA	Principal Axis
RCM	Rotary Current Meter
RMSE	Root Mean Square Error
ROMS	Regional Ocean Modeling System
S	Salinity
SSH	Sea Surface Height
SODA	Simpl Ocean Data Assimilation
SSM/I	Special Sensor Microwave/Imager
STD	Standard Deviation
Sv	Sverdrup ($10^6 m^3/s$)
T	Temperature
UAF	University of Alaska Fairbanks
UW	University of Washington
U	Zonal velocity
V	Meridional velocity
θ	PA orientation

1 Introduction

1.1 Background: The Chukchi and Beaufort Seas

The Chukchi and Beaufort seas are the northernmost shelf seas bordering Alaska. Although properly a part of the western Arctic Ocean, both shelves are linked, atmospherically and oceanographically, to the Pacific Ocean. These connections profoundly influence the wind and wave regimes, the seasonal distribution of sea ice, the regional hydrologic cycle, and the water masses and circulation characteristics of the Chukchi shelf (Figure 1). The atmospheric connection is primarily via the Aleutian Low, whose time-varying position and strength and interactions with polar air masses affects regional meteorological conditions. The oceanographic link is via the mean northward flow through Bering Strait, which draws water from the Bering Sea shelf and basin, and is sustained by a large-scale pressure gradient between the Pacific and Atlantic oceans (*Coachman et al.* (1975); *Aagaard et al.* (2006)).

Chukchi Sea Oceanography

The northward flux of mass, heat, nutrients, carbon, and organisms through the strait bequeaths the Chukchi shelf with physical and ecological characteristics that are unique among arctic shelves. For example, the spring retreat (fall onset) of sea ice occurs earlier (later) in comparison to most other arctic shelves because of the northward heat flux through the strait. *Woodgate et al.* (2006) estimate that summer Pacific waters provide a heat source capable of melting nearly the entire (640,000 km²) 2-m thick ice cover of the Chukchi Sea and *Shimada et al.* (2006) contend that this flux may be an important source of interannual variability in the ice cover. Similarly, the enormous biological productivity of this shelf (*Walsh and Coauthors* (1989); *Grebmeier and McRoy* (1989); *Springer and McRoy* (1993)), including its ability to support large and diverse marine mammal populations, is due to the carbon and nutrient loads carried through Bering Strait.

The water properties of the strait throughflow reflect the time-varying output of physical processes occurring over the Bering shelf and northern North Pacific. These fluxes are a result of the net effects of upwelling from the deep Bering Sea basin and areally integrated heat and freshwater fluxes (*Aagaard et al.* (2006)), including the freezing and melting of sea ice (*Danielson et al.* (2006)), river runoff, atmospheric moisture and heat fluxes, and heat and freshwater contributions from the Gulf of Alaska (*Weingartner et al.* (2005b)), all of which ultimately affect the heat and salt budgets. Much of our understanding of the Chukchi shelf derives from the early syntheses of *Coachman et al.* (1975) and *Walsh and Coauthors* (1989) and from the observational studies of *Paquette and Bourke* (1974), *Mountain et al.* (1976), *Paquette and Bourke* (1981), *Ahlnäs and Garrison* (1984), *Aagaard et al.* (1985), *Aagaard* (1988), *Johnson* (1989), *Aagaard and Roach* (1990), *Hansell et al.* (1993), *Cooper et al.* (1997), *Münchow and Carmack* (1997), *Weingartner et al.* (1998), *Weingartner et al.* (1999), *Münchow et al.* (1999), *Münchow et al.* (2000), *Pickart* (2004), *Steele et al.* (2004), *Pickart et al.* (2005), *Weingartner et al.* (2005a), *Codispoti et al.* (2005), *Woodgate et al.* (2005), *Shimada et al.* (2006), *Nikolopoulos et al.* (2009), the modeling

1.1 Background: The Chukchi and Beaufort Seas

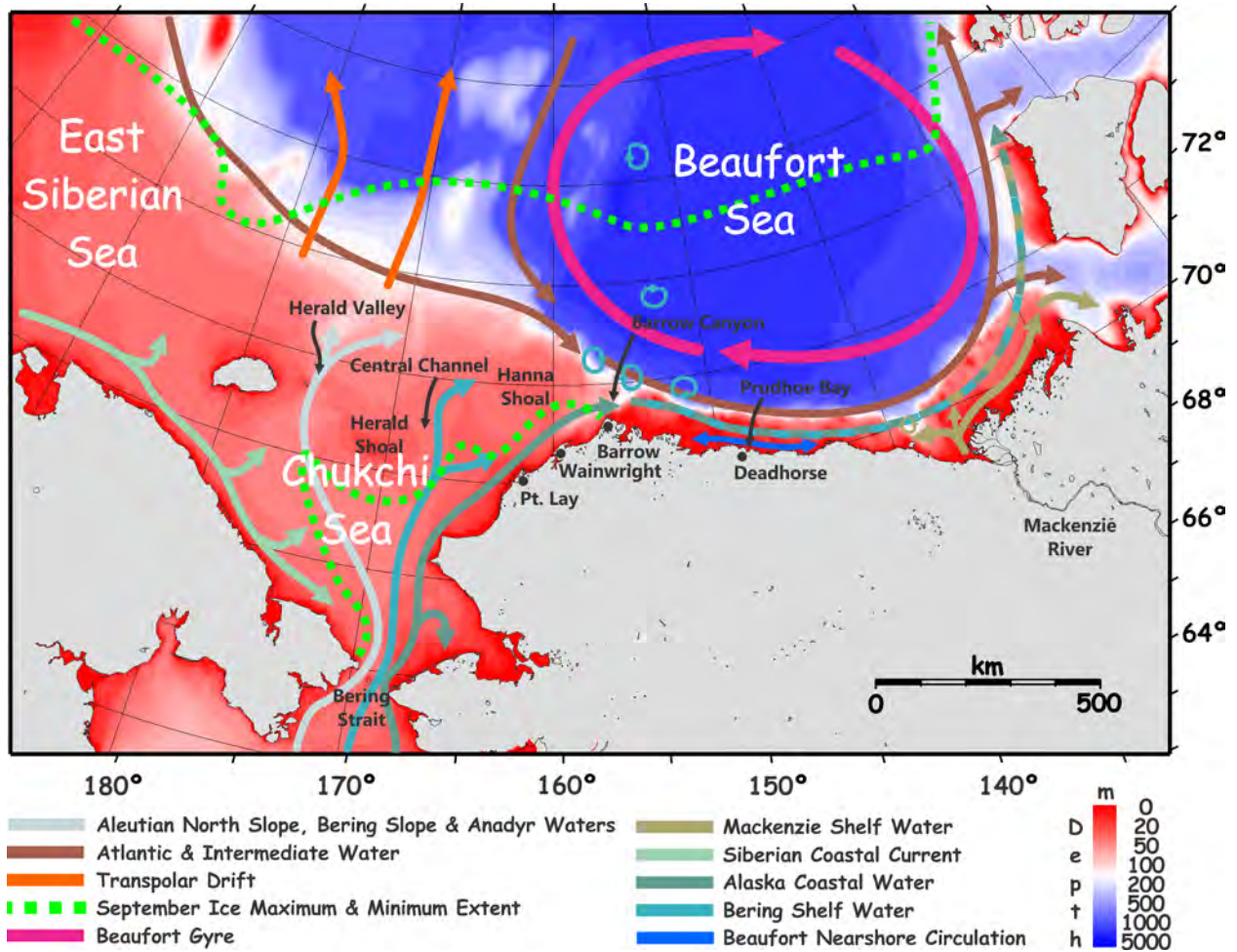


Figure 1: Idealized schematic of the circulation in the Chukchi and Beaufort seas. Maximum and minimum ice edges are approximations of the summer ice minimum over 1979-2002.

1.1 Background: The Chukchi and Beaufort Seas

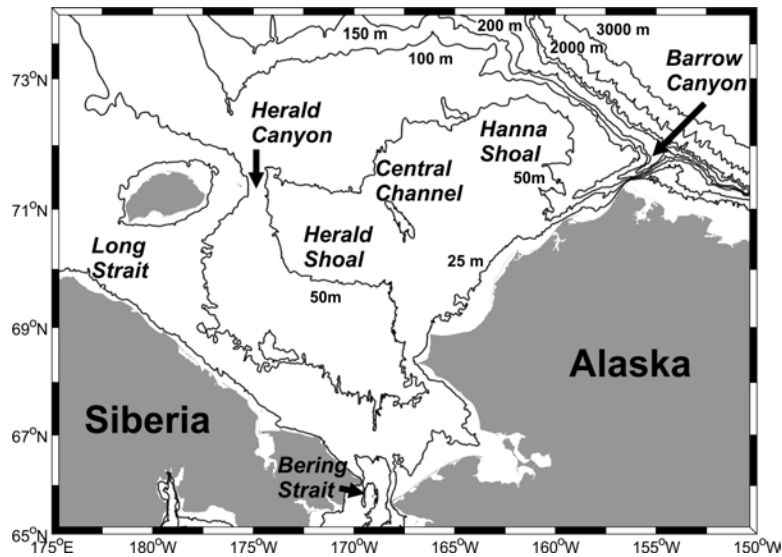


Figure 2: Chukchi sea schematic with labeled places and bathymetric features. Contours are plotted at 25 m, 50 m, 100 m, 150 m, 200 m, 500 m, 1000 m, 2000 m and 3000 m depths.

and theoretical work of *Gawarkiewicz and Chapman (1995)*, *Winsor and Chapman (2002)*, *Winsor and Chapman (2004)*, *Spall (2007)*, *Spall et al. (2008)*, and the sea-ice studies of *Muench et al. (1992)*, *Cavaliere and Martin (1994)*, *Liu et al. (1994)*, and *Martin and Drucker (1997)*. The following summary is drawn from these sources.

Mean Circulation

The shallow (about 50m) Chukchi Sea shelf extends approximately 800 km northward from Bering Strait to the shelfbreak at about the 200 m isobath. The mean flow over much of the shelf is northward due to the Pacific-Arctic pressure gradient and opposes the prevailing southwestward-blowing winds. This pressure gradient propels the Bering Strait throughflow along three principal pathways that are associated with distinct bathymetric features (Figure 2); Herald Canyon, the Central Channel, and Barrow Canyon. Herald Shoal separates Herald Canyon from the Central Channel, and Hanna Shoal is between Barrow Canyon and the Central channel. The recent BOEM Chukchi Sea lease sales lie on the northeast shelf between the Central Channel and Barrow Canyon and south of Hanna Shoal (Figure 2).

As sketched in Figure 1, a western branch of waters originating south of Bering Strait flows northwestward from the strait and exits the shelf through Herald Canyon. While most of this outflow probably descends through Herald Canyon, some of it spreads eastward across the central shelf. A second branch flows northward through the Central Channel and then probably splits; with some water continuing eastward toward the Alaskan coast along the south flank of Hanna Shoal while the remainder flows northeastward toward the continental slope. The third branch flows northeastward along the Alaskan coast towards Barrow Canyon at the junction of the Chukchi and Beaufort shelves. In summer this flow includes the

1.1 Background: The Chukchi and Beaufort Seas

northward extension of the Alaskan Coastal Current (ACC) that originates south of Bering Strait. At the head of Barrow Canyon the ACC is joined by waters flowing eastward from the central shelf, with the merged flow then continuing downcanyon as a narrow, but strong, coastal jet.

Mean current speeds within the Herald and Barrow canyons are swift (about 25 cm/s), more moderate in the Central Channel (about 10 cm/s), and generally less than 5 cm/s elsewhere (Figure 3). Long-term transport estimates for these three pathways are very approximate at best and suggest that the flow through the Central Channel is about 200,000 m³/s, while the branches in both Herald Canyon and Barrow Canyon carry about 300,000 m³/s. Estimates of transit time from Bering Strait to Barrow Canyon are from 3–4 months in summer and longer in winter. The vectors in Figure 3 suggest that some of the Barrow Canyon outflow proceeds eastward along the Beaufort continental slope. Water mass analyses and current meter measurements clearly show that this is indeed the case, but apparently not all of the mass transported down the canyon is captured by the slope flow. Instead some of the outflow is entrained into shelfbreak eddies that drift into the deep basin, some appears to spill over onto the inner Beaufort shelf when opposing winds are sufficiently weak [Okkonen, pers. comm.], and some appears to drift northwestward from the Barrow canyon mouth and into the Arctic basin. The influence of the three flow pathways northwards from Bering Strait is evident, in summer and fall, by the formation of perennial “melt-back embayments” that indent the ice edge. The embayments reflect accelerated melting by the warm Bering Sea summer waters that are channeled northward along these pathways (Figure 1).

The routes and transit times by which Bering water ultimately enters the Arctic Ocean affects the distribution of hydrographic properties across the Chukchi Sea shelf (Figure 1) and gives rise to complex shelf hydrographic structures. For example, Figure 4 indicates that relatively warm (temperature greater than 2°C) and salty (salinity greater than 32.4) “summer” water from Bering Strait is found in Herald Canyon and the Central Channel. Warm, but fresher (salinity less than 32.2), Alaskan Coastal Water, also of Bering Sea origin, occupies the head of Barrow Canyon. Cold, dilute waters, derived from ice melt, lie along the western side of Herald Canyon, within the upper 20 meters atop Herald Shoal, and between the Central Channel and Barrow Canyon. Of particular importance is the strongly stratified, 2-layer structure of the water column between the Central Channel and Barrow Canyon (e.g., within the area occupied by recently leased tracts). The stratification increases from spring through summer and then erodes in fall as strong winds, cooling and freezing mix the water column. Seasonal changes in stratification may possibly lead to different surface velocity responses to winds. In addition to its spatial complexity, the hydrographic structure can vary considerably on seasonal and storm time scales as well as from year-to-year.

The observed mean flow (Figure 3) is similar to that depicted in previous numerical circulation models of the Chukchi shelf (*Proshutinsky* (1986); *Winsor and Chapman* (2004); *Spall* (2007)). These (and other) model results are consistent with the observed mean currents in showing that the mean, vertically integrated flow, which parallels the streamlines, crosses the Chukchi shelf and is swiftest where the streamlines converge (e.g., channels and canyons). The weakest flow occurs over the two shoals and relatively weak flow occurs where

1.1 Background: The Chukchi and Beaufort Seas

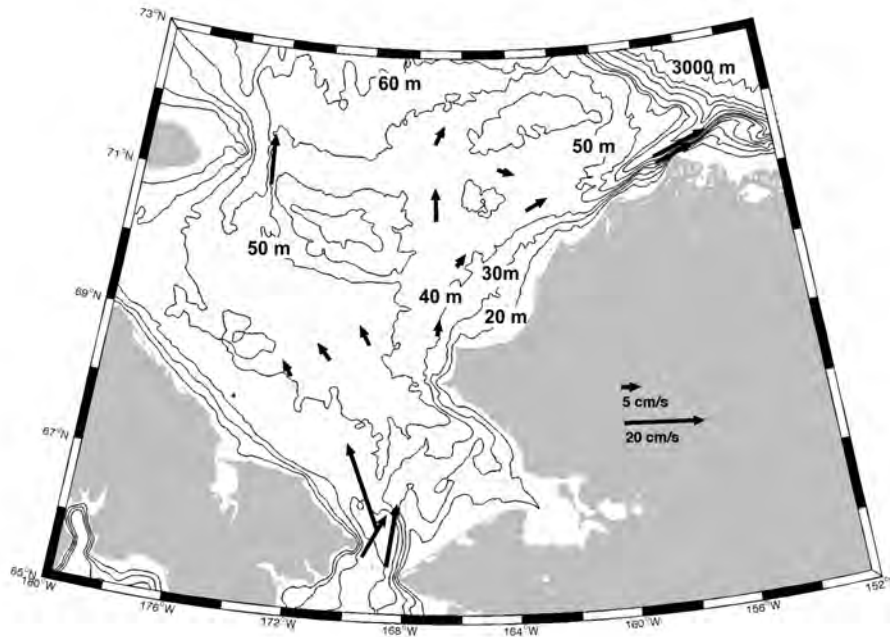


Figure 3: Mean near-bottom currents measured by rotary current meters by year-long mooring deployments. Bathymetric contours are plotted at depths of 20, 30, 40, 50, 60, 80, 100, 150, 250, 500, 1000, 2000 and 3000 m.

there is little bottom relief. An implication from the models is that materials discharged southwest of Hanna Shoal may be advected around the northern and eastern sides of the shoal and then swept down Barrow Canyon.

The mean circulation is due to the large scale pressure field between the Pacific and Arctic oceans and opposes the mean winds, which are from the northeast at about 4 m/s on average. The winds are, however, the principal cause of flow variations, which can be substantial. Wind forcing varies seasonally with the largest values being in fall and early winter and the smallest being in summer (Figure 4). The current time series in Figure 5 and statistical analyses (*Weingartner et al. (2005a)*) indicate that current fluctuations are coherent with wind velocity variations over the northeast shelf over spatial scales of at least 300 km and have decorrelation time scales of three to five days. These adjustments reflect wind-induced modifications to the shelf pressure field. Although the adjustment envelopes a broad area, the magnitude of the current response varies over the shelf. In particular both the wind-forced (and mean) currents are more vigorous in regions of strong topographic gradients (Central Channel and Barrow Canyon) than in areas of gentler bottom relief. On occasion, and most frequently in fall and winter, strong southwestward-blowing winds can reverse the shelf flow field or even re-distribute the flow from one of the main flow pathways to another.

The current measurements described above were obtained from current meters installed

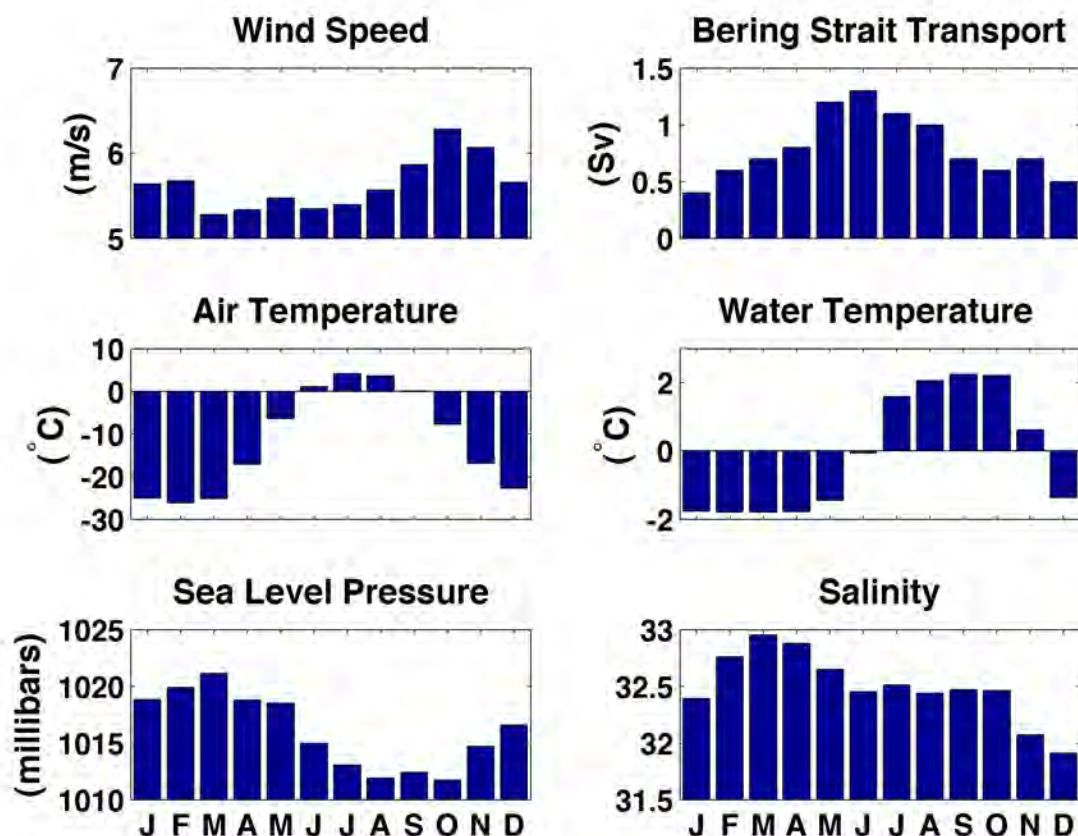


Figure 4: Observed monthly mean annual cycles in the western Arctic atmosphere-ocean system. Meteorological parameters are from the National Weather Service station located in Barrow, AK and the transport, water temperature, and salinity monthly means are from observations in Bering Strait (*Woodgate et al. (2005)*).

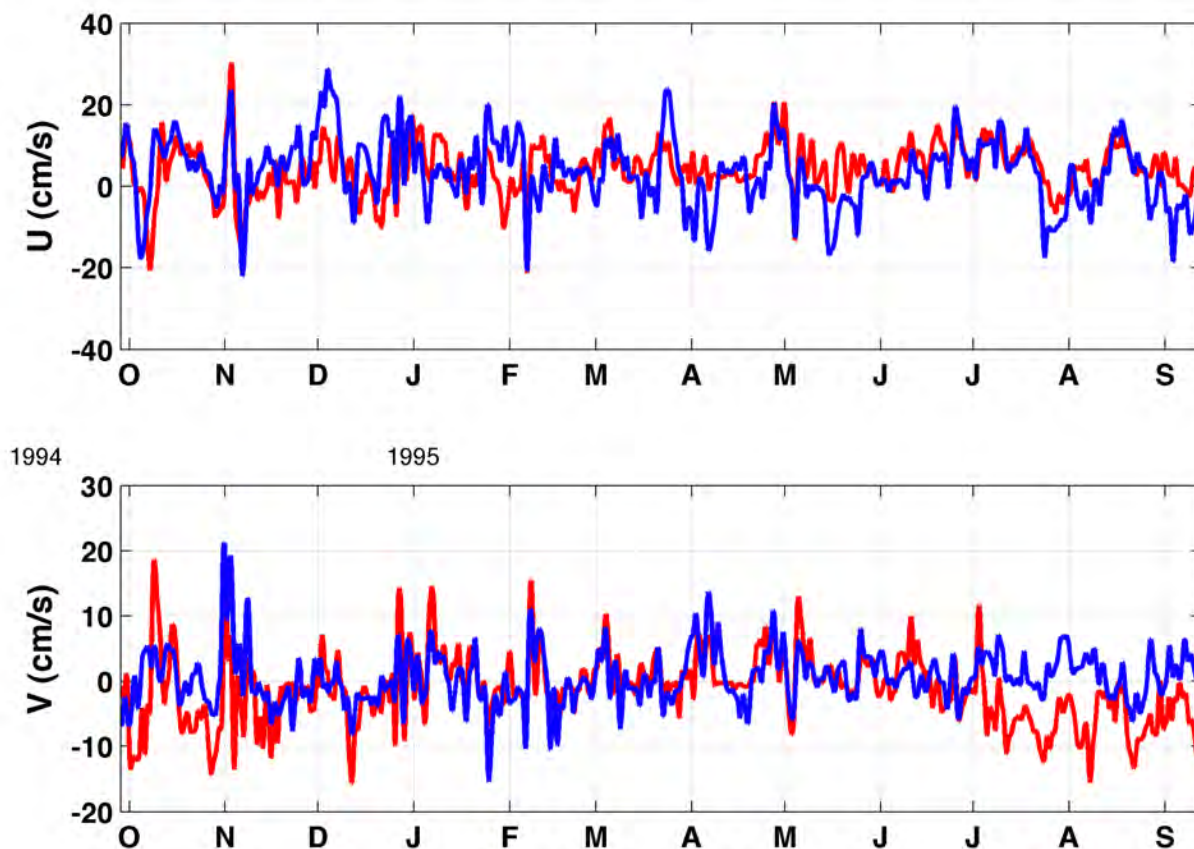


Figure 5: Modeled (blue) and observed (red) east-west (U) and north-south (V) velocities at Chukchi shelf mooring C2. See Figure 7 and Table 2 for location and duration of the observation. Observed and modeled velocities in this figure have been smoothed with a 5-day lowpass filter.

about 10 m above the seabed in depths greater than 40 m. However, these measurements may not reflect the surface currents. Although there are few direct measurements of surface currents on the Chukchi Sea, ice drift measurements suggest that ice drifts westward (and downwind) over the outer Chukchi shelf. In addition, several passive acoustic recorders prematurely released in summer 2008 drifted westward out of the lease sale area (Rea, pers. comm., 2009). These few observations suggest that the flow in a “thin” surface layer, which absorbs the bulk of the momentum imparted by the wind to the water column, may differ from the deeper flow measured by current meters. The model runs do suggest the existence of a thin sheared layer at the surface (see the velocity climatology plots for the 71°N cross-sections in appendix A.8). Satellite-tracked drifters have been deployed in the Chukchi Sea during the 2011 and 2012 summer months as part of a BOEM-sponsored program. The preliminary results of this field program and other water column measures of currents will provide an opportunity for future analyses to quantitatively assess the vertical shears and compare the observed fields to those predicted by the numerical model. The thickness of this wind-shear layer will likely vary due to wind velocity, ice, topography, and stratification.

Other current variations are induced by mesoscale (10–50 km) motions resulting from instabilities generated by cross-frontal ocean density gradients. Mesoscale flows (eddies and frontal meanders) can be vigorous (greater than 20 cm/s) and uncorrelated with winds. Eddies and meanders are often prominent features of ice-edge fronts, and they may occur in winter due to ocean frontal instabilities at the edge of polynyas where large density differences form between cold, dense polynya waters and less dense waters seaward of the polynya. These instabilities are believed to generate vigorous cross-isobath eddy fluxes of dense coastal water from within the polynyas that may be carried far from the coast and across the shelf. Extensive polynyas develop in most winters along the northwest Alaska coast between Barrow and the Lisburne peninsula.

Beaufort Sea Oceanography

The Alaskan Beaufort Sea shelf (Figure 1) extends approximately 500 km eastward from Point Barrow to the Mackenzie portion of the Beaufort Sea shelf in Canadian waters. The shelf width is approximately 80 km as measured from the coast to the 200 m isobath. Shelf depths grade smoothly offshore with bottom slopes typically being about 10^{-3} inshore of the 100 m isobath. Sea ice can cover the shelf year-round, although more typically the inner shelf (and in recent years the entire shelf) is ice-free during the summer months. Landfast ice begins to form in October and extends 20–40 km offshore through mid-June so that it covers nearly 25% of the shelf area (*Barnes et al. (1984)*) through most of the year. *Weingartner et al. (2009)* shows that currents under the landfast ice are small and uncorrelated with the local winds whereas currents in the presence of freely drifting ice and open water (summer months) are highly coherent with the winds. The landfast ice is relatively smooth adjacent to the coast, but is increasingly deformed offshore.

The Beaufort’s oceanic circulation and ice deformation are related to the seasonally varying winds. These we summarized in the form of monthly statistics using the archived National Weather Service wind record in Barrow from 1949–2005. The alongshore component of the

winds accounts for most of the variance in the winds and are primarily responsible for forcing shelf circulations. In general, winds blowing from the northeast prevail throughout the year. On a monthly basis the majority of the alongshore winds are westward (upwelling favorable) and westward winds are, on average, stronger than eastward (downwelling-favorable) winds. There are however, substantial seasonal differences. Westward winds are strongest in late fall and early winter and occur most frequently in October, November, and March. Westward winds are only slightly more frequent than eastward winds in July and August, although westward winds are stronger in these months. Thus, on average, upwelling favorable conditions prevail throughout the year. Although the alongshelf wind stress component is important in the ocean circulation, the north-south component plays an important role in ice dynamics. In particular, winter winds are primarily onshore (southward) and thus force pack ice onshore and deform the landfast ice edge. Less frequent offshore winds can result in detachment of the landfast ice (breakouts). These seasonal variations are primarily related to the deep high pressure cell centered over the Arctic Ocean in winter. However, the high pressure system weakens in summer and fall, when low-pressure systems invade the Beaufort Sea from the North Pacific (*Maslanik et al. (1999)*).

Seasonally varying mesoscale winds may substantially alter the synoptic wind field in the nearshore zone. For example, a persistent summer sea breeze results in mean westward winds within 25 km of the coast (*Kozo (1982a)*, *Kozo (1982b)*). *Brower et al. (1988)* indicate that mean summer winds are westward, which suggests there is a reversal in wind direction on crossing the shelf. From October through April mountain barrier baroclinicity (*Kozo (1980)*; *Kozo (1984)*) can produce along-shore divergence in the wind field. This effect occurs when the southward flow of low-level cold air from the Arctic Ocean is blocked along the northern flank of the Brooks Range. The resulting isopycnal slopes induce eastward surface winds of about 15 m/s over a horizontal width scale of 200–300 km. The western Beaufort coast is rarely influenced by the mountain barrier effect because it lies more than 300 km north of the Brooks Range, but the eastern Beaufort coast lies within 60 km of the mountains. Consequently, winds can be westward over the western Beaufort coast but eastward along the eastern coast. *Kozo (1984)* estimated that the mountain barrier baroclinicity effect occurs approximately 20% of the time during winter.

Three distinct oceanic regimes bound the Alaskan Beaufort Sea. To the west, variability in Barrow Canyon outflow is large, especially in fall and winter, and mainly due to fluctuations in the regional winds (*Weingartner et al. (1998)*; *Weingartner et al. (2005a)*; *Woodgate et al. (2005)*). Some of the Barrow Canyon outflow continues eastward as a subsurface current (or slope undercurrent) along the Beaufort shelfbreak and slope where it forms the upper halocline waters of the Canada Basin (*Mountain et al. (1976)*; *Aagaard (1984)*; *Pickart (2004)*; *Pickart et al. (2005)*; *Nikolopoulos et al. (2009)*). Under weak westward winds or eastward winds some of the water exiting Barrow Canyon rounds Pt. Barrow and continues onto the inner portion of the western Beaufort shelf (*Okkonen, pers. comm.*).

The outer shelf and continental slope provide the offshore boundary for the Alaskan Beaufort Sea. In the upper 50 m or so the flow is westward and part of the southern limb of the wind-driven Beaufort Gyre. This flow can occasionally be reversed by strong eastward

winds and/or by occasional shelfbreak upwelling that advects eastward momentum from the slope undercurrent onto the shelf at least as far inshore as the 50 m isobath (*Aagaard (1984); Pickart (2004); Nikolopoulos et al. (2009)*).

The Mackenzie shelf joins the Alaskan Beaufort shelf to the east and likely the year-round discharge from the Mackenzie River influences the eastern Beaufort shelf (*Carmack et al. (1989); Macdonald et al. (1989); Macdonald and Carmack (1991)*). Mackenzie shelf water has been detected throughout much of the Canada basin, including the continental slope of the Chukchi and western Beaufort Sea as far as 160W longitude (*Guay and Falkner (1998); Macdonald et al. (1999)*). Conceivably wind-driven currents transport Mackenzie shelf waters onto the Alaskan Beaufort shelf as well; observations of satellite imagery suggest that the summer melt in the Alaskan Beaufort is strongly dependent upon the Mackenzie River plume (*Weingartner et al. (2009)*). In addition to the Mackenzie River, a large number of smaller rivers discharge into the Alaskan Beaufort Sea. These are asymmetrically distributed with most of them discharging into the central and eastern portions of the shelf.

2 Scientific and technical approaches

In this section, we describe the modeling framework, its components, and the details of the model implementation, forcing, boundary conditions, and the various model integrations performed.

2.1 The coupled ocean-sea ice model

The main research tool used for this work is a state-of-the-art coupled ocean/sea ice model based on the Regional Ocean Modeling System (ROMS) (*Shchepetkin and McWilliams (2005)*). ROMS is a free-surface, hydrostatic primitive equation ocean circulation model whose core was developed at Rutgers University and University of California, Los Angeles with significant contributions from a large community of users. ROMS is a terrain-following, finite volume (Arakawa C-grid) model with the following advanced features: extensive restructuring for sustained performance on multi-processor computing platforms (using MPI); high-order, weakly dissipative algorithms for tracer advection; a unified treatment of surface and bottom boundary layers (e.g., K-Profile Parameterization; *Large et al. (1994)*), atmosphere-ocean flux computations based on the ocean model prognostic variables using bulk-formulae (*Fairall et al. (1996)*) and an integrated set of procedures for data assimilation (e.g., optimal interpolation and adjoint-based methods; *Moore et al. (2004)*). ROMS also has an integrated float tracking capability. The vertical discretization is based on a terrain-following coordinate system with the ability to increase the resolution near the surface and bottom boundary layers.

ROMS has been coupled to a sea-ice model (*Budgell (2005)*) consisting of the elastic-

2.1 *The coupled ocean-sea ice model*

viscous-plastic (EVP) rheology (*Hunke and Dukowicz (1997), Hunke (2001)*) and the *Mellor and Kantha (1989)* thermodynamics. It is fully explicit and implemented on the ROMS Arakawa C-grid and is therefore fully parallel using MPI, just as ROMS is. The model also includes frazil ice growth in the ocean being passed to the ice (*Steele et al. (1989)*). It currently follows a single ice category, which exhibits accurate results in a marginal ice zone such as the Bering Sea.

The principal attributes of the model are:

1. General

- (a) Primitive equations with potential temperature, salinity, and an equation of state.
- (b) Hydrostatic and Boussinesq approximations.
- (c) Optional third-order upwind advection scheme.
- (d) Optional Smolarkiewicz advection scheme for tracers (potential temperature, salinity, etc.).
- (e) Optional Lagrangian floats.
- (f) Option for point sources and sinks.

2. Horizontal

- (a) Orthogonal-curvilinear coordinates.
- (b) Arakawa C grid.
- (c) Choice of closed, periodic, prescribed, radiation, and gradient open boundary conditions.
- (d) Masking of land areas.

3. Vertical

- (a) sigma (terrain-following) coordinate.
- (b) Free surface.
- (c) Tridiagonal solver with implicit treatment of vertical viscosity and diffusivity.

4. Ice

- (a) Hunke and Dukowicz elastic-viscous-plastic dynamics.
- (b) Mellor-Kantha thermodynamics.
- (c) Orthogonal-curvilinear coordinates.
- (d) Arakawa C grid.
- (e) Smolarkiewicz advection of tracers.

5. Mixing options

2.2 Arctic Implementation

- (a) Horizontal Laplacian and biharmonic diffusion along constant s, z or density surfaces.
- (b) Horizontal Laplacian and biharmonic viscosity along constant s or z surfaces.
- (c) Optional Smagorinsky horizontal viscosity and diffusion (but not recommended for diffusion).
- (d) Horizontal free-slip or no-slip boundaries.
- (e) Vertical harmonic viscosity and diffusion with a spatially variable coefficient, with options to compute the coefficients with *Large et al.* (1994), Mellor-Yamada, or generic length scale (GLS) mixing schemes.

6. Implementation

- (a) Dimensional in meter, kilogram, second (MKS) units.
- (b) Fortran 90.
- (c) Runs under UNIX, requires the C preprocessor, gnu make, and Perl.
- (d) All input and output is done in NetCDF (Network Common Data Format), requires the NetCDF library.
- (e) Options include serial, parallel with MPI, and parallel with OpenMP.

Exhaustive details of the model are provided in the accompanying manual which is part of the deliverables for this contract (Hedstrom, 2013, MMS 2013-???)

2.2 Arctic Implementation

We developed an arctic domain (Figure 6) that focuses the resolution down to 4–5 km over the Chukchi and Beaufort seas and coarsens away from the region of interest. The overall model extent was determined after extensive testing of the coupled ocean-sea ice model. Though we have extensive experience with open boundary conditions for multi-decadal integrations of regional ocean models, the open sea ice boundaries proved to be challenging. The final configuration was chosen so as to minimize errors in both the circulation and the sea ice distributions in the region of interest, while allowing us to maintain high resolution there.

Tidal forcing is implemented through the boundaries using the eight dominant diurnal and semi-diurnal components derived from the Oregon State TOPEX/Poseidon Global Inverse Solution (TPXO) (*Egbert and Erofeeva* (2002)) (<http://www.coas.oregonstate.edu/research/po/research/tide/global.html>).

2.2.1 Atmospheric forcing

We are using the CORE2 forcing files (*Large and Yeager* (2008)) and computing the momentum, heat and salt fluxes from the atmospheric conditions and the model's surface tem-

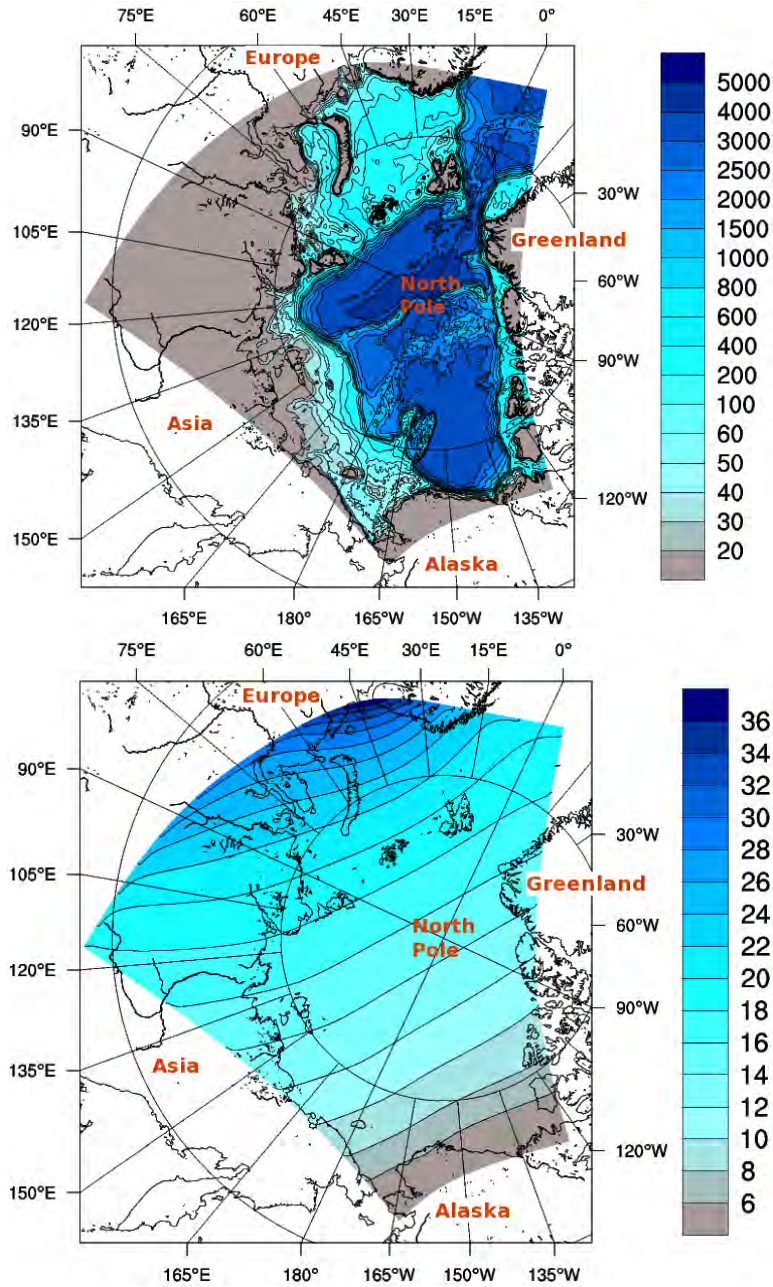


Figure 6: Model domain showing bathymetry on top (meters) and telescoping resolution on bottom (kilometers).

perature. There are two options for this bulk flux computation in ROMS—we are using that described in *Large and Yeager* (2008). CORE2 provides six-hourly winds, air temperature, air pressure and humidity plus daily radiation fields. With minimal tweaking of the time variables, the CORE2 files can be used as is, on their native grid, then interpolated by ROMS internally to the domain at run time.

2.2.2 Initial and boundary conditions

The best ocean fields we knew of at the start of the project are known as Simple Ocean Data Assimilation (SODA), a reanalysis from 1958 through 2005 by *Carton et al.* (2005). There are Python scripts to create initial and boundary conditions from the SODA files (one every five days). Snow (monthly) and ice (daily) initial and boundary conditions are obtained from model results generously provided by Jinlun Zhang. Three boundary files (ocean, snow, ice) are used so that each field can have its own unlimited time dimension.

The side known as “South” is along Northern Alaska and Western Canada and is set to closed. The side known as “West” is only open at Bering Strait, where the inflow is imposed using a “rivers” file, but letting temperature and salinity come in from SODA boundary conditions. The last two boundaries on the Atlantic side use a combination of radiation and nudging as suggested by *Marchesiello et al.* (2001). The nudging timescales are 3 days on inflow, 360 days on outflow, values we have found to be well-behaved in prior simulations. The idea is that on outflow, the boundary conditions should be dominated by a radiation condition, allowing signals to exit the domain. On inflow, the boundary conditions should be more strongly influenced by conditions from the global model. Previous studies (*Coachman and Aagaard* (1981); *Woodgate et al.* (2005)) have shown that the local wind is significantly correlated with the Bering Strait transport variability, with the best correlations accounting for up to 50% of the observed variance. Following this approach, we regress hindcast winds from the North American Regional Reanalysis (*Mesinger and Coauthors* (2006)) against the observed Bering Strait velocity record (*Woodgate et al.* (2005)) to form the best least-squares fit of the wind field to the velocity field and thus achieve an estimate of the inflow for the entire integration time period.

Other forcings include a 360-day nudging to sea surface salinity climatology, runoff from *Dai et al.* (2009), which is prescribed as a virtual precipitation source along the coastlines using their monthly varying global gridded discharge estimates and a fastice climatology from Andy Mahoney (http://mms.gina.alaska.edu/private/landfast_summary.html). This latter is used to set the ice velocity to zero when the climatology indicates the presence of landfast ice.

Table 1: Snow and ice albedo values.

Wet ice	0.60	Snow is absent, temperature is at 0.0 C
Dry ice	0.65	Snow is absent, temperature is below -1.0 C
Wet snow	0.72	Snow is present, temperature is at 0.0 C
Dry snow	0.85	Snow is present, temperature is below -1.0 C

2.2.3 Albedo

The default ice albedo is chosen based on the presence or absence of snow and on the surface temperature. Temperatures below -1° C are assumed to be dry while temperatures between -1° C and 0° C are a linear combination of the wet and dry albedoes shown in Table 1. The ocean albedo is assumed to depend on latitude θ as:

$$1.0 - [0.069 - 0.11 \cos(2\theta)] \quad (1)$$

This albedo function is meant to provide the influence of low marine clouds not well captured by the CORE2 atmospheric model.

2.2.4 Other model details

Some choices are made via C preprocessor flags when compiling ROMS. These choices include masking, salinity, sea ice and the non-linear equation of state. We also use Laplacian viscosity on σ -surfaces, diffusion along constant z-surfaces and the full non-linear, curvilinear momentum equations. We are applying the tides, including the forcing provided by the tidal potential. The linear bottom drag coefficient varies spatially and is prescribed as a function of the water depth. The model was unstable with the k-profile parameterization vertical mixing (*Large et al. (1994)*) so we instead used the $k - \omega$ parameters in the GLS vertical mixing scheme (*Umlauf and Burchard (2003)* and *Warner et al. (2005)*) which proved to be more well-behaved.

2.2.5 The model runs

The Arctic models runs of note are known privately as RUN05, RUN07, and RUN10. The characteristics by which they differ significantly are:

- **RUN05:** the run delivered to BOEM.
 - Six-hourly CORE2 atmospheric fields, daily radiation forcing.
 - Bering Strait inflow imposed based on correlation between winds and observed currents.

- “Classic” albedo formulation for ice, our best latitudinal dependence of albedo for the ocean.
- Years simulated: 1985–2005.
- **RUN07**: a run with worse ice characteristics.
 - Three-hourly Modern-Era Retrospective Analysis for Research and Applications (MERRA) atmospheric fields and radiation forcing.
 - Bering Strait boundary conditions coming from a run of the Northeast Pacific domain.
 - Albedo imposed from MERRA for both ice and ocean.
 - Years simulated: 1987–2006.
- **RUN10**: A short test, too recent for the needs of this project.
 - Three-hourly MERRA atmospheric fields and radiation forcing.
 - Bering Strait boundary conditions coming from a run of the Northeast Pacific domain.
 - Ice albedo from *Ebert and Curry* (1993).
 - Years simulated: 1987–1995.

The only ice albedo in our code to account for melt ponds is that of *Ebert and Curry* (1993). It has been implemented for some time, but proved to be unstable until a bug was found and fixed. We hope to use it in future runs.

3 Model-data comparisons

3.1 The data

An integral part of this project is model skill assessment. We rely on publicly available in situ and remotely sensed datasets for model evaluation and validation. The moored records come from University of Alaska Fairbanks (UAF) and University of Washington (UW) field campaigns during 1990–1996 in the Chukchi Sea and 1999–2006 in the Beaufort Sea (Figure 7). Remotely sensed ice concentration data comes from the National Snow and Ice Data Center (NSIDC) archives of the passive microwave SSM/I satellite measurements and is available on a daily or bi-daily basis for the entire model integration period. Midwinter ice thickness data are taken from the IceSat composites (*Kwok et al.* (2009)) and are only available during two years of the model integration time period.

We located and assembled nearly seventy moored current meter and temperature/salinity time series from the Chukchi and Beaufort Sea shelves with records that overlapped in time

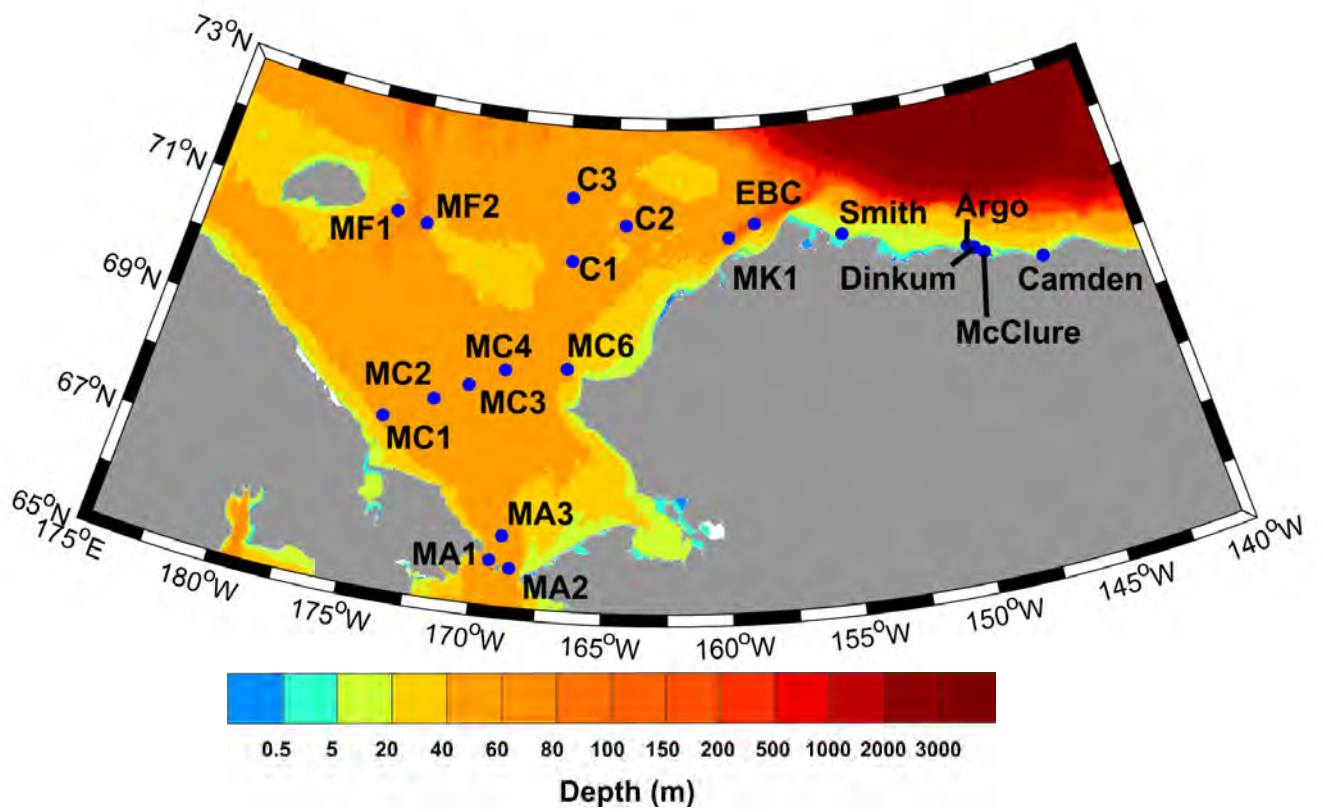


Figure 7: Current meter and temperature/salinity time series mooring sites selected for comparisons.

with the model integration period. All of these records were visually inspected for erroneous data and the data were retained in entirety, truncated to the intervals deemed reliable, or discarded. Examples of problems found included stuck rotors on the Aanderaa rotary current meter (RCM) instruments (possibly due to frazil ice in the water column or biofouling), drift in the conductivity/salinity records, and conductivity/salinity step changes inconsistent with our notions of the seasonal melt/freezing cycle. From the good records, we selected 38 records (19 each of the velocity and temperature/salinity) based on data record length and location so that we achieve a representative and spatially distributed set of mooring locations at which to make comparisons (Figure 7 and Table 2).

3.2 Methodology

We make comparisons between the water column point measurement current meter velocities and the vertically averaged velocity at the model grid point closest to the mooring deployment location (U = east-west velocity and V = north-south velocity). In general, the mismatch between the vertically averaged model currents and the observations do not pose problem for the comparisons because most of the vertical shear is limited to a fairly narrow layer at the surface of the water column. This simplification is justified by the analysis of mean current components, which for nearly all comparisons shows no significant difference (at the 95% confidence level) between the mean observed and modeled velocities. Temperature and salinity comparisons are made between the observed T/S (usually located within 10 m of the seafloor) and near-bottom depths from the model, so as to avoid the surface mixed layer and associated stratification. We note that the comparisons are biased to on-shelf locations and that a subjective examination of the shelf-slope Beaufort Gyre exhibits a very energetic (perhaps too strong) modeled gyre circulation.

To examine the model's ability to represent the seasonality in the moored records, we compute statistics based on late summer (August-September) and mid-winter (February-March) time intervals. These two periods are selected based on the need to evaluate model performance at opposite ends of the annual cycles in the heat content, ice cover, and fresh water content (Figure 4). The late summer interval represents a period of time with increasing winds as the fall storm season approaches, ice-free waters or low ice concentrations, warm temperatures and decreasing salinities. Mid winter is characterized by near-freezing temperatures, high salinities and near complete ice cover.

3.3 Model-data comparisons

3.3.1 Velocity

Figure 5 and Figures 8–10 show examples of the moored velocity records plotted along the model hindcasts at one coastal Beaufort Sea site (Dinkum), one northeast Chukchi Sea site

3.3 Model-data comparisons

Table 2: Mooring sites selected for comparisons. Columns show the mooring name, deployment site latitude and longitude, start and end dates of the good observations and the number of hourly observations.

Station	MA1	MA2	MA3	MC1	MC2	MC3	MC4	MC6	MF1	MF2
Latitude	65.9	65.8	66.3	67.9	68.3	68.6	68.9	69.0	71.1	71.0
Longitude	-169.4	-168.6	-169.0	-174.5	-172.5	-171.1	-169.6	-166.9	-175.7	-174.2
Start Date	25-Sep-90	5-Sep-90	5-Sep-90	23-Sep-90	23-Sep-90	23-Sep-90	22-Sep-90	10-Sep-90	22-Sep-90	22-Sep-90
End Date	28-Apr-91	27-Mar-91	5-Sep-91	4-Oct-91	19-Sep-91	16-Aug-91	4-Sep-91	22-Sep-91	14-Jan-91	30-Sep-91
N	5161	4873	8761	9025	8665	7849	8329	9049	2737	8953
Station	MK1	C1	C2	C3	EBC	Argo	Camden	Dinkum	McClure	Smith
Latitude	71.1	70.7	71.3	71.7	71.3	70.5	70.0	70.4	70.3	71.0
Longitude	-159.5	-167.0	-164.5	-167.2	-158.2	-148.2	-144.9	-147.9	-147.5	-154.0
Start Date	14-Sep-90	28-Sep-94	29-Sep-94	29-Sep-94	26-Sep-94	15-Aug-99	27-Aug-04	15-Aug-99	15-Aug-99	30-Aug-04
End Date	22-Sep-91	13-Sep-95	13-Sep-95	13-Sep-95	11-Sep-95	19-Aug-02	25-Jul-05	19-Aug-02	31-Aug-01	23-Jul-05
N	8953	8401	8377	8377	8401	17641	7981	26401	17929	7849

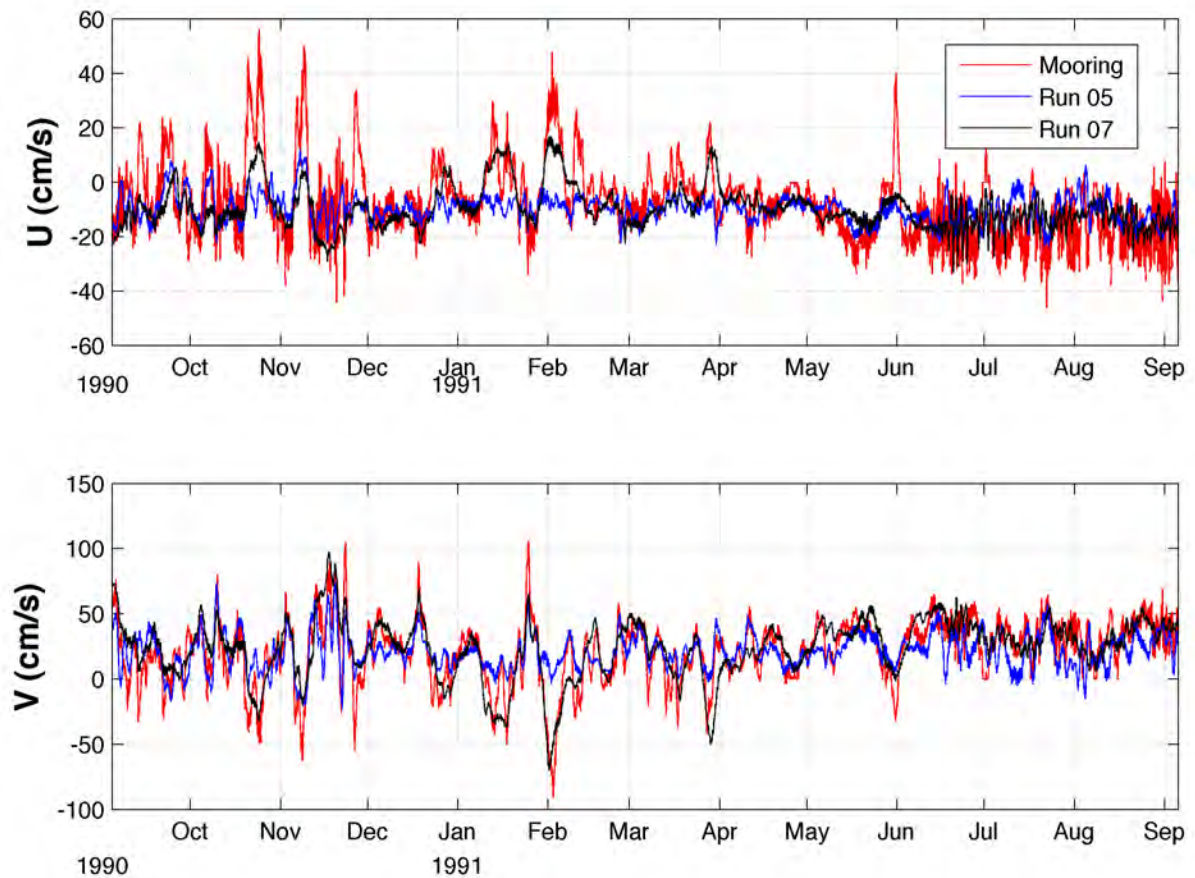


Figure 8: Observed (red) and modeled for RUN05 (blue) and RUN07 (black) east-west (U) and north-south (V) velocities at mooring MA3 during the fall 1990 to fall 1991 deployment.

near Barrow Canyon (MK1), one offshore Chukchi site within Central Channel (C2), and one southern Chukchi Sea site in Bering Strait (MA3).

In Bering Strait (mooring MA3, Figure 8), the flow is strongly influenced by the southern boundary conditions. We find that the boundary conditions of RUN05, which is based on a regression to the local winds, reproduces much of the observed variability but misses many large excursions. RUN07 boundary conditions, based on computations made by the Northeast Pacific (NEP) regional model hindcast, performs better but still underestimates or misses entirely some of the largest excursions observed by the mooring. Recent tests (not shown here) suggest that these missed excursions may be related to propagating continental shelf waves generated by wind stress that is not well reproduced in the large-scale atmospheric forcing fields employed by the reanalysis products. Missing these excursions will limit the model's ability to reproduce observed variability far away from the model boundary because these barotropic waves can propagate great distances, moving rapidly at the shallow water wave speed. Results described in this document refer to the RUN05 integration because the RUN07 run exhibited unacceptable ice thicknesses and concentrations.

The effects of the imposed landfast ice in the Beaufort Sea are obvious in the Dinkum velocity plot (Figure 9), which exhibits a strong seasonal modulation with the presence or absence of the landfast ice, which dramatically changes the surface stress. The model underestimates the small remaining (1-10 cm/s) synoptic and tidal fluctuations that remain in the observed record during periods of landfast ice. In the summer months, with ice in free drift or open water, the model exhibits a similar level of variance and timing/direction of wind-forced events as those observed. With the landfast ice being imposed based on the observed climatology, the ice setup or retreat.

Near Barrow Canyon (MK1, Figure 10), up-canyon (west and south) and down-canyon (north and east) flows of approximately the same magnitude and timing are observed in both the moored and modeled time series, although the fidelity of the model in reproducing any given event's magnitude is variable. To remove tidal fluctuations and highlight fluctuations on weekly to monthly periods, the observed and modeled time series are both smoothed with a 5-day lowpass filter.

At C2 (also smoothed with a 5-day filter, Figure 5), the model performs nearly as well as at MK1, although an observed southward tendency in July and August is not picked up by the model. We speculate that this offset is due to a mis-representation of the Alaska Coastal Current during these summer months. However, it could also be due to an offset in the mean flow through Bering Strait. Inspection of the mean monthly vectors shows that this mooring site is located in a transition zone of the flow field whose magnitude and direction varies seasonally.

Tables 3, 4 and 5 show quantitative comparisons of nineteen velocity parameters based on the record length current meter timeseries. These include the mean, maximum, and variance of the east-west and north-south components of velocity; the maximum and mean speeds; the net direction; the total mean kinetic energy (MKE), the mean eddy kinetic energy (MEKE) and the ratio of these two; and four parameters based on analysis of the currents rotated to the principal axis of variation: the ratio of these two velocity components, the direction of the principal axis and the percent variance explained by each of the two components.

Table 3 reveals that the model exhibits some degree of skill in hindcasting most of the selected parameters. East/west (U velocity vector) current means are indistinguishable between the model and the moorings for at least one of the velocity components at all 19 current meter sites (95% confidence limits on the means computed with the assumption of a 72 hour decorrelation time scale (*Weingartner et al. (2005a)*)). Sixteen of the nineteen comparisons agree for the north-south velocity component and fourteen of the nineteen agree for the east-west component. The other three modeled Bering Strait sites (MA1, MA2 and MA3) agree with the observations in at least one velocity component, including the dominant northward through-strait component. The hindcast net speeds are within ± 3 cm/s at all locations except for moorings MA1, MA2, MF2, and MK1. Of the four sites with mean speed differences greater than 3 cm/s, the model underestimated the observed speed in two cases and overestimated the observed speed in two cases. Net directions are within $\pm 30^\circ$ except at sites MC1, Dinkum, and McClure, all sites that exhibit observed vector mean

3.3 Model-data comparisons

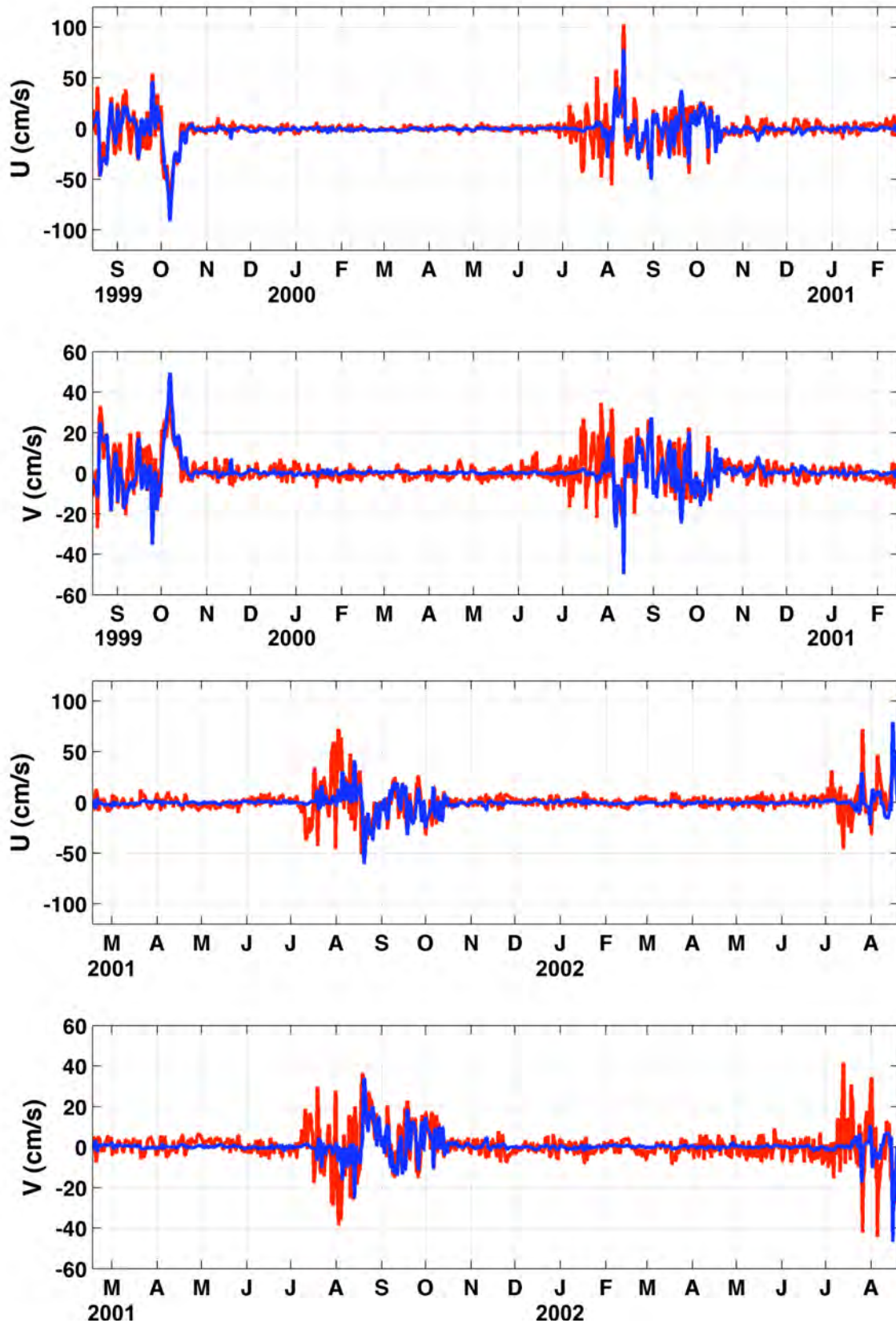


Figure 9: Modeled (blue) and observed (red) east-west (U) and north-south (V) velocities at Beaufort shelf mooring Dinkum. Observed and modeled velocities in this figure have been smoothed with a 5-day lowpass filter. 22

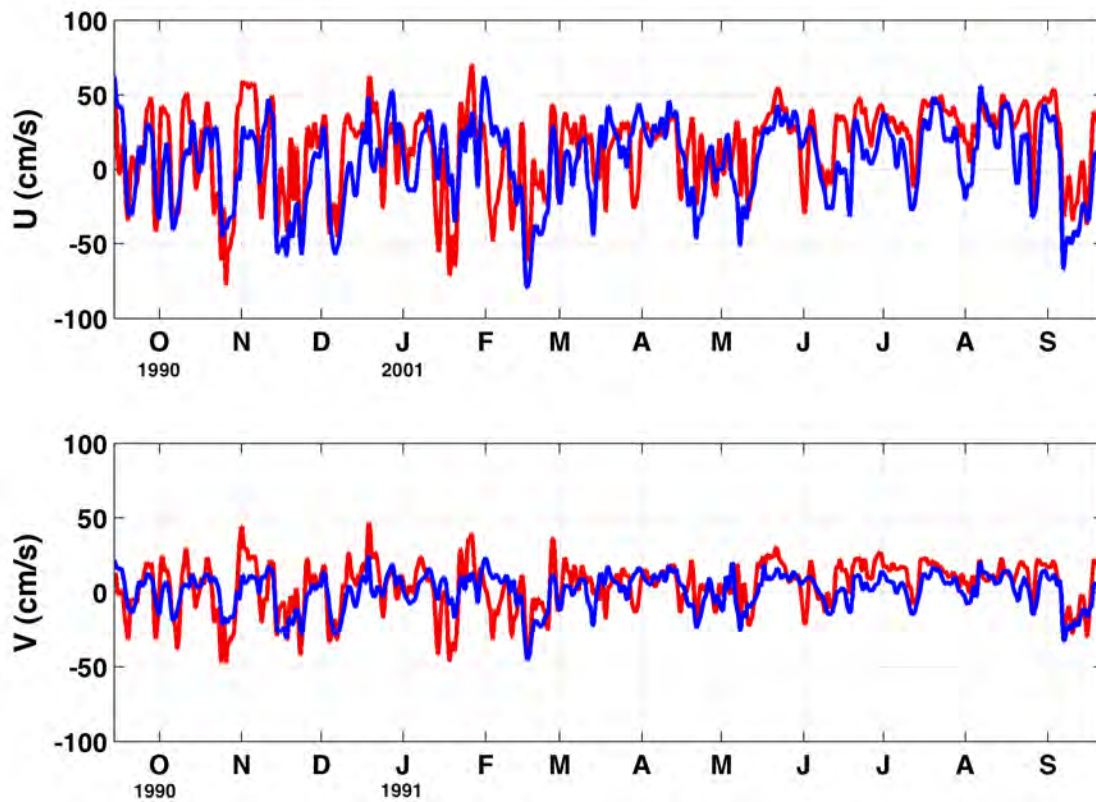


Figure 10: Modeled (blue) and observed (red) east-west (U) and north-south (V) velocities at Chukchi shelf mooring MK1. Observed and modeled velocities in this figure have been smoothed with a 5-day lowpass filter.

speeds of less than 2 cm/s. The net direction is not well resolved by either the observations or the moorings at such sites. The observational and modeled currents and variances are also shown in Figures 11.

The model is challenged in reproducing the observed MEKE:MKE ratio statistics. Of the 19 comparisons, four sites were modeled as having a ratio > 1 or < 1 when the observed ratio was opposite. Three of these are the stations in Bering Strait, where the observations exhibit a much greater tendency for EKE than the model showed. Only three ratios agreed to within a factor of 2 of each other; thirteen were within a factor of 4. Eleven of the comparisons show the observed MKE greater than the modeled and the remaining seven show the modeled MKE greater. The observations show a consistently higher level of EKE: 16 of the 19 sites are larger.

The principal axis of variation measures show that the first eigenvector accounts for 64.4% to 98.6% from the moorings and 71.9% to 99.5% from the model. For all sites, the model reproduces the observed fraction to within $\pm 10\%$ except at mooring MF2 and C2, where the differences are +16.5% and -16.2% respectively.

3.3.2 Temperature and Salinity

Temperature and salinity model-data comparisons for the mid-winter (February-March) and late summer (August-September) time intervals are shown in Table 6. Hindcasting accurate seasonal cycles of these parameters is a particular challenge on shallow Arctic shelves because of the strong influence that freezing and melting processes impart upon the shelf waters. Accurate boundary conditions and surface fluxes between the ocean and the atmosphere are generally lacking. For example, *Walsh et al.* (2009) shows that hindcast surface heat fluxes commonly exhibit biases of 160 W/m^2 , primarily due to the inability of most reanalysis products to properly represent low level cloud cover. Both shortwave and long-wave downwelling hindcasts in the reanalysis products often exhibit cloud-dependent biases of up to $\pm 40 \text{ W/m}^2$ (*Walsh et al.* (2009)). Such biases can quickly translate into excessive or insufficient freezing, and thereby create too much or too little ice cover and associated biases in the shelf salinities. Nonetheless, we show below that the hindcast model is able to reproduce many observed characteristics of both the annual cycle and synoptic-scale variations of these parameters at many of the mooring sites.

Figures 12–15 show examples of the record length observed temperature and salinity time series from one site in the Beaufort Sea (Dinkum), one site in the northeast Chukchi Sea (MK1), one site in the western Chukchi Sea (MF2) and one site in the southern Chukchi Sea near Bering Strait (MA3).

In Bering Strait, where the T/S properties are strongly influenced by the southern boundary conditions, temperatures remain somewhat ($< 2^\circ\text{C}$) too warm through the winter months (Figure 12) and up to about 4°C too warm in summer months). Large mid-winter salinity fluctuations are exhibited by the model that are not observed in the moored dataset. The

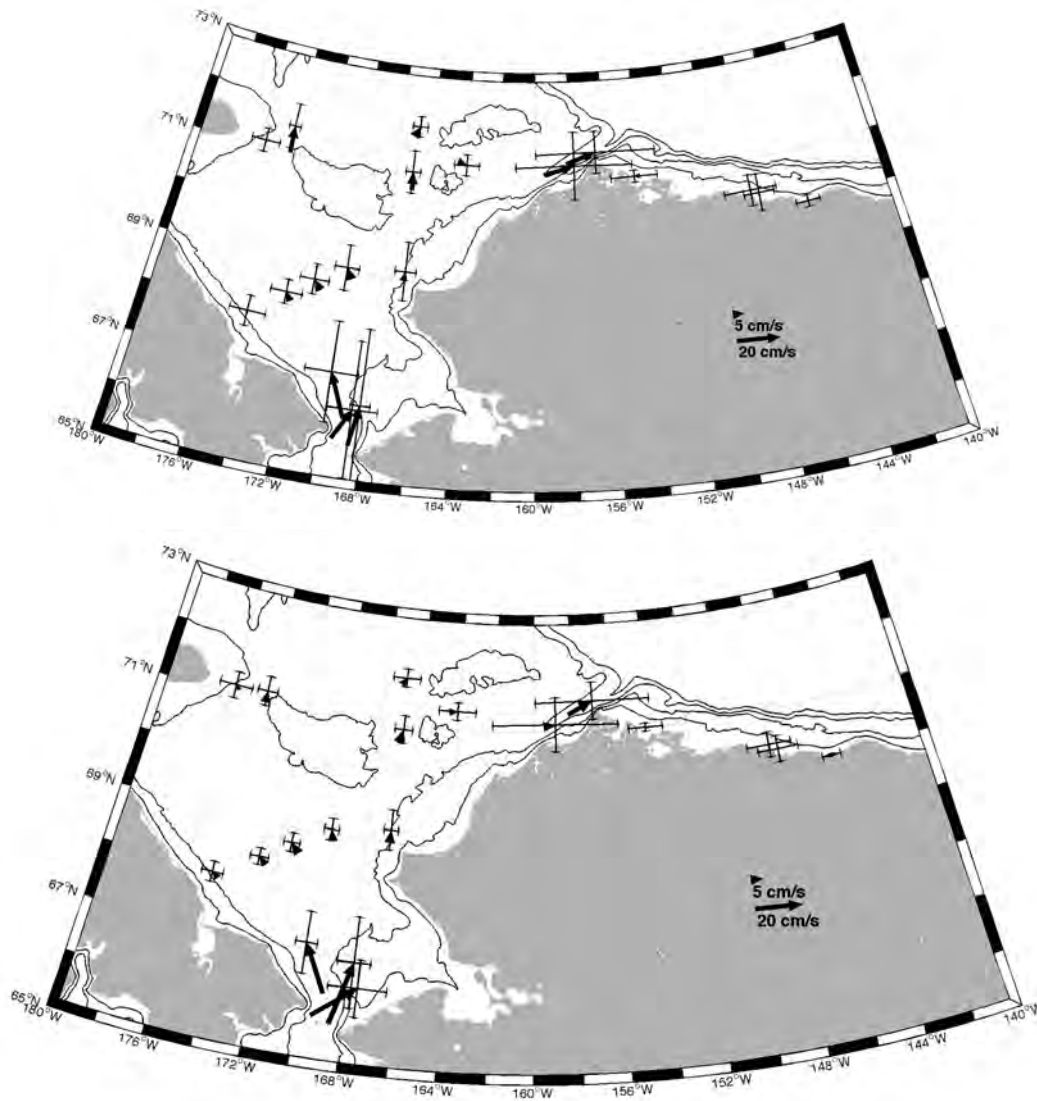


Figure 11: Chukchi and Beaufort flow field as represented by the moored observations at the 19 comparison sites in Table 2 (top) and numerical model (bottom). Vectors depict the record length mean velocities. Cross-hairs depict one standard deviation in the U and V velocity components.

3.3 Model-data comparisons

Table 3: Statistics of the current meter moorings and model hindcasts at the mooring locations. Columns represent the moorings described in Table 2. Rows represent the observed (obs) and modeled (mod) east-west velocity (U) and north-south velocity (V) mean, minimum (min), maximum (max), variance (var), maximum observed speed (max Spd), mean speed (mean Spd), vector mean net speed (Net Spd) and direction (Net Dir), mean kinetic energy (MKE), mean eddy kinetic energy (MEKE), kinetic energy ratio (KE ratio), principal axis (PA) of variation ratio, PA orientation (theta), and the percent variance explained by each of the two eigenvectors (Obs % Var for Eig 1 and Eig 2). Mean U and V predicted and observed velocities that are not statistically distinguishable from each other based on overlapping 95% confidence limits for the mean are highlighted in bold type.

		MA1	MA2	MA3	MC1	MC2	MC3	MC4	MC6	MF1	MF2	MK1	C1	C2	C3	EBC	Camden	Dinkum	McClure	Smith
U mean	obs	7.84	3.31	-8.17	0.15	-2.44	-3.4	-2.62	0.47	-0.17	-0.47	13.8	-0.27	4.18	2.37	13.4	-0.28	-0.24	0.12	-2.62
	mod	18.09	7.26	-9.98	-2.73	-3.11	-3.44	-1.03	0.12	-1.59	0.02	4.9	1.42	3.4	2.05	10.2	-0.9	-0.78	-0.6	-1.38
V mean	obs	14.4	19.2	20.7	1.18	3.78	4.61	4.76	4.1	0.44	12.43	4.05	8.24	-1.4	4.65	5.08	-0.05	0.62	1.34	-0.06
	mod	14.1	27.2	20.5	2.18	2.87	3.95	4.68	5.17	1.59	4.75	0.85	5.82	0.52	2.86	5.74	0.12	0.38	0.39	0.36
U min	obs	-32.3	-13.5	-30.3	-52.9	-37.8	-28.3	-30.4	-23.6	-24.7	-18.5	-77.2	-40.3	-21.1	-18.6	-107	-28.34	-83.85	-49.48	-72.16
	mod	-19.7	-7.01	-21.6	-24.9	-20.1	-17.6	-18.6	-18.3	-31.1	-31	-79.2	-18.5	-22	-16.8	-69	-23.18	-90.92	-70.73	-50.09
U max	obs	50.44	23.56	44.09	39.47	31.41	28.48	17.07	20.51	29.1	18.4	70.23	13.34	30.29	18.55	78.54	23.22	103.24	59.47	31.42
	mod	54.72	35.7	9.34	19.89	11.61	8.63	9.11	17.12	12.92	12.67	62.19	15	28.76	20.42	70.26	20.41	79.32	69.84	17.39
V min	obs	-101	-107	-80.2	-32	-20	-32	-49.5	-57.4	-23.8	-24.2	-47.2	-25.1	-15.6	-20.8	-37.9	-12.37	-47.01	-66	-13.49
	mod	-23.5	-26.5	-19.6	-19.5	-14.3	-10.7	-11.4	-27.6	-21.4	-17.9	-44.9	-13.6	-15.3	-21.9	-18.6	-4.87	-49.54	-40.97	-4.81
V max	obs	115.5	132.6	96.69	26.32	32.98	23.88	33.26	52.17	24.86	40.51	46.86	46.76	18.61	22.5	37.17	16.66	41.51	63.37	25.52
	mod	66.94	103.5	73.43	27.21	16.3	18.77	22.49	40.05	27.61	25.37	24.6	31.77	21.25	24.23	27.77	4.03	49.63	52.53	13.36
U var	obs	147	23.59	166.5	78.2	59.18	50.57	35.85	27.19	47.66	8.85	739	13.32	37.46	14.08	776.7	34.36	153.21	53.28	122.3
	mod	166.3	54.43	24.21	24.1	17.74	13.77	11.8	11.47	53.15	20.18	722.9	16.36	66.23	36.12	588.3	18.08	92.62	77.34	55.88
V var	obs	1054	1316	576.9	55.97	36.46	52.75	115.4	191.1	32.93	116.9	259.7	103.5	27.6	25.44	103.4	9.39	56.85	80.73	9.54
	mod	157.8	391.6	184.5	21.69	14.71	18.62	24.1	76.07	35.33	42.66	138.1	37.75	16.15	16.94	67.34	0.66	31.86	34.76	4.05
Max Spd	obs	125.9	132.9	98.83	55.65	40.12	35.25	50.1	57.4	36.27	40.7	90.47	46.76	30.64	29.04	112.7	30.07	113.22	80.26	72.26
	mod	86.46	109.1	75.85	36.9	23.45	23.17	23.03	43.47	37.38	31.27	90.69	35.11	30.18	25.33	75.39	23.53	103.59	88.1	51.62
Mean Spd	obs	30.25	34.03	30.6	8.69	8.64	10.14	11.02	12.28	7.08	13.77	30.53	10.82	7.92	6.68	26.69	3.8	8.73	6.8	6.21
	mod	24.48	29.52	23.83	6.03	6.11	6.84	6.74	8.85	7.18	7.72	25.31	8.06	8.13	6.86	23.18	2.26	4.89	4.59	3.91
Net Spd	obs	16.43	19.43	22.22	1.19	4.5	5.73	5.43	4.12	0.48	12.44	14.42	8.24	4.41	5.22	14.35	0.28	0.66	1.35	2.62
	mod	22.93	28.14	22.79	3.49	4.23	5.24	4.8	5.17	2.25	4.75	4.97	5.99	3.44	3.52	11.7	0.91	0.86	0.71	1.43
Net Dir	obs	28	10	338	7	327	324	331	7	339	358	74	358	109	27	69	259	339	5	269
	mod	52	15	334	309	313	319	348	1	315	0	80	14	81	36	61	277	296	303	285
MKE	obs	135	188.8	246.8	0.71	10.13	16.41	14.73	8.5	0.11	77.34	104	33.95	9.72	13.61	103	0.04	0.22	0.91	3.43
	mod	262.8	396	259.8	6.09	8.96	13.73	11.5	13.37	2.53	11.29	12.35	17.94	5.91	6.19	68.43	0.41	0.37	0.25	1.03
MEKE	obs	600.4	669.7	371.6	67.08	47.82	51.65	75.63	109.1	40.28	62.89	499.3	58.42	32.53	19.76	440	21.88	105.03	67	65.91
	mod	162	223	104.4	22.9	16.22	16.19	17.95	43.76	44.22	31.41	430.4	27.05	41.19	26.53	327.8	9.36	62.24	56.05	29.96
KE ratio	obs	4.45	3.55	1.51	94.27	4.72	3.15	5.13	12.84	357.1	0.81	4.8	1.72	3.35	1.45	4.27	554.48	479.13	73.88	19.22
	mod	0.62	0.56	0.4	3.76	1.81	1.18	1.56	3.27	17.5	2.78	34.85	1.51	6.97	4.28	4.79	22.58	167.84	221.72	29.22
PA ratio	obs	0.12	0.12	0.22	0.3	0.53	0.6	0.53	0.38	0.49	0.26	0.12	0.36	0.74	0.47	0.16	0.22	0.15	0.29	0.24
	mod	0.21	0.11	0.17	0.17	0.44	0.63	0.61	0.25	0.45	0.55	0.09	0.34	0.49	0.62	0.07	0.07	0.06	0.06	0.07
PA theta	obs	19	177	154	129	122	136	170	2	54	176	60	2	61	32	72	116	121	142	98
	mod	46	20	162	133	131	145	21	17	54	24	67	30	94	72	72	100	120	124	105
Obs % Var	Eig 1	98.57	98.52	95.37	91.74	77.93	73.55	77.89	87.66	80.84	93.46	98.57	88.69	64.43	81.76	97.49	95.42	97.84	92.42	94.4
	Eig 2	1.43	1.48	4.63	8.26	22.07	26.45	22.11	12.34	19.16	6.54	1.43	11.31	35.57	18.24	2.51	4.58	2.16	7.58	5.6
Mod. % Var	Eig 1	95.85	98.79	97.33	97.04	83.63	71.28	72.85	94.24	83.29	76.97	99.27	89.9	80.67	72.4	99.5	99.52	99.68	99.66	99.49
	Eig 2	4.15	1.21	2.67	2.96	16.37	28.72	27.15	5.76	16.71	23.03	0.73	10.1	19.33	27.6	0.5	0.48	0.32	0.34	0.51

3.3 Model-data comparisons

Table 4: Statistics of the current meter moorings and model hindcasts for August and September. Rows represent the observed (obs) and modeled (mod) east-west velocity (U) and north-south velocity (V) mean, minimum (min), maximum (max), variance (var), maximum observed speed (max Spd), mean speed (mean Spd), vector mean net speed (Net Spd) and direction (Net Dir), mean kinetic energy (MKE), mean eddy kinetic energy (MEKE), kinetic energy ratio (KE ratio), principal axis (PA) of variation ratio, PA orientation (theta), and the percent variance explained by each of the two eigenvectors (Obs % Var for Eig 1 and Eig 2). Mean U and V predicted and observed velocities that are not statistically distinguishable from each other based on overlapping 95% confidence limits for the mean are highlighted in bold type.

		MA1	MA2	MA3	MC1	MC2	MC3	MC4	MC6	MF1	MF2	MK1	C1	C2	C3	EBC	Camden	Dinkum	McClure	Smith
U mean	obs	9.37	3.52	-11.7	0.21	-3.76	-2.67	-2.65	1.55	-3.11	-2.08	18.52	-1.02	4.48	1.41	33.8	0.12	1.06	0.89	-3.86
	mod	7.34	6.49	-9.7	-3.39	-3.59	-1.92	-1.24	0.27	1.54	0.7	5.06	0.58	0.61	-0.37	9.48	0.09	0.72	1.01	-2.54
V mean	obs	18.49	12.67	23.86	1.4	3.48	4.66	3.21	3.96	-1.48	19.46	4.4	5.66	-5.68	3.45	12.39	-0.23	1.33	1.23	0.97
	mod	4.99	25.9	19.48	2.19	2.59	1.93	3.57	4.69	1.93	5.72	0.62	4.04	0.49	2.09	6.09	-0.21	-0.7	-0.34	0.81
U min	obs	0.12	-8.52	-26.57	-19.71	-20.98	-11.39	-20.04	-17.52	-13.45	-13.77	-41.29	-6.69	-2.4	-5.13	-22.55	-26.38	-55.94	-49.48	-59.87
	mod	-6.27	-3	-20.15	-14.46	-12.58	-7.38	-6.81	-7.88	-5.84	-11.31	-66.8	-5.93	-18.35	-15.22	-39.78	-13.58	-60.07	-47.09	-20.93
U max	obs	13.12	15.05	20.84	29.38	24	14.59	12.74	20.16	8.5	5.69	53.45	3.79	13.13	10.49	78.54	19.77	103.24	58.9	31.42
	mod	24.82	27.16	7.04	8.6	6.94	3.46	3.22	8.88	5.05	10.92	61.48	6.52	16.24	20.42	49.73	20.41	79.32	69.84	17.39
V min	obs	-15.78	-41.31	-25.92	-22.91	-14.72	-6.66	-9.27	-26.03	-7.37	-8.22	-31.04	-12.2	-15.5	-5.81	-7.03	-11	-47.01	-66	-10.07
	mod	-5.68	-12.83	-15.86	-13	-8.02	-4.06	-6.78	-15.94	-3.22	-17.93	-32.69	-6.76	-6.84	-9.49	-7.77	-4.87	-49.54	-40.97	-4.81
V max	obs	50.75	89.37	67.63	18.32	11.38	10.27	20.15	33.96	5.16	36.62	25.62	26.93	1.11	18.9	33.57	14.75	36.65	37.71	15.28
	mod	16.04	74.71	48.9	10.5	10.13	7.85	11.3	23.07	5.16	23.15	21.07	18.03	6.49	13.09	20.83	2.86	34.12	31.37	6.57
U var	obs	12.66	27.09	126.4	80.26	53.61	25.33	20.6	37.25	45.41	4.65	668.65	3.23	14.91	6.09	446.23	109.93	490.89	152.84	199.18
	mod	73.11	43.15	37.29	17.41	15.95	7.12	5.02	7.04	8.23	15.7	886.54	5.93	59.31	67.23	651.08	81.19	339.3	266.57	99.1
V var	obs	369.92	608.1	351.5	61.34	32.95	10.16	33.08	148	10.11	102.45	215.99	61.49	13.42	14.3	107.56	25.17	185.45	237.28	22.35
	mod	25.46	416.7	196.2	18.2	13.72	8.6	15.88	51.75	4.75	82.79	147.8	34.99	9.31	21.13	74.84	3.2	123.64	110.27	8.24
Max Spd	obs	52.38	89.55	69.7	33	27.87	16.01	22.03	35.3	14.89	36.72	57.37	27.4	15.56	19.61	84.78	28.56	113.22	80.26	59.87
	mod	29.55	79.45	52.08	16.84	14.02	9.67	11.3	24.33	7.22	25.6	74.17	19.06	18.36	22.73	53.45	20.99	92.72	80.97	21.63
Mean Spd	obs	24.5	23.67	30.67	9.48	9.31	7.62	7.07	12.31	7.21	20.28	31.93	7.44	8.15	4.47	37.33	9.75	21.32	16.15	12.69
	mod	11.07	28.09	23.6	6.24	6.22	4.36	5.31	7.71	3.92	10.05	28.33	6.55	7.24	8.29	25.09	7.97	16.21	14.91	9.18
Net Spd	obs	20.73	13.15	26.57	1.41	5.12	5.37	4.17	4.25	3.45	19.57	19.03	5.75	7.24	3.73	36	0.26	1.7	1.52	3.98
	mod	8.88	26.7	21.76	4.04	4.42	2.72	3.78	4.69	2.47	5.76	5.1	4.08	0.79	2.12	11.26	0.23	1	1.07	2.66
Net Dir	obs	27	16	334	8	313	330	320	21	245	77	350	142	22	70	153	39	36	284	
	mod	56	14	334	303	306	315	341	3	39	7	83	8	51	350	57	156	134	109	288
MKE	obs	214.84	86.44	352.9	1	13.1	14.41	8.68	9.04	5.94	191.43	181.16	16.53	26.18	6.95	647.93	0.03	1.44	1.15	7.91
	mod	39.39	356.5	236.7	8.16	9.78	3.7	7.15	11.02	3.05	16.61	13	8.33	0.31	2.25	63.43	0.03	0.5	0.57	3.54
MEKE	obs	189.96	317.1	238.7	70.76	43.25	17.72	26.81	92.55	27.63	53.52	442.05	32.33	14.15	10.19	276.64	67.47	338.1	195	110.62
	mod	48.94	229.6	116.7	17.79	14.82	7.85	10.44	29.38	6.46	49.22	516.86	20.44	34.28	44.14	362.63	42.14	231.42	188.36	53.6
KE ratio	obs	0.88	3.67	0.68	70.79	3.3	1.23	3.09	10.23	4.65	0.28	2.44	1.96	0.54	1.47	0.43	2000.39	234.24	169.54	13.98
	mod	1.24	0.64	0.49	2.18	1.52	2.12	1.46	2.67	2.12	2.96	39.76	2.45	110.5	19.6	5.72	1582.67	462.28	331.2	15.14
PA ratio	obs	0.12	0.17	0.24	0.37	0.69	0.51	0.69	0.5	0.47	0.21	0.12	0.21	0.91	0.37	0.13	0.15	0.1	0.28	0.28
	mod	0.14	0.09	0.15	0.21	0.3	0.6	0.51	0.26	0.25	0.29	0.07	0.25	0.29	0.45	0.06	0.04	0.06	0.05	0.07
PA theta	obs	8	173	151	130	114	111	24	179	90	179	61	175	62	29	65	114	121	142	100
	mod	60	17	158	136	132	141	13	15	54	18	68	18	105	71	72	101	121	123	106
Obs % Var	Eig 1	98.59	97.13	94.6	87.87	67.88	79.1	67.49	79.9	81.8	95.68	98.53	95.81	54.64	88.22	98.23	97.66	99	92.88	92.52
	Eig 2	1.41	2.87	5.4	12.13	32.12	20.9	32.51	20.1	18.2	4.32	1.47	4.19	45.36	11.78	1.77	2.34	1	7.12	7.48
Mod. % Var	Eig 1	98.2	99.28	97.86	95.89	91.68	73.74	79.13	93.79	94.16	92.14	99.53	94.07	92.03	82.97	99.67	99.84	99.62	99.75	99.48
	Eig 2	1.8	0.72	2.14	4.11	8.32	26.26	20.87	6.21	5.84	7.86	0.47	5.93	7.97	17.03	0.33	0.16	0.38	0.25	0.52

3.3 Model-data comparisons

Table 5: Statistics of the current meter moorings and model hindcasts for February and March. Rows represent the observed (obs) and modeled (mod) east-west velocity (U) and north-south velocity (V) mean, minimum (min), maximum (max), variance (var), maximum observed speed (max Spd), mean speed (mean Spd), vector mean net speed (Net Spd) and direction (Net Dir), mean kinetic energy (MKE), mean eddy kinetic energy (MEKE), kinetic energy ratio (KE ratio), principal axis (PA) of variation ratio, PA orientation (theta), and the percent variance explained by each of the two eigenvectors (Obs % Var for Eig 1 and Eig 2). Mean U and V predicted and observed velocities that are not statistically distinguishable from each other based on overlapping 95% confidence limits for the mean are highlighted in bold type.

		MA1	MA2	MA3	MC1	MC2	MC3	MC4	MC6	MF2	MK1	C1	C2	C3	EBC	Camden	Dinkum	McClure	Smith
U mean	obs	7.09	2.57	-0.8	0.49	-0.1	-1.06	-0.44	-0.17	0.52	2.34	0.67	4.26	2.43	8.63	-0.22	0.02	-0.2	-0.26
	mod	17.03	6.19	-9.64	-2.91	-3.01	-3.1	-0.39	-0.96	-0.25	1.76	1.4	3.59	2.11	13.89	-0.59	-0.68	-0.39	0.06
V mean	obs	9.36	15.06	7.71	1.33	1.6	3.17	1.57	0.31	4.69	-1.12	8.09	0.38	3.64	2.37	0	-0.35	1.23	-0.55
	mod	13.89	24.44	18.43	2.61	2.78	4.17	4.58	3.2	4.35	-0.6	4.64	-0.39	2.47	5.97	0.15	0.32	0.07	-0.02
U min	obs	-32.3	-5.7	-18.91	-5.94	-9.4	-28.34	-25.17	-23.58	-5.55	-61.42	-7.25	-21.1	-13.82	-103.4	-2.34	-9.21	-3.49	-6.67
	mod	-1.94	-2.49	-20.68	-11.76	-20.05	-17.55	-18.61	-18.28	-15.87	-79.17	-18.47	-20.7	-16.8	-36.75	-3.69	-5.86	-3.87	-3.96
U max	obs	48.24	11.38	31.35	12.7	15.37	17.12	15.92	8.55	6.2	43.25	7.08	16.65	8.31	52.15	2.22	13.06	6.31	7.45
	mod	46.8	22.12	-3.45	4.04	6.08	7.52	9.11	7.51	9.22	57.69	10.46	23.69	16.6	70.26	1.62	4.06	2.61	3.35
V min	obs	-101.42	-107.3	-80.18	-6.95	-8.28	-16.43	-24.77	-27.53	-7.84	-45.09	-11.76	-5.54	-6.87	-37.92	-2.26	-8.6	-7.78	-6.39
	mod	-0.46	-0.76	-0.06	-3.72	-3.39	-4.87	-11.35	-15.78	-8.34	-44.9	-4.59	-10.4	-7.24	-7.49	-0.26	-2.25	-1.97	-1.88
V max	obs	90.12	69.77	50.7	8.63	9.71	13.84	18.87	35.85	12.17	36.42	29.13	15.43	14.37	21.12	2.36	5.77	7.56	5.14
	mod	38.95	62.69	47.26	10.54	8.48	11.77	17.94	25.32	17.67	22.68	13.9	11.06	13.05	27.77	0.77	3.3	2.43	1.35
U var	obs	219.97	9.32	126.7	11.66	21.85	46.46	28.64	15.67	4.43	581.96	3.83	28.84	10.59	427	0.5	14.07	2.39	5.09
	mod	130.82	32.29	11.36	10.14	19.2	20.02	22.06	13.91	22.26	885.24	17.97	55.56	30.94	506.8	0.62	1.45	0.77	2.34
V var	obs	1263.32	1358	688.2	8.63	15.62	38.15	73.24	139.6	26.76	202.02	57.62	11.24	12.02	53.26	0.61	7.13	6.66	3.9
	mod	77.38	163.4	121.6	7.43	5.49	11.68	22.61	67.42	25.94	197.4	15.9	15.82	9.81	61.18	0.03	0.41	0.32	0.28
Max Spd	obs	106.39	107.4	85.83	14.41	17.41	29.45	26.89	35.86	12.56	74.79	29.41	21.4	15.13	109.6	3.03	14.91	9.98	7.69
	mod	59.86	66.31	49.81	15.78	20.63	17.56	19.03	25.59	19.64	90.69	18.51	23.77	19.7	75.39	3.72	6.7	4.55	4.11
Mean Spd	obs	30.96	33.18	24.57	3.67	5.16	8.43	8.64	9.88	6.83	24.11	8.99	6.3	5.62	17.2	0.96	3.82	2.74	2.77
	mod	22.22	25.39	21.23	4.81	5.42	6.83	7.34	8.32	7.06	27.2	6.31	7.66	6.1	22.7	0.77	1.27	0.91	1.35
Net Spd	obs	11.75	15.28	7.75	1.42	1.6	3.34	1.63	0.35	4.72	2.6	8.12	4.27	4.38	8.95	0.22	0.35	1.25	0.61
	mod	21.97	25.21	20.8	3.91	4.09	5.19	4.6	3.34	4.36	1.86	4.85	3.61	3.25	15.12	0.61	0.75	0.39	0.07
Net Dir	obs	37	10	354	20	356	341	344	331	6	116	5	85	34	75	270	176	351	205
	mod	51	14	332	312	313	323	355	343	357	109	17	96	40	67	285	295	280	112
MKE	obs	69	116.7	30.05	1	1.28	5.57	1.33	0.06	11.12	3.37	32.99	9.13	9.57	40.06	0.02	0.06	0.78	0.19
	mod	241.35	317.9	216.3	7.64	8.38	13.49	10.58	5.59	9.49	1.73	11.75	6.53	5.27	114.4	0.19	0.28	0.08	0
MEKE	obs	741.12	683	407.2	10.14	18.72	42.27	50.9	77.57	15.58	391.71	30.7	20.03	11.3	240	0.56	10.6	4.52	4.49
	mod	104.02	97.79	66.45	8.78	12.34	15.84	22.32	40.63	24.08	540.94	16.92	35.66	20.36	283.8	0.32	0.93	0.55	1.31
KE ratio	obs	10.74	5.85	13.55	10.1	14.63	7.59	38.29	1253	1.4	116.26	0.93	2.19	1.18	5.99	23	174.01	5.82	23.98
	mod	0.43	0.31	0.31	1.15	1.47	1.17	2.11	7.27	2.54	312.96	1.44	5.46	3.86	2.48	1.73	3.27	7.06	589.81
PA ratio	obs	0.1	0.08	0.15	0.32	0.34	0.38	0.47	0.32	0.34	0.12	0.18	0.49	0.61	0.17	0.7	0.19	0.28	0.84
	mod	0.19	0.09	0.18	0.21	0.38	0.65	0.63	0.31	0.61	0.07	0.37	0.5	0.56	0.07	0.12	0.1	0.12	0.25
PA theta	obs	22	178	158	130	129	131	157	6	13	60	11	68	41	73	37	125	152	109
	mod	53	24	166	130	111	115	44	18	40	65	47	101	96	71	100	118	122	103
Obs % Var	Eig 1	98.98	99.42	97.83	90.76	89.46	87.38	81.72	90.76	89.8	98.56	96.95	80.92	72.82	97.33	67.17	96.65	92.61	58.36
	Eig 2	1.02	0.58	2.17	9.24	10.54	12.62	18.28	9.24	10.2	1.44	3.05	19.08	27.18	2.67	32.83	3.35	7.39	41.64
Mod. % Var	Eig 1	96.67	99.13	96.87	95.89	87.38	70.53	71.43	91.1	72.7	99.45	87.99	79.85	76.42	99.57	98.54	99.09	98.55	94.15
	Eig 2	3.33	0.87	3.13	4.11	12.62	29.47	28.57	8.9	27.3	0.55	12.01	20.15	23.58	0.43	1.46	0.91	1.45	5.85

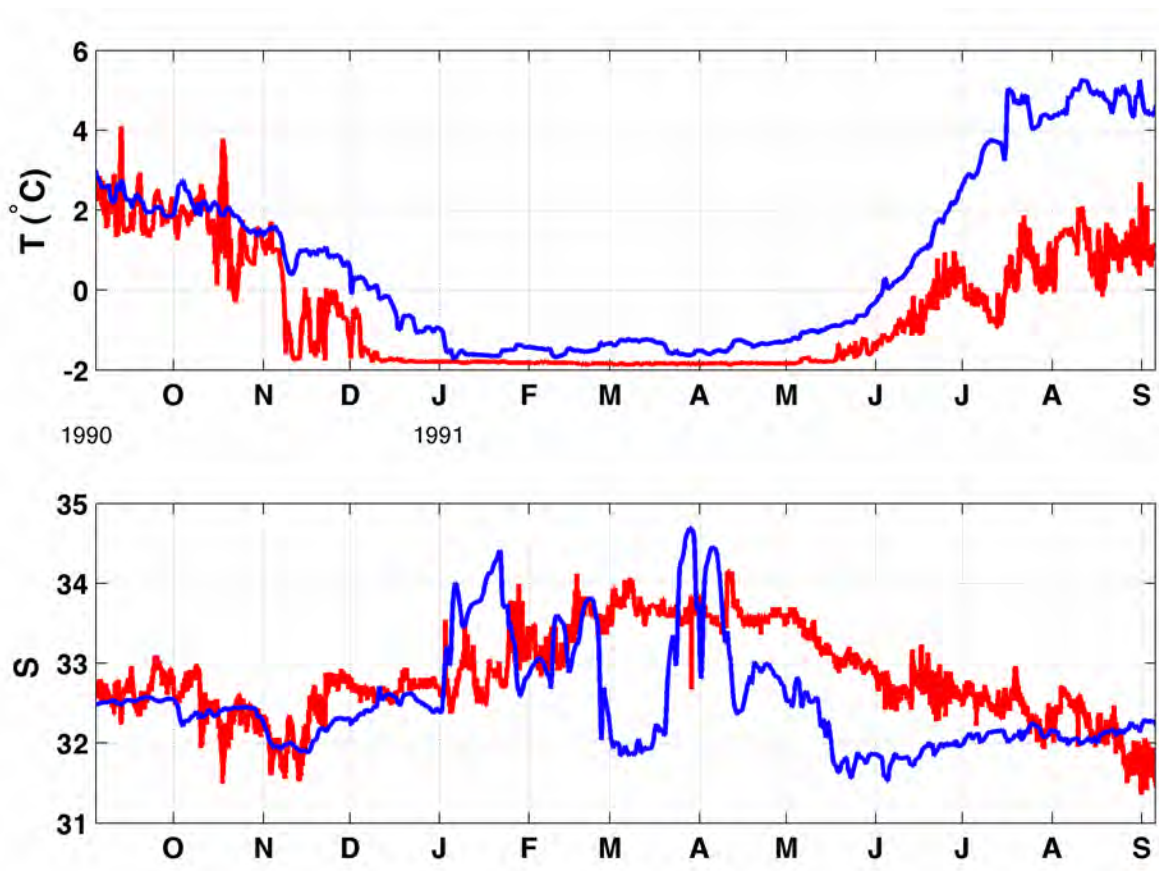


Figure 12: Modeled (blue) and observed (red) water temperature (T) and salinity (S) at Bering Strait mooring MA3.

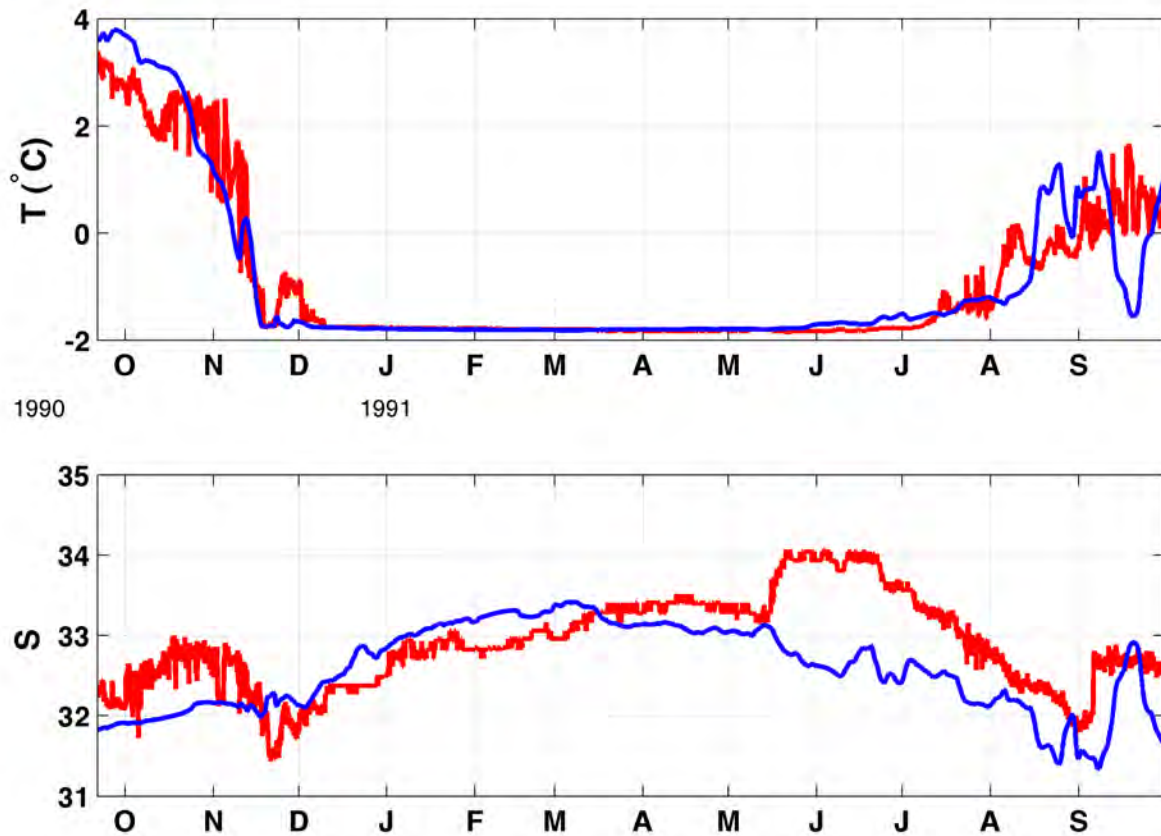


Figure 13: Modeled (blue) and observed (red) water temperature (T) and salinity (S) at Western Chukchi mooring MF2.

majority of the Bering Strait transport is advected through Herald Canyon in the western Chukchi Sea. Mooring MF2 (Figure 13) shows that despite the differences in temperature and salinity at mooring MA3, the modeled MF2 annual cycle very closely conforms to that observed. At the Barrow Canyon site, MK1, the model captures some of the fluctuating T/S properties associated with up-canyon and down-canyon flow events (Figure 14). However, the model shows extremely salty excursions ($S > 36$) associated with down-canyon flow events that may reflect excessive ice formation in the model in this region (see sea ice results below for supporting evidence).

Qualitatively, at the Dinkum mooring site (Figure 15), we see that the model reproduces the approximate magnitude and timing of the seasonal cycle in both the temperature and salinity fields. In addition, some of the synoptic scale variations are also reproduced. The most pronounced difference between the modeled and observed fields are the low salinity excursions during August, which are not well reproduced by the model and the warm temperature pulses observed in August 2000 and August 2002. These features are undoubtedly due to the Alaskan north slope rivers that discharge into the nearshore Beaufort Sea. While

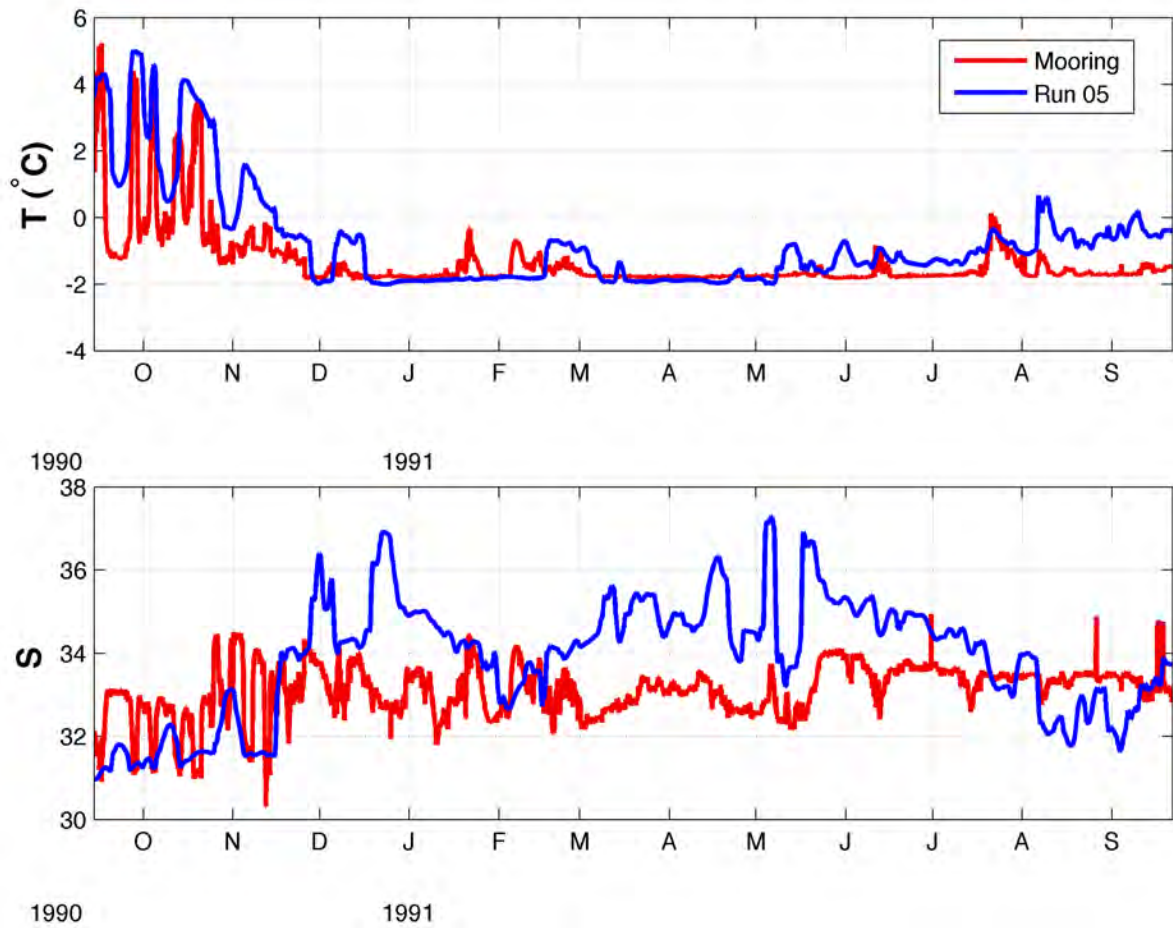


Figure 14: Modeled (blue) and observed (red) water temperature (T) and salinity (S) at Barrow Canyon mooring MK1.

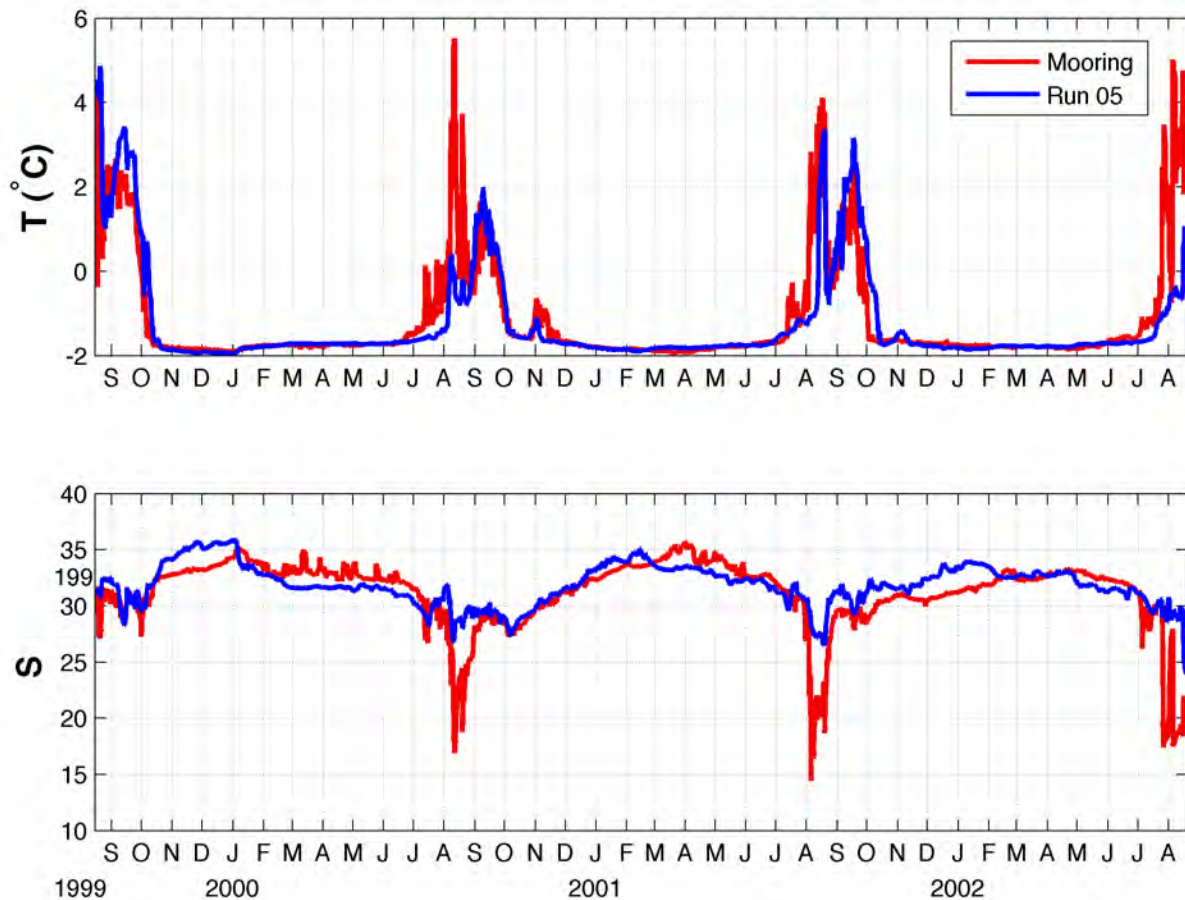


Figure 15: Modeled (blue) and observed (red) water temperature (T) and salinity (S) at Beaufort shelf mooring Dinkum.

the implementation of coastal discharge (a function of the monthly mean discharge field applied to the model for fresh water forcing) is not able to capture the magnitude of this signal, we note that a muted amplitude response but with the correct timing did occur in 2001 and to a lesser degree in 2000.

Table 6 shows that the winter modeled temperatures are generally within 0.5°C of the observations, and the freezing point of seawater. Near the southern Bering Strait boundary the incoming salinities are typically too fresh (by about 1–2 psu), showing a need for better southern boundary conditions. However, over the northeast Chukchi Sea, salinities are too salty by up to 2 psu, suggesting too much freezing and brine rejection takes place over the Chukchi Shelf. Mean modeled winter salinities in the Beaufort Sea are within 1.5 of those observed. In late summer, largest errors are again near the southern boundary: modeled temperatures are generally within 2°C of those observed except at moorings MA1 and MC1, where the modeled offset is about $+4^{\circ}\text{C}$.

3.3 Model-data comparisons

Table 6: Statistics of winter (top panel) and late summer (bottom panel) temperature (T) and salinity (S) mooring data and model hindcasts. Rows depict the mean, minimum, maximum and variance computed over these two-month intervals for each parameter.

		February-March															
		MA1	MA2	MA3	MC1	MC2	MC3	MC4	MC6	MF2	MK1	C1	C2	C3	Argo	Dinkum	McClure
T mean	obs	-1.91	-1.85	-1.84	-1.80	-1.82	-1.83	-1.83	-1.85	-1.81	-1.61	-1.72	-1.74	-1.74	-1.75	-1.81	-1.90
	mod	-1.33	-1.46	-1.44	-1.78	-1.75	-1.79	-1.88	-1.94	-1.81	-1.56	-1.74	-1.75	-1.73	-1.82	-1.78	-1.78
T min	obs	-1.95	-1.90	-1.89	-1.83	-1.83	-1.85	-1.83	-1.92	-1.83	-1.82	-1.80	-1.76	-1.76	-1.84	-1.97	-1.95
	mod	-1.69	-1.79	-1.68	-1.80	-1.78	-1.86	-1.92	-2.06	-1.82	-1.94	-1.80	-1.76	-1.75	-1.98	-1.91	-1.85
T max	obs	-1.86	-1.72	-1.80	-1.78	-1.79	-1.81	-1.81	-1.78	-1.78	-0.68	-1.16	-1.72	-1.71	-1.63	-1.72	-1.85
	mod	-1.09	-1.18	-1.23	-1.77	-1.61	-1.68	-1.79	-1.89	-1.80	-0.68	-1.69	-1.73	-1.70	-1.74	-1.72	-1.73
T var	obs	0.00	0.00	0.00	0.00	0.00	0.00	0.00	0.00	0.00	0.07	0.02	0.00	0.00	0.00	0.00	0.00
	mod	0.03	0.03	0.02	0.00	0.00	0.00	0.00	0.00	0.00	0.19	0.00	0.00	0.00	0.00	0.00	0.00
S mean	obs	33.81	33.54	33.52	32.53	33.23	33.27	33.01	33.77	33.07	32.97	29.74	31.63	31.71	33.37	33.29	34.09
	mod	31.72	33.17	32.92	32.82	32.61	33.42	34.56	35.64	33.26	34.25	32.48	32.13	31.90	33.45	32.83	32.78
S min	obs	33.03	33.03	32.68	32.02	33.06	33.06	32.79	31.72	32.72	32.08	29.19	31.37	31.57	31.65	31.78	33.19
	mod	31.52	31.84	31.84	32.61	32.41	32.55	32.91	34.71	33.11	32.66	31.90	31.86	31.25	32.00	31.57	31.87
S max	obs	34.75	34.23	34.12	33.33	33.74	33.72	33.31	34.90	33.40	34.20	29.83	32.34	32.00	36.60	35.73	35.42
	mod	32.41	35.81	34.69	33.07	32.82	34.33	35.29	37.87	33.42	35.61	33.19	32.34	32.13	36.35	35.10	34.10
S var	obs	0.17	0.05	0.08	0.11	0.01	0.02	0.01	0.49	0.03	0.20	0.02	0.04	0.01	1.06	0.73	0.50
	mod	0.02	1.22	0.67	0.02	0.02	0.48	0.31	0.57	0.01	0.69	0.09	0.02	0.06	1.08	0.76	0.43
		August-September															
		MA1	MA2	MA3	MC1	MC2	MC3	MC4	MC6	MF2	MK1	C1	C2	C3	Argo	Dinkum	McClure
T mean	obs	1.25	2.66	1.47	-0.16	0.92	1.37	1.42	4.48	0.38	-1.06	1.60	-0.78	0.50	0.96	1.17	0.65
	mod	5.20	3.99	3.69	3.50	3.54	3.91	3.11	6.20	0.42	0.45	1.85	-0.88	-0.75	1.16	0.93	0.59
T min	obs	-0.62	-0.16	-0.16	-1.69	-0.47	-0.63	0.29	0.85	-1.45	-1.79	-1.30	-1.72	-1.49	-1.41	-1.21	-1.22
	mod	2.21	2.08	1.84	0.71	1.06	0.78	0.94	2.34	-1.55	-1.10	-0.16	-1.46	-1.47	-1.36	-1.43	-1.29
T max	obs	3.32	8.66	4.09	3.05	2.95	2.84	3.03	8.60	3.39	5.23	3.20	0.75	2.75	4.28	5.52	4.03
	mod	6.99	5.50	5.26	5.63	5.36	5.71	5.44	8.81	3.79	5.01	4.52	1.76	2.37	6.08	4.86	2.79
T var	obs	0.61	4.69	0.44	2.00	0.73	0.52	0.72	3.75	1.35	2.09	1.30	0.57	1.22	1.31	1.60	1.20
	mod	1.31	0.76	1.64	2.42	2.00	2.49	1.98	3.74	2.49	3.22	2.61	0.41	0.60	2.31	2.10	1.34
S mean	obs	32.87	31.67	32.36	33.21	32.78	32.70	32.46	31.61	32.42	33.12	26.71	32.52	32.37	27.94	26.76	25.82
	mod	31.92	32.25	32.30	31.77	32.00	32.02	31.98	31.48	31.95	32.42	31.59	31.70	31.66	29.48	29.79	29.26
S min	obs	32.25	30.05	31.36	32.01	30.17	32.19	31.55	30.05	31.72	30.91	25.37	32.22	31.28	17.97	14.48	13.93
	mod	31.64	32.01	31.98	31.53	31.86	31.90	31.85	31.04	31.34	30.97	31.47	30.90	30.76	23.95	23.95	23.89
S max	obs	33.32	33.11	33.10	33.75	33.46	33.35	33.09	32.43	32.89	33.59	29.33	32.87	32.79	31.76	31.56	29.73
	mod	32.42	32.55	32.57	31.93	32.31	32.46	32.44	31.71	32.92	34.00	31.70	32.02	31.92	32.14	32.55	31.75
S var	obs	0.03	0.51	0.15	0.17	0.06	0.06	0.08	0.16	0.08	0.26	0.99	0.02	0.05	12.13	16.92	18.66
	mod	0.04	0.02	0.05	0.01	0.01	0.03	0.04	0.03	0.15	0.72	0.00	0.06	0.05	2.38	2.48	2.41

3.3.3 Sea Ice

Ice thickness Sea ice thickness data are taken from the monthly mean gridded files of *Kwok et al.* (2009), obtained from <http://rkwok.jpl.nasa.gov/icesat/download.html>. We compare the mean ice thickness fields from the model and observations and their differences. The left-hand panels of Figure 16 shows predicted ice thickness. The right-hand panels show the difference between the model and the observations (predicted–observed). These panels show that over most of the Chukchi and Beaufort seas, the modeled mid-winter ice thickness is typically within ± 1 m of that observed, with the notable exception of predicted ice that is too thin in the northeast Chukchi Sea and ice that is too thick along the Siberian coast. This suggests that the ice is too mobile, creating coastal polynyas too readily in the northeast Chukchi Sea and subsequently piling up too much ice along the Siberian coast. This problem in the ice also leads to excessive modeled ocean water freezing and elevated salinities in the NE Chukchi Sea region. Some of the modeled and observed salinity comparisons in Table 6 above suggest that this does in fact occur.

Ice concentration Figures 17–19 show comparisons of the modeled and observed sea ice concentrations in the Chukchi and Beaufort Seas. Blue contours in all of these figures denote the observed monthly ice concentration climatology with contours plotted at each integer multiple of 10% ice concentration. Color shadings in Figure 17 depict the difference between the modeled and observed concentrations, with colors that change at integer multiples of 10% ice concentration. The maps show that the model hindcasts ice concentrations within 10% of those observed for December through April, although in spring the model has too little ice near Point Barrow and in summer and fall months the model retains too much ice. The monthly mean magnitude of the model error is shown in Figure 18, which indicates that generally the model error is on the order of 20–40% during summer and fall months but can be as large as 50%. The comparison of standard deviations (Figure 19) shows that the model is more variable in the spring and summer months than what is observed over the Chukchi shelf and over the continental slope but the model is slightly less variable than observed in the northern Beaufort Sea. Differences in standard deviation (STD) are typically less than 20%.

Figure 20 shows the magnitude and sign of the cross-correlation of the modeled and observed ice concentrations in the Chukchi and Beaufort Seas. Yellow contours bound the regions for which the prediction is significant at the 95% confidence level (Spearman’s r , $p < 0.05$). These maps show that the model does not reproduce small amplitude variations in sea ice concentration in non-coastal areas during periods of near complete ice cover. Along the coasts and even offshore of the landfast ice, the model is able to reproduce low ice concentrations associated with wind-driven polynyas.

Averaging over the entire Chukchi-Beaufort Seas, we compute the mean climatology, monthly anomalies and annual anomalies (Figure 21). Results are consistent with the monthly maps discussed above. We see that the model begins to melt ice a little early in May with respect to these observations but achieves insufficient melt (possibly due to too

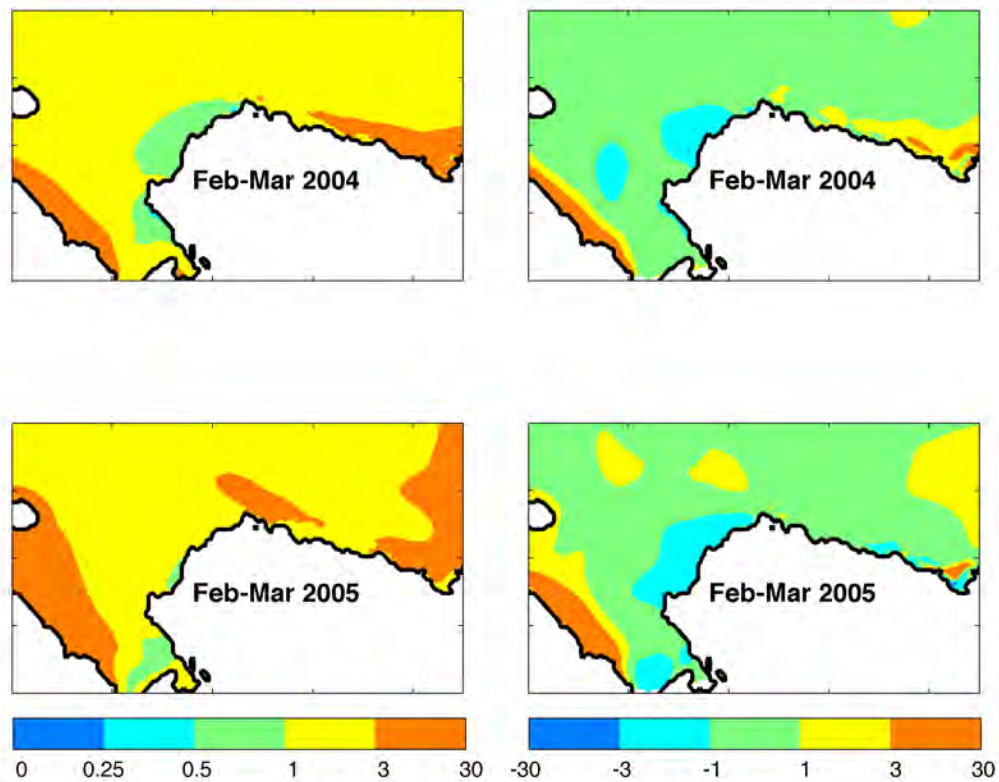


Figure 16: Predicted ice thickness (left panels) and the difference between the predicted thickness and that observed by the IceSat satellite (right panels). Thicknesses and differences are given in meters. Difference is plotted as model thickness minus observed thickness.

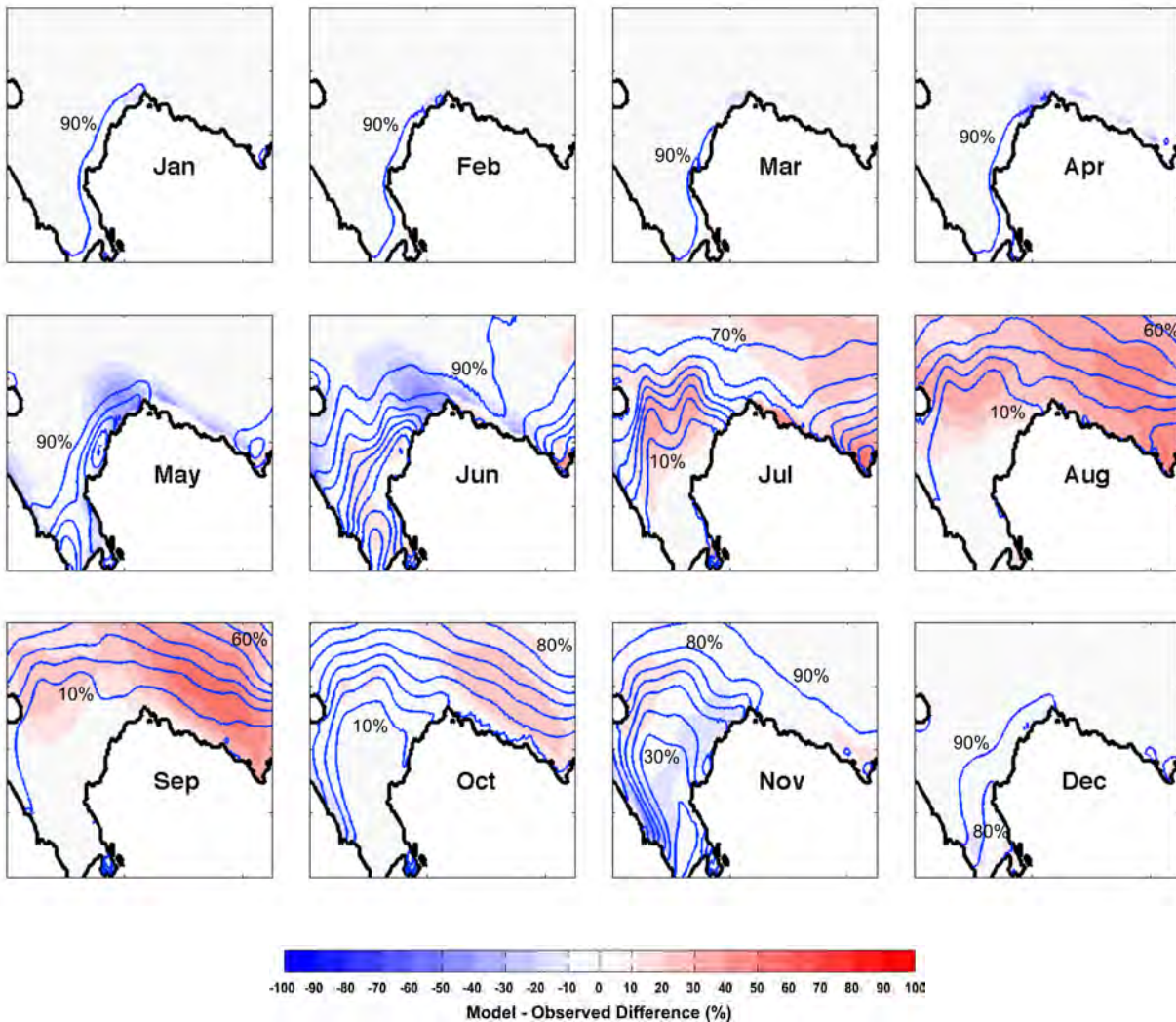


Figure 17: Monthly observed ice concentration and model-observed difference for the 1985–2005 Run05 hindcast. Blue contours denote the observed monthly climatology of ice concentrations with contours plotted at each integer multiple of 10% ice concentration. Colorbar denotes differences in units of percent concentration.

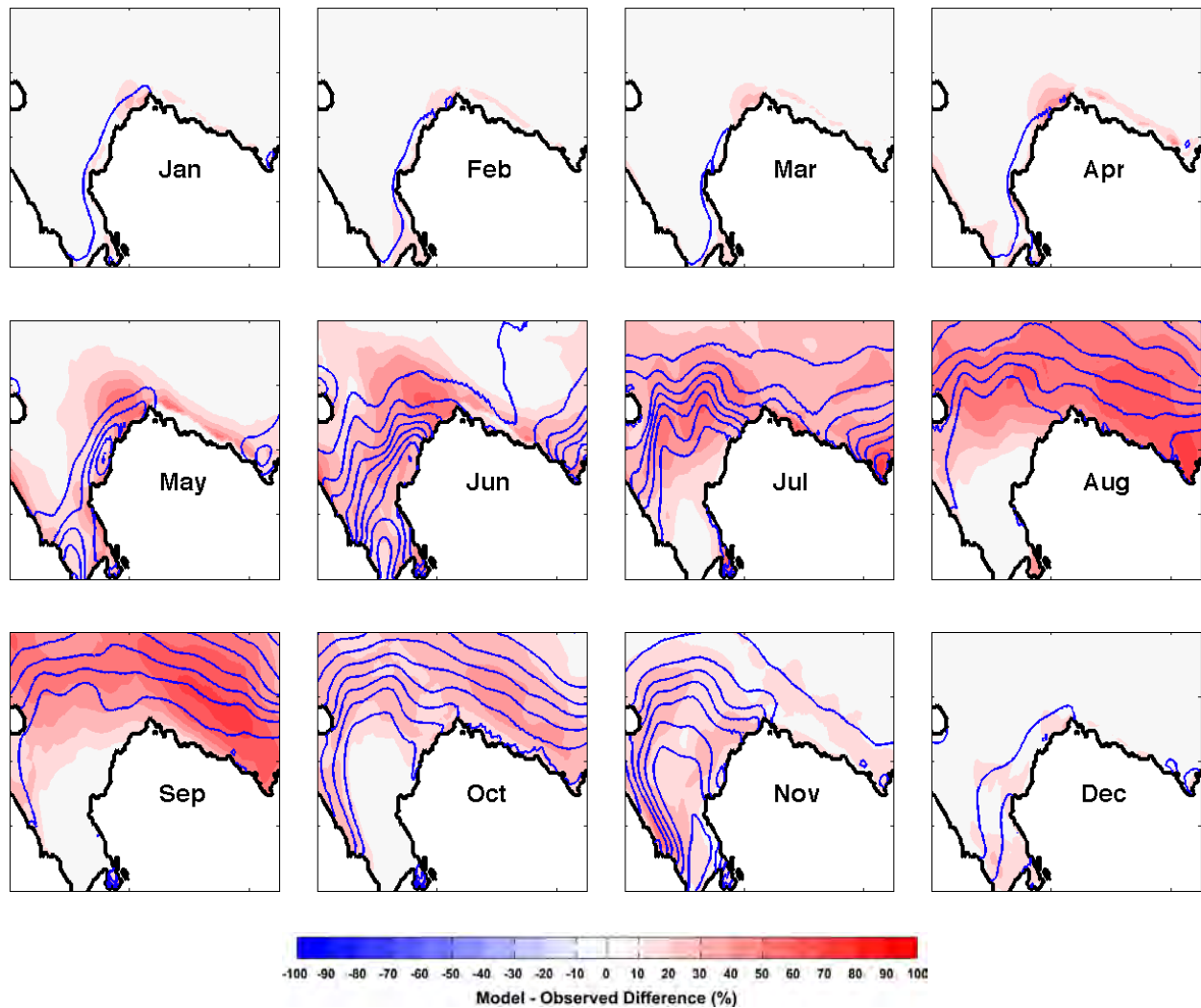


Figure 18: Mean observed ice concentration and model-observed RMSE for the 1985–2005 Run05 hindcast. Blue contours denote the observed monthly climatology of ice concentrations with contours plotted at each integer multiple of 10% ice concentration. Colorbar denotes differences in units of percent concentration.

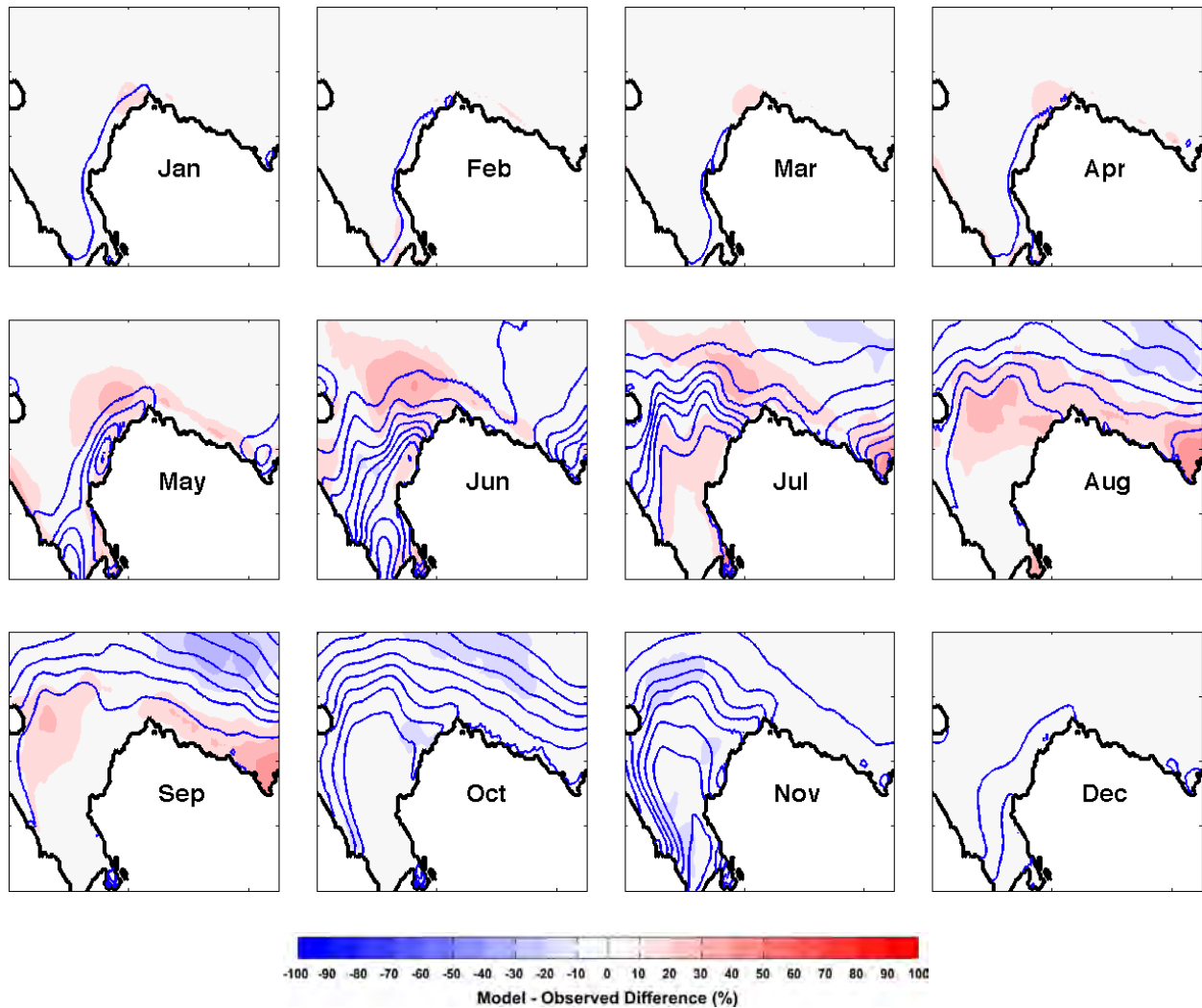


Figure 19: Mean observed ice concentration and model-observed STD difference for the 1985–2005 Run05 hindcast. Blue contours denote the observed monthly climatology of ice concentrations with contours plotted at each integer multiple of 10% ice concentration. Colorbar denotes differences in units of percent concentration.

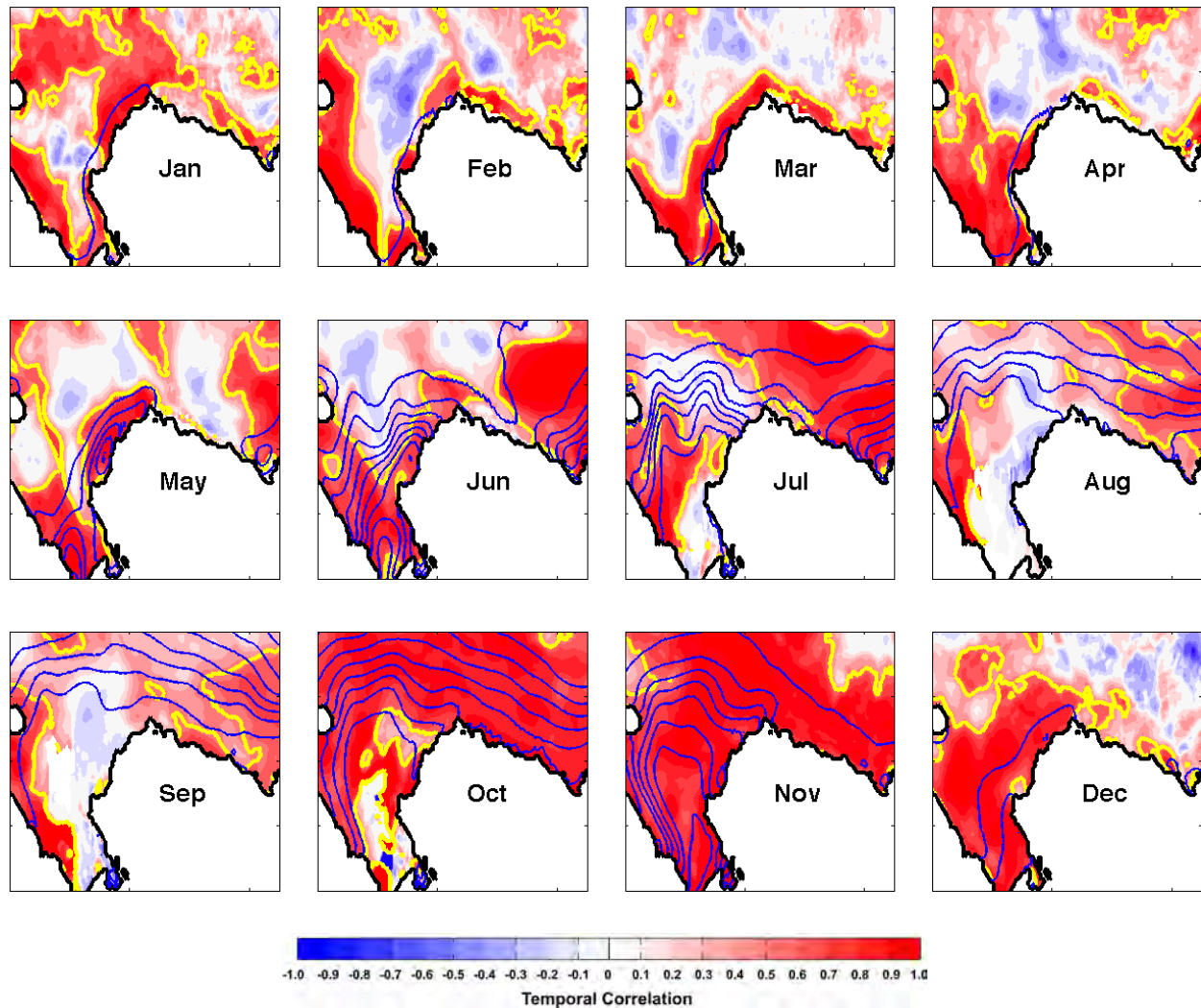


Figure 20: Mean observed ice concentration and model observed cross-correlation for the 1985–2005 Run05 hindcast. Blue contours denote the observed monthly climatology of ice concentrations with contours plotted at each integer multiple of 10% ice concentration. Colorbar denotes correlation coefficient. Yellow contour denotes significance at the 95% confidence level.

much ice formation in the previous winter) during July, August, and September. It is important to note that the passive microwave observations are known to miss some ice covered by wet snow and melt ponds, so the mismatch in Figure 21 may be complicated somewhat by observational error.

We find that the hindcast monthly ice concentration anomaly accounts for almost 50% of the observed anomaly and the annually averaged anomaly accounts for slightly more than 50% of that observed. Thus, the model provides appreciable insight beyond that of an annual climatology. The time series of monthly anomalies is shown in the middle panel of Figure 21, which shows that in most years, the modeled anomaly matches that of the observed anomaly quite closely. A few years stand out as being particularly problematic for the model, including the summer melt of seasons 1988, 2002, and 2003. We are currently unable to account for the atmospheric or oceanographic conditions responsible for these years of model underperformance. Examination of sea level pressure patterns for these years reveals no particular anomalies, which leads us to conclude that these events may be tied to the heat delivered to the Chukchi Sea through Bering Strait that was not captured by the southern boundary conditions.

Based on a 20% ice concentration threshold, example comparisons of the modeled date of ice onset with the observed ice onset are shown in Figure 22. The results are sensitive to the chosen location, likely a function of the transport pathways that deliver heat to the northern Chukchi Sea. Figure 22 shows that at 166° W, 71° N, the model is not able to well predict early freeze-up ($r = 0.74$), however two degrees of longitude west, it does a much better job ($r = 0.92$). This is consistent with the correlation map for October that shows a minimum in model performance in the northeast Chukchi Sea but a significant fit farther west. For the farther west site, the model is able to predict the date of ice formation to within ± 20 days for all years and to within ± 10 days for all but 1988, 2002, and 2003.

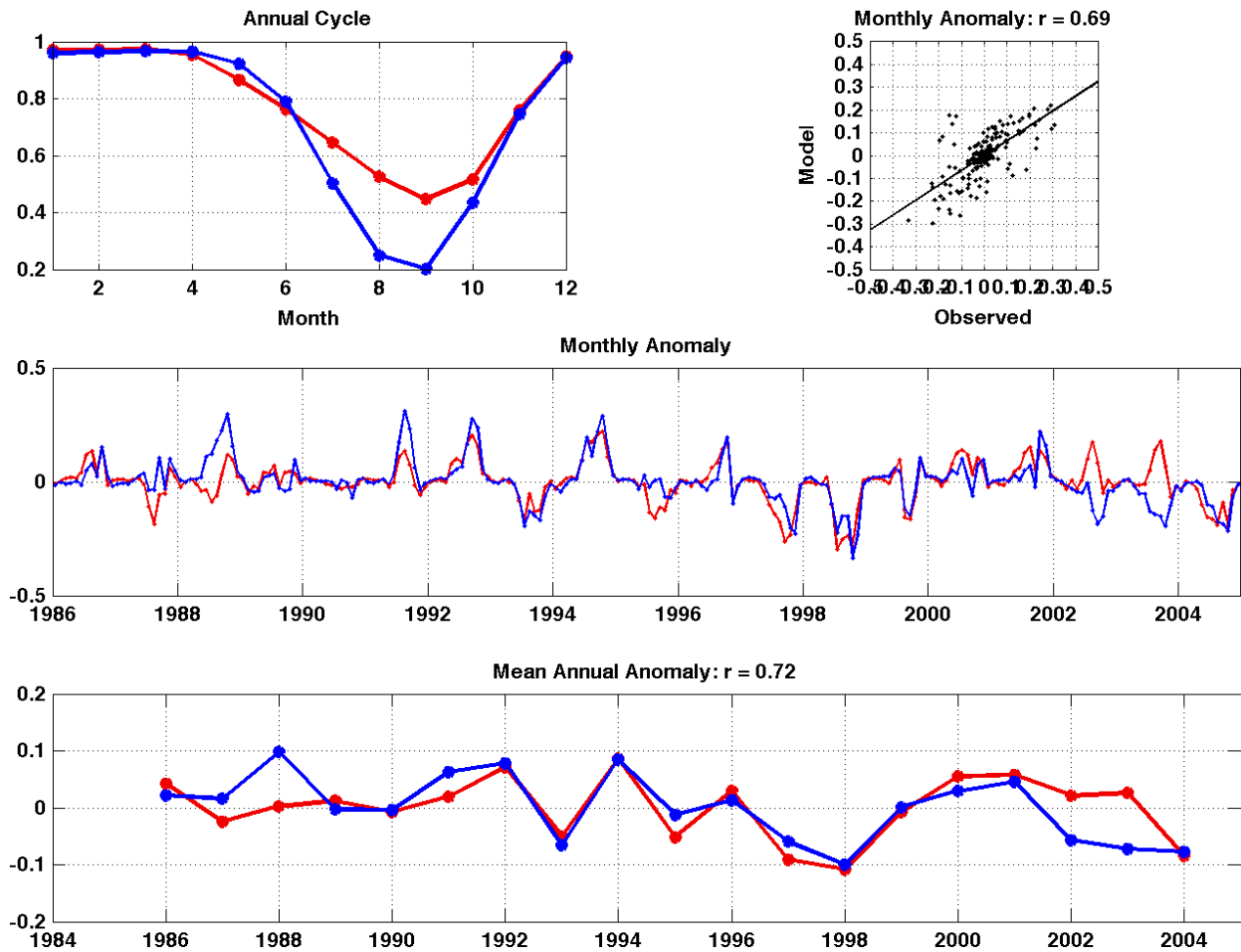


Figure 21: Area weighted sea ice concentration time series. Observed data are plotted in red and model output is plotted with blue.

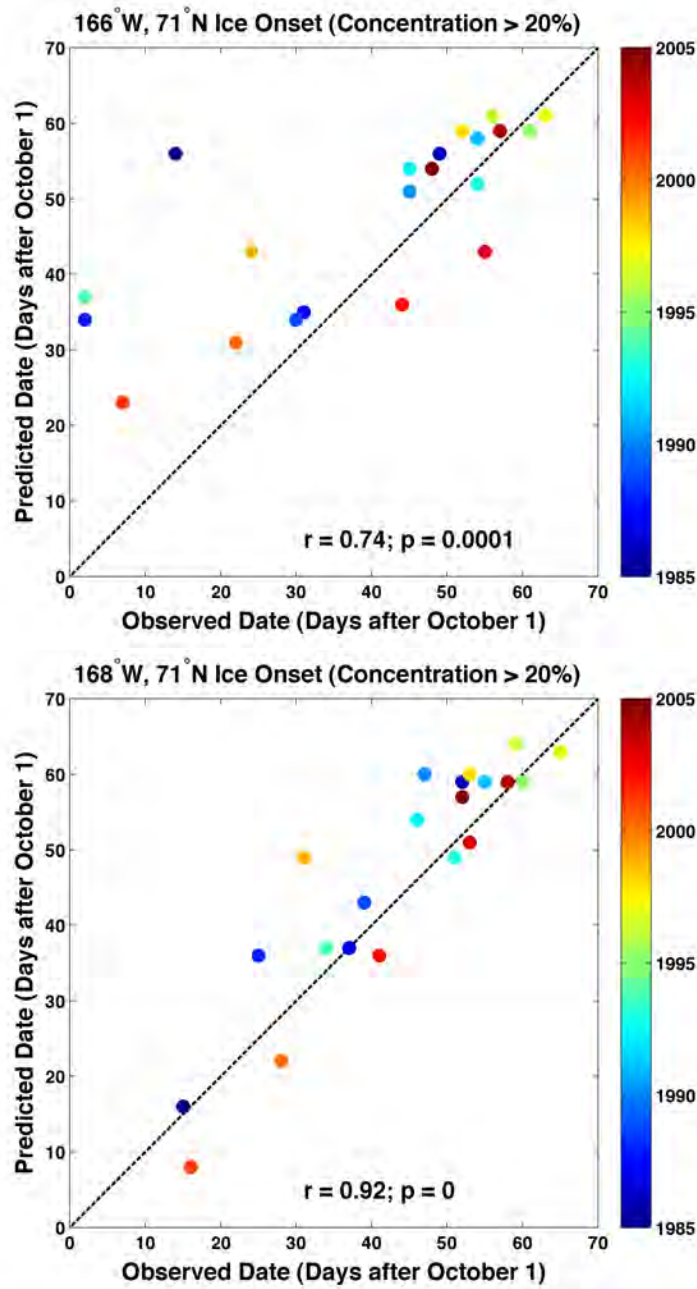


Figure 22: Sea ice onset at 71°N for 166°W (top) and 168°W (bottom).

4 Summary remarks

We presented results from a regional coupled circulation-sea ice model of the Chukchi and Beaufort seas, which was run in hindcast mode for the 1985–2005 period. We followed a design-run-evaluate-analyze-design spiral to achieve results that conform as closely as possible to the observations without strong restoring, which blurs the line between physical dynamics and model constraints.

We spent a considerable effort in attempting to implement a high resolution grid of the western Arctic only, however the complex boundary conditions associated with the sea ice field mandated that the model domain extend all the way to the North Atlantic so as to avoid a model edge through the middle of the ice pack. To maintain the requisite resolution in the Chukchi and Beaufort seas, a telescoping grid that covers the entire Arctic was developed. The grid cell size nearly matches that of the forcing in the North Atlantic (~ 25 km) and is ~ 3.5 -7 km in the western Arctic. Open boundary conditions (particularly to the south where Bering Strait feeds the Chukchi Sea) also exert strong control over the integration results within the Chukchi shelf temperature, salinity, and velocity fields. Some of the mis-match between the observed and modeled mean flows and flow variances (e.g., Figure 11) can be traced back to the limitations of the oceanic forcing imposed at Bering Strait.

We also spent a significant portion of time on model evaluations and comparison to in situ data. We used a combination of moored current meter and temperature/salinity time series, satellite-based sea ice thickness observations, and satellite-based sea ice concentration data. The observational data available for comparison are sparse in comparison to the two-decade model hindcast output fields so in the analyses we are forced to assume that the available records are accurate representations of the flow field and thermohaline fields in general.

Despite known deficiencies in the surface heat flux of available atmospheric forcing fields, the model was able to reproduce many aspects of the seasonal fluctuations that exist in the observations. We note particular success in the implementation of landfast ice in the Beaufort Sea, which led directly to a close reproduction of the observed annual cycle of currents on the inner Beaufort Sea shelf. Other strengths of the model include its ability to reproduce (to within the 95% confidence level) the observed U and V mean velocity components at nearly all mooring sites. In addition, the model was able to reproduce approximately 50% of the monthly mean sea ice concentration anomaly. Temperature/salinity fluctuations in Barrow Canyon were signatures of up-canyon and down-canyon flows and often matched the timing and magnitude of the observed variations.

Computations of transport across selected transects (Figure 23) provide insight to the circulation pathways over the Chukchi shelf, how the Bering Strait inflow is partitioned amongst the various branches of the northward flowing Bering Sea waters, and how these may change on a seasonally varying basis. We note that some aspects of these figures suggest seasonal variations that have not been previously appreciated for the Chukchi Sea circulation. These variations are not currently verifiable by observations due to lack of data (although current meter moorings scheduled for recovery in 2013 may provide some of the answers).

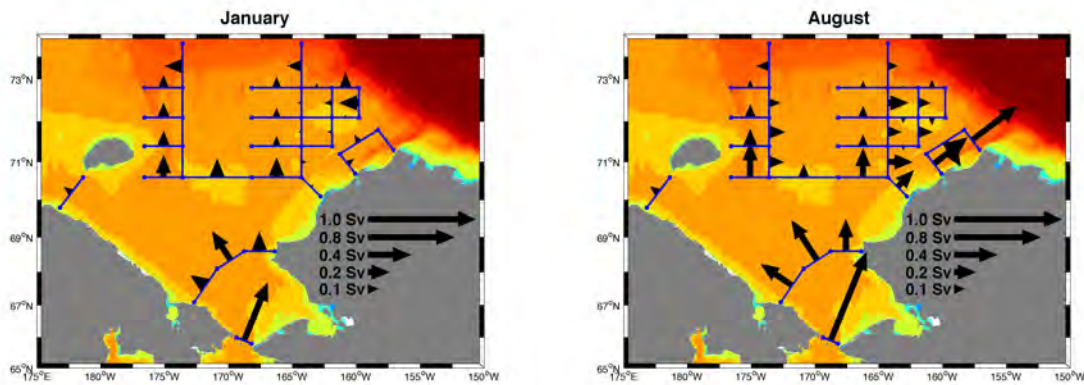


Figure 23: Transports averaged over the 1985–2005 Run05 hindcast for January (left) and August (right).

Examples of new insights suggested by these model integrations include 1) the direction and magnitude of the seasonally varying flow through Long Strait; 2) the magnitude of flow across Herald Shoal in winter; 3) the direction of the flow (and its possible seasonal reversal) to the north and northeast of Hanna Shoal. It is not clear whether the character of these features as resolved by the model well represents the actual ocean or if these features represent model deviations from the real world. In the context of the model-observation velocity comparisons made above, we have reason to believe the model results in these unmeasured regions of the Chukchi Sea bear some resemblance to the functioning of the real ocean.

A particular challenge to the model was the insufficient melting of ice in the summer months. In part, this appears to be due to ice that is too mobile, leading to coastal polynyas that kept the ocean exposed to the atmosphere for too long during the winter months. As a consequence, the shelf salinities grew too high and the ice swept away from the polynya region in the northeast Chukchi Sea was compacted along the Siberian coast in unrealistically thick ridges. In addition, the model did not closely reproduce the expected manifestation of the Alaska Coastal Current, although the summer increase in flow past Point Barrow and through Barrow Canyon was observed. Improvements of the southern boundary conditions in Bering Strait would likely capture a more realistic coastal current in future model runs, however it may also be necessary to lessen the quantity of winter dense water production over the shelf. Similarly, there is little evidence for the Siberian Coastal Current along the western Chukchi Sea shoreline. It is possible that a different implementation of the coastal discharge could capture this feature. Along the upper Beaufort slope, we do not observe a Beaufort Undercurrent shelfbreak jet. Three limiting factors may play a role in this: 1) model resolution in the slope region; 2) strength of the modeled Beaufort Gyre; and 3) thermohaline properties of the Barrow Canyon outflow.

Although this model is now at a fairly mature stage, future improvements are within reach. Improved boundary conditions in Bering Strait would lead to a better developed

Alaska Coastal Current and the buoyancy-driven jet associated with this low-salinity feature. Implementing point source river inputs from the large Arctic rivers and some small rivers along Alaska's coast could improve the model performance in regions that these river's out-flow plumes strongly impact. The ice field could see improvements by moving away from the ice module currently within ROMS and implementing a multi-category ice model such as the Los Alamos National Laboratory (LANL) CICE model (<http://climate.lanl.gov/Models/CICE/>). Development of an ice model that dynamically grows landfast ice would be novel and provide a significant step forward in arctic modeling and could possibly be achieved with a dedicated effort.

A Appendix: Monthly mean hindcast fields

On the following pages we display mean hindcasts of each calendar month's velocity, transport, sea surface elevation, temperature, and salinity in the form of maps and vertical cross-sections. These monthly climatologies are provided as a summary of the model integrations and as a reference for diagnosing model behavior and characteristics (both successes and limitations). In addition, these plots provide insight to the physical dynamics of the study region.

A.1 Sea surface height

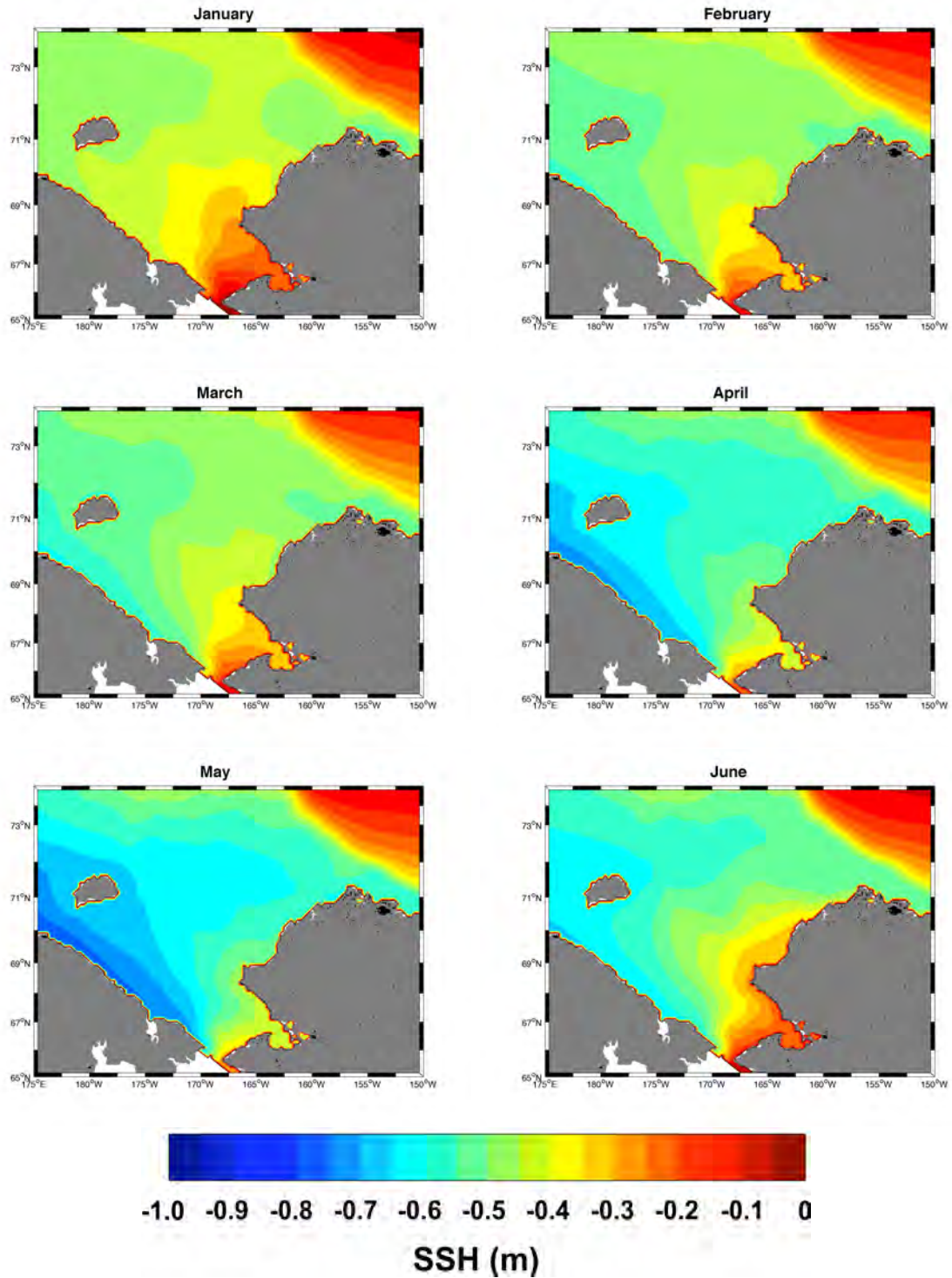


Figure 24: Hindcast monthly mean sea surface height (SSH) maps for the Chukchi Sea.

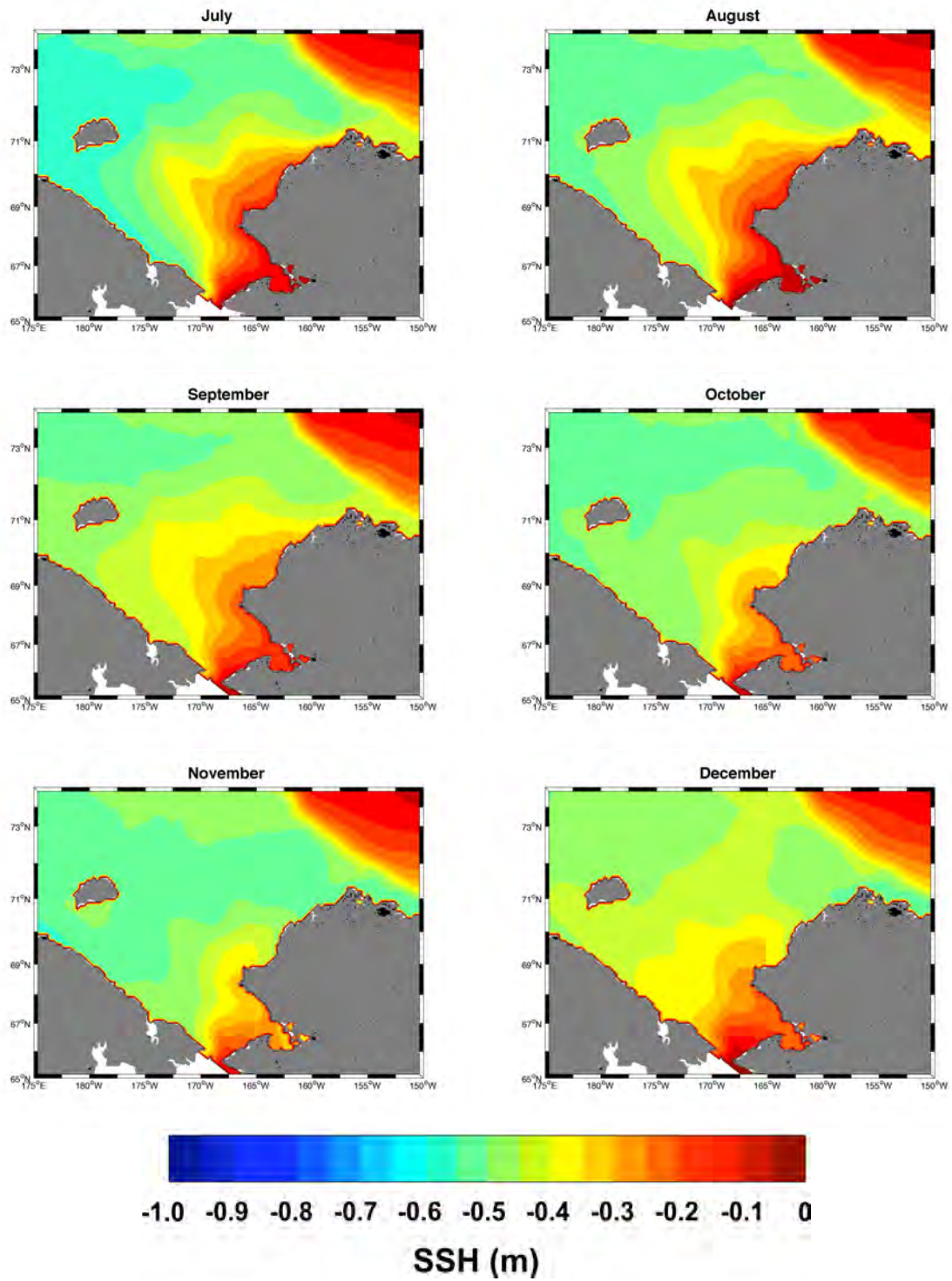


Figure 24: Hindcast monthly mean sea surface height (SSH) maps for the Chukchi Sea (Continued).

A.2 Velocities

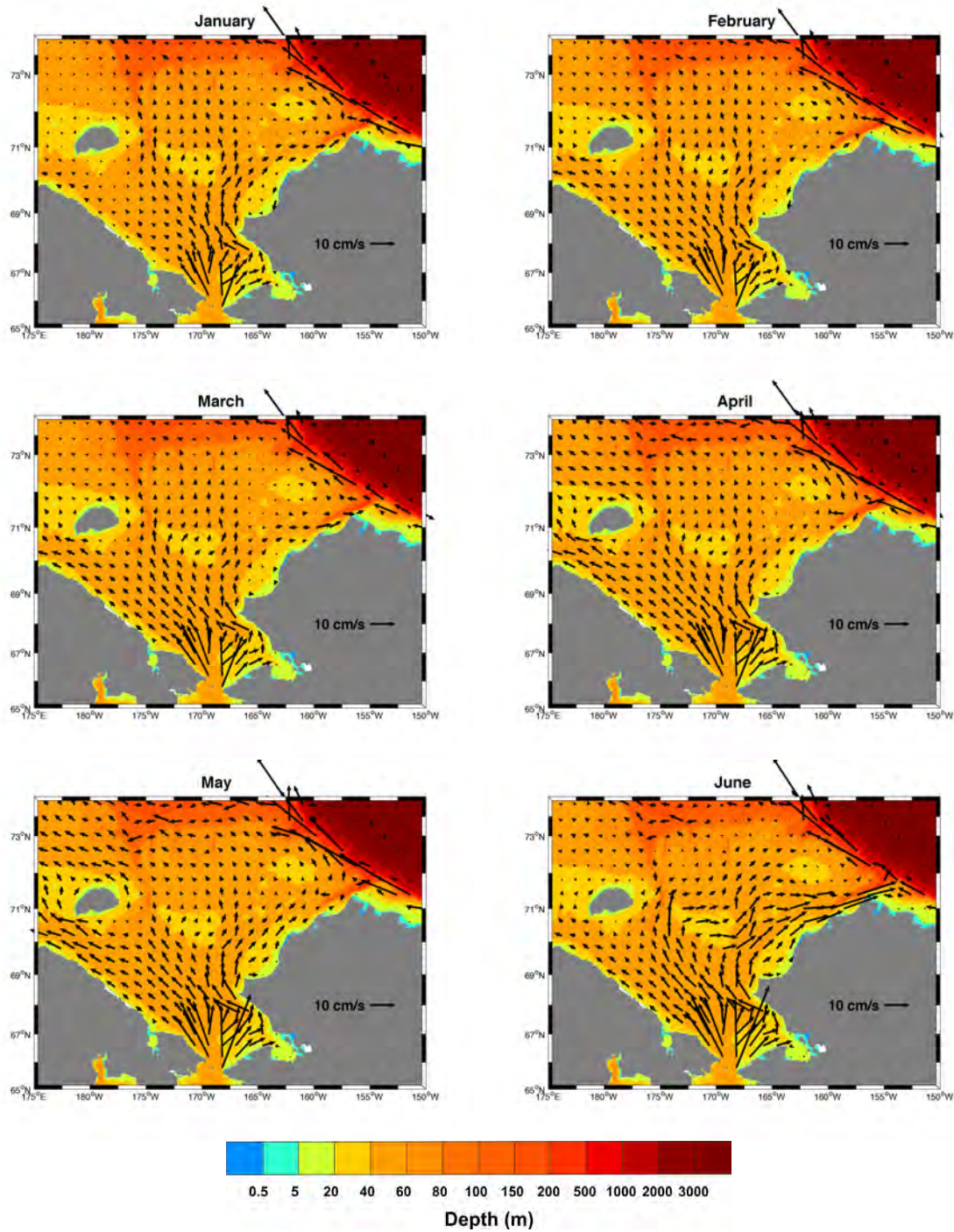


Figure 25: Hindcast monthly mean vertically averaged velocity vectors from the Chukchi Sea.

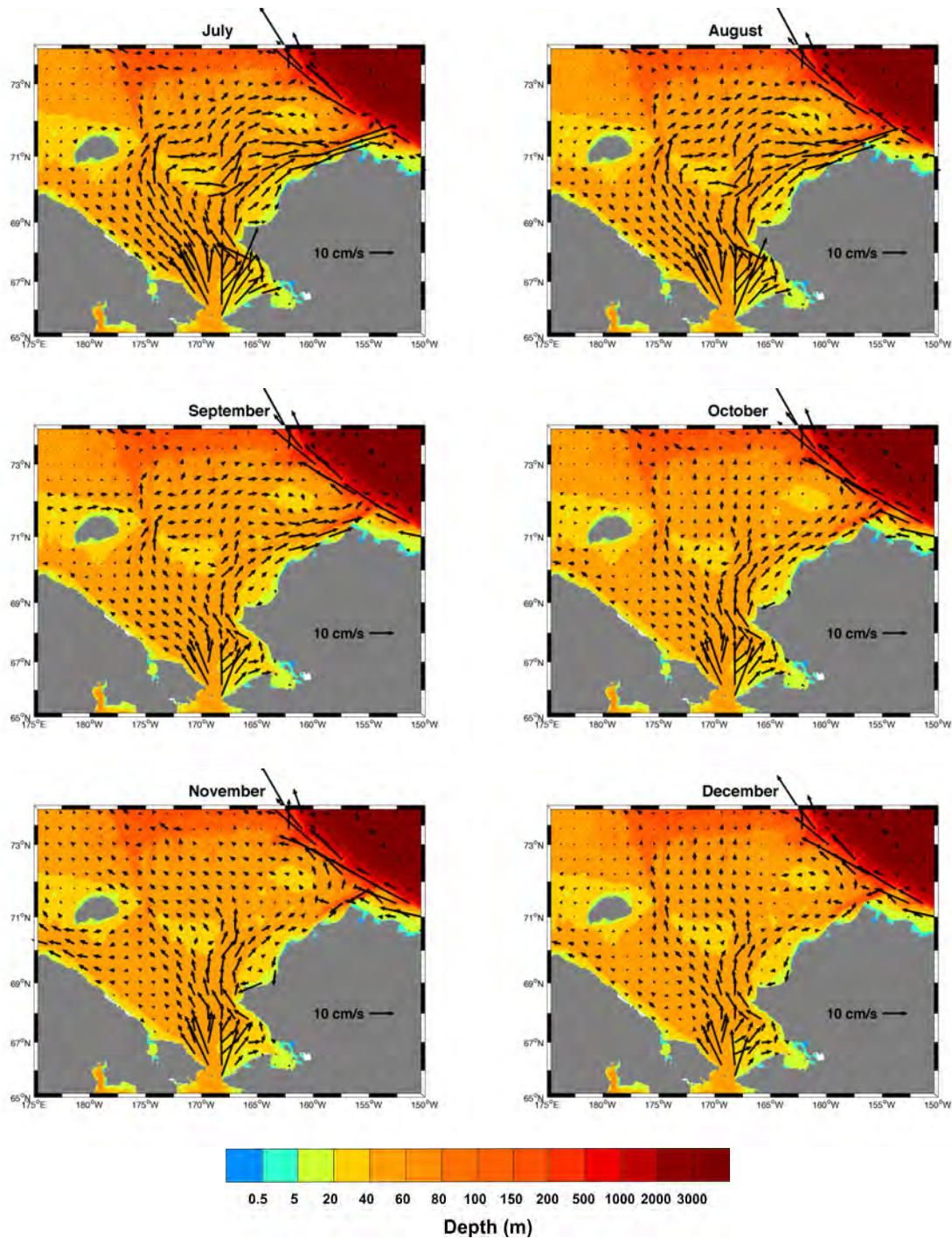


Figure 25: Hindcast monthly mean vertically averaged velocity vectors from the Chukchi Sea (Continued).

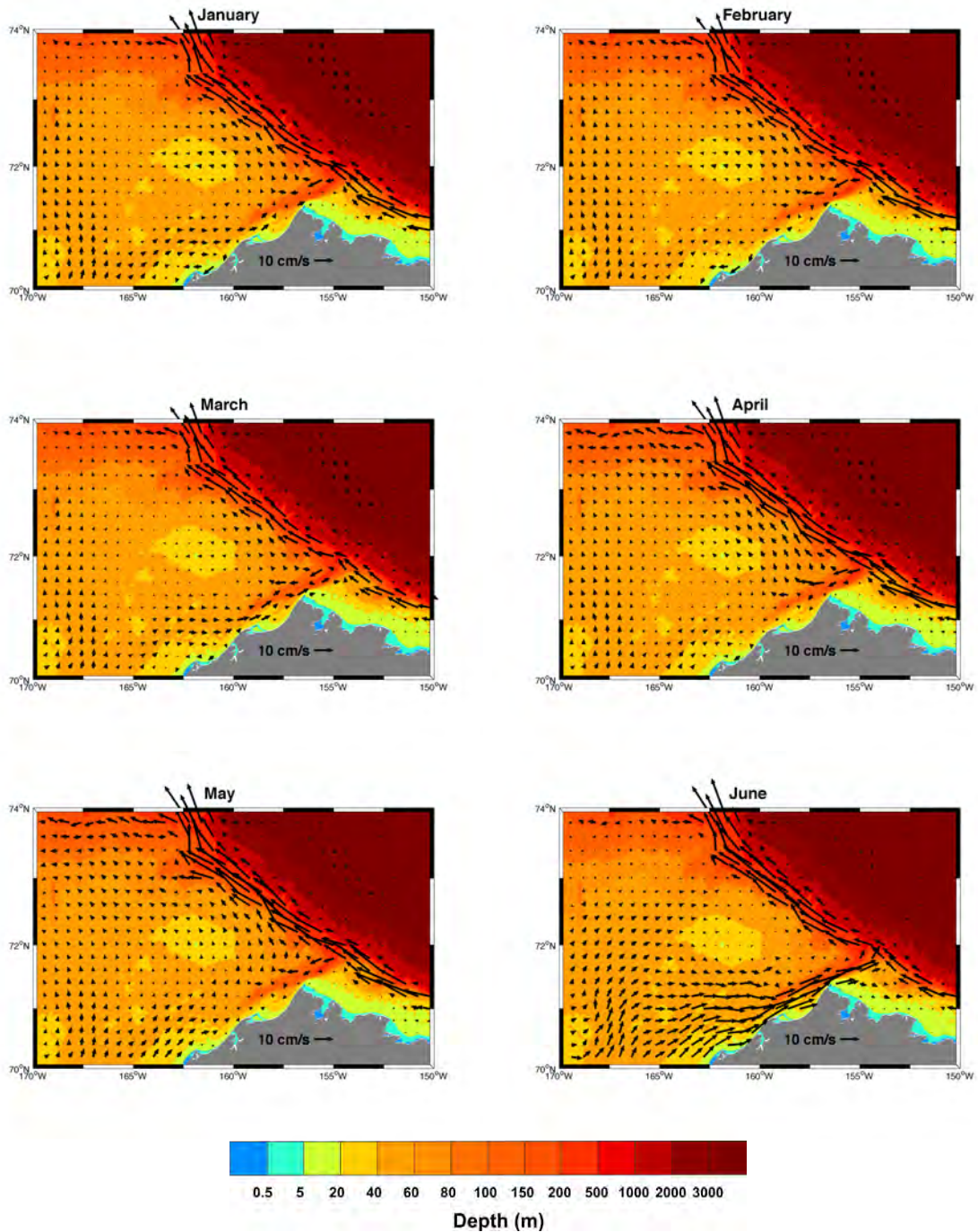


Figure 26: Hindcast monthly mean vertically averaged velocity vectors from the Northeast Chukchi Sea (a zoom of Figure 25 showing more of the vectors).

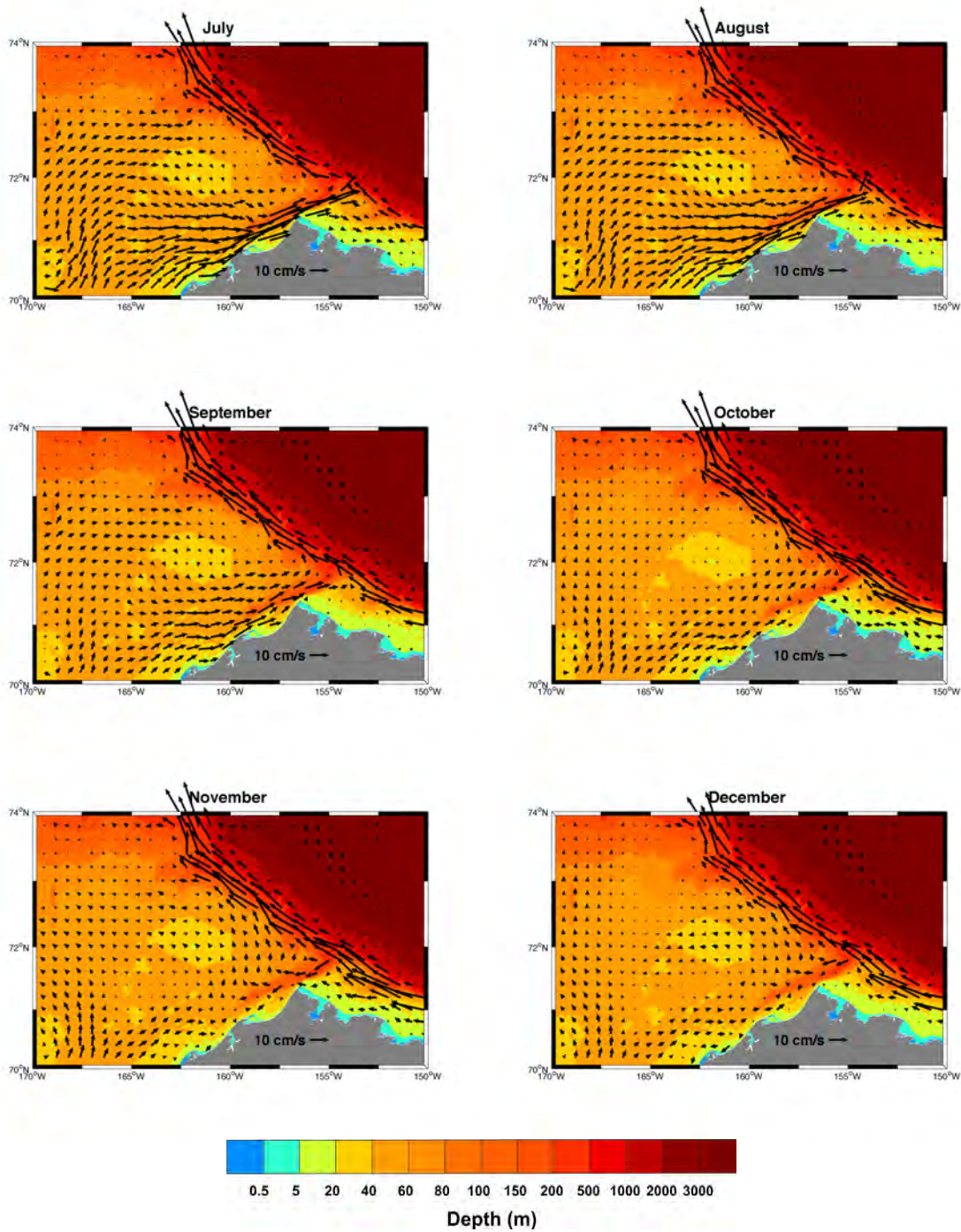


Figure 26: Hindcast monthly mean vertically averaged velocity vectors from the Northeast Chukchi Sea (a zoom of Figure 25 showing more of the vectors) (Continued).

A.3 Temperature at 5 m depth

A.3 Temperature at 5 m depth

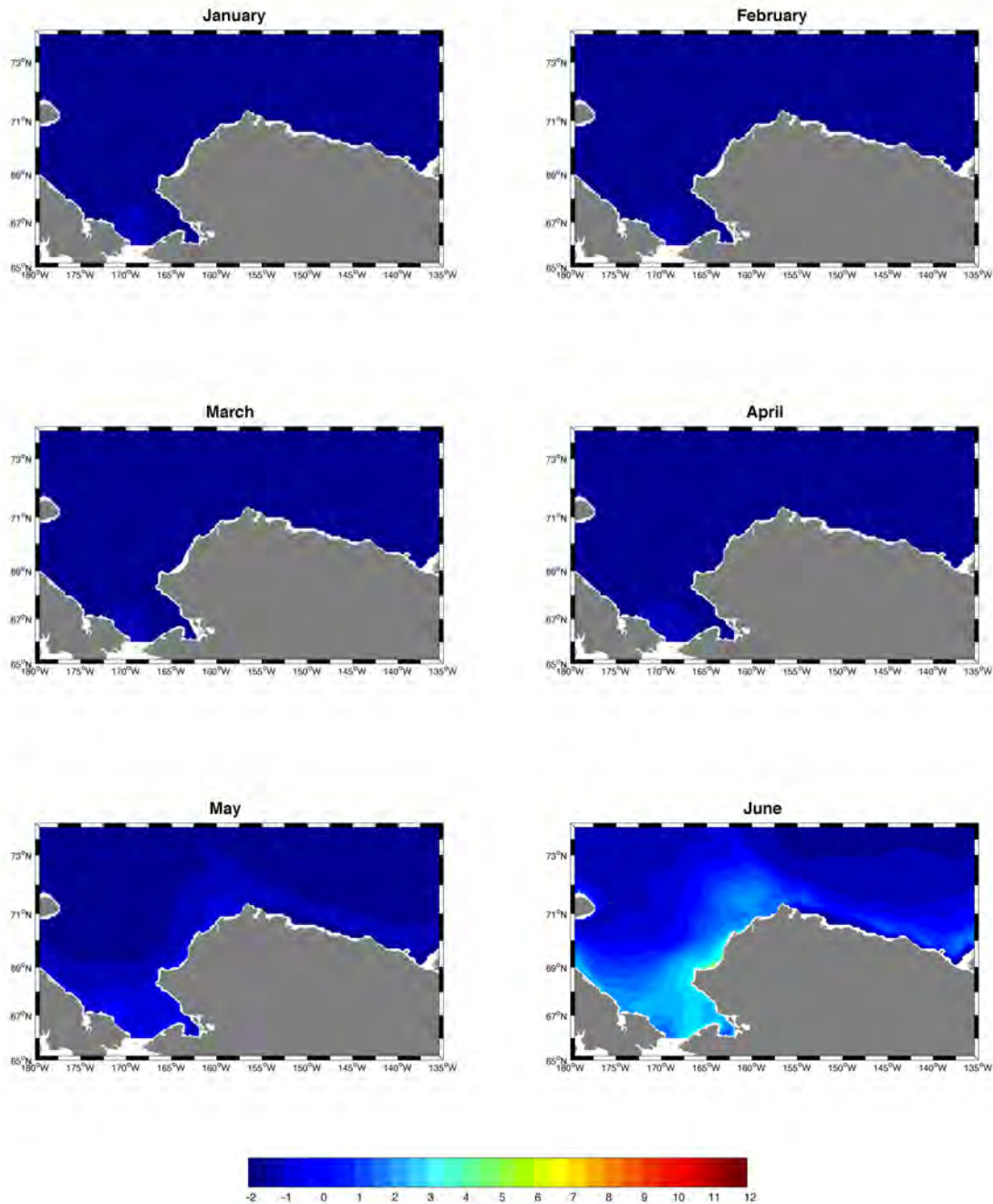


Figure 27: Hindcast monthly mean temperatures at 5 m depth in the Chukchi and Beaufort Seas. Color scale varies from -2 to $+12^{\circ}\text{C}$.

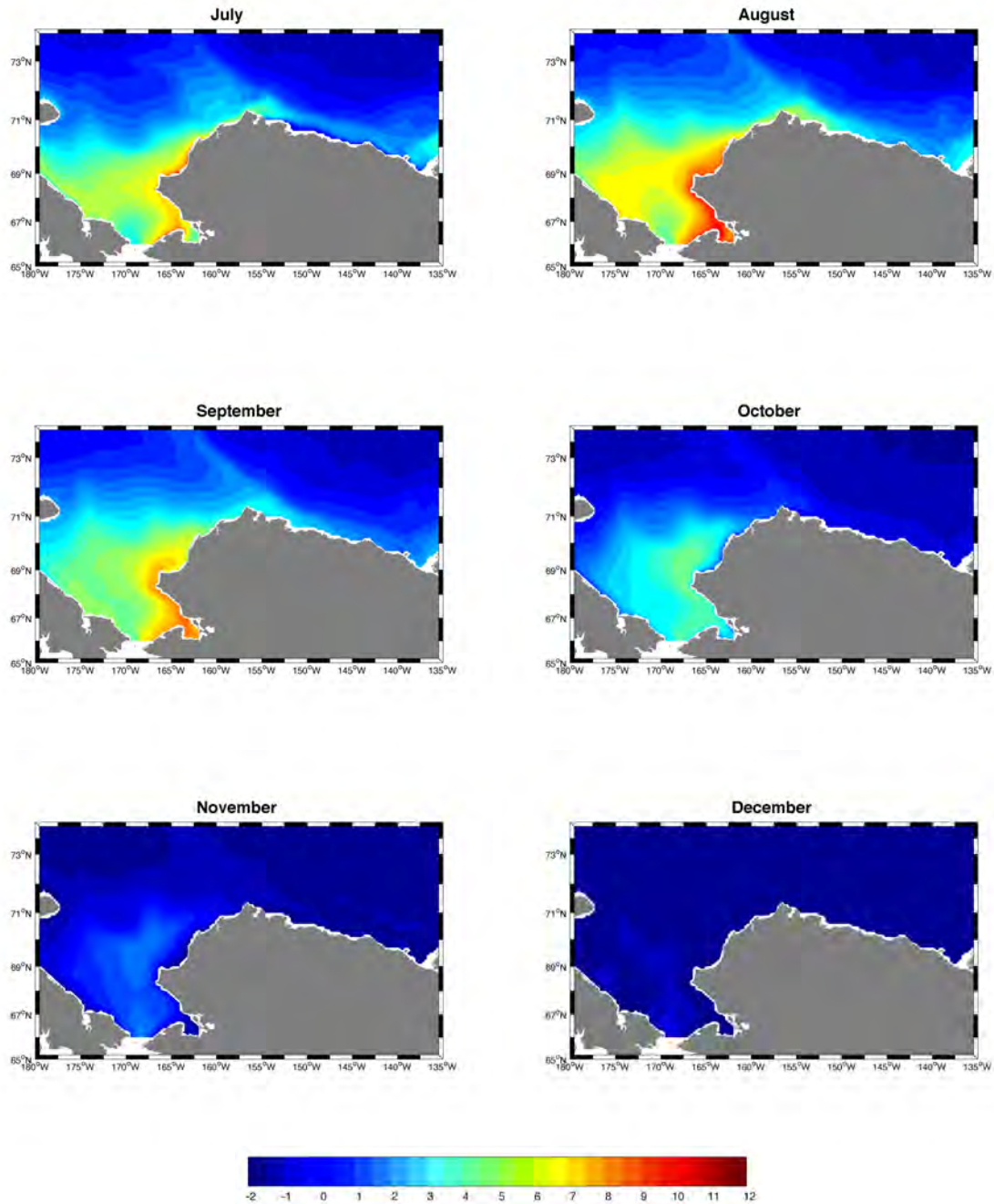


Figure 27: Hindcast monthly mean temperatures at 5 m depth in the Chukchi and Beaufort Seas. Color scale varies from -2 to $+12^{\circ}\text{C}$ (Continued).

A.4 Salinity at 5 m depth

A.4 Salinity at 5 m depth

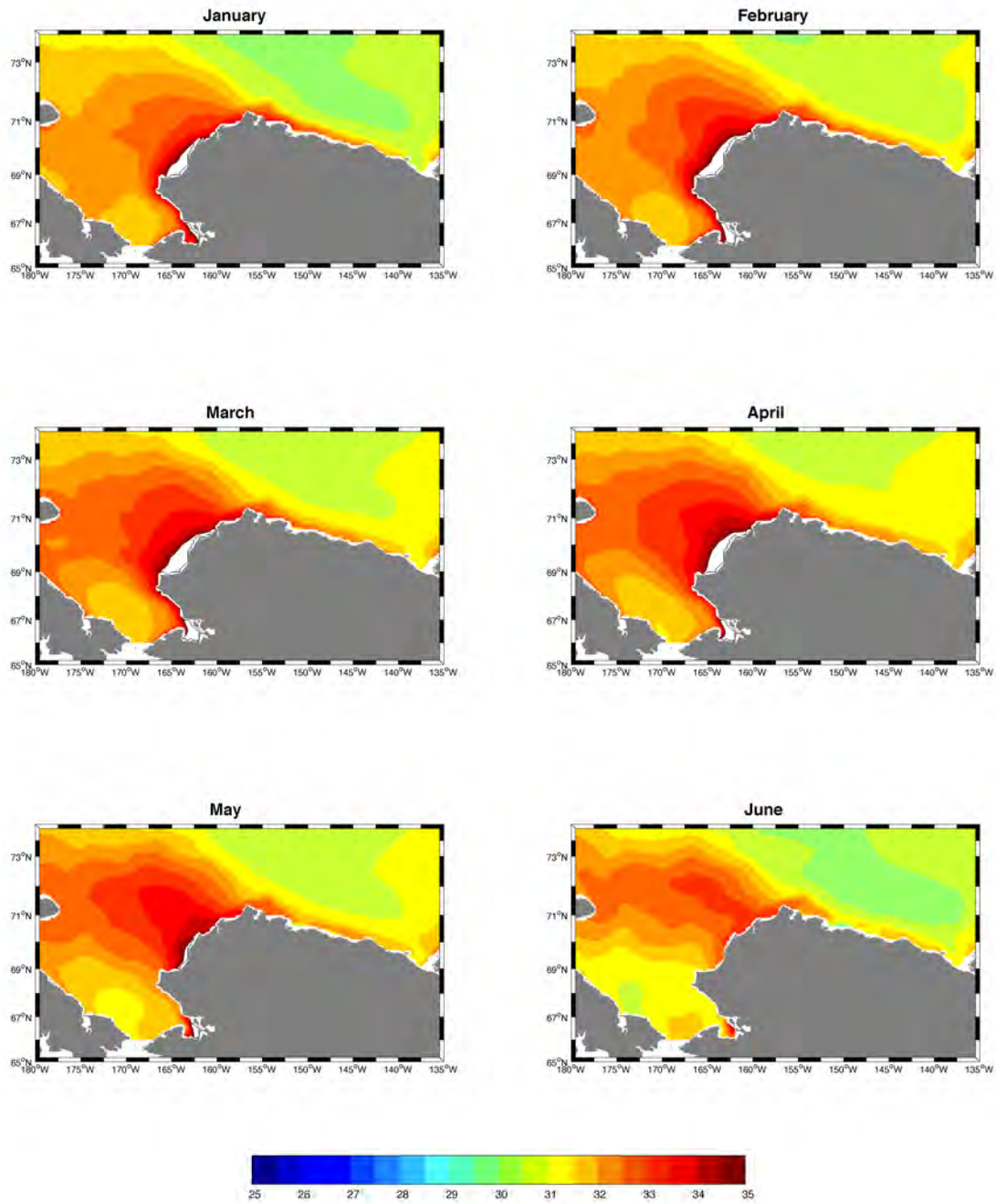


Figure 28: Hindcast monthly mean salinity at 5 m depth in the Chukchi and Beaufort Seas. Color scale varies from 25 to 35.

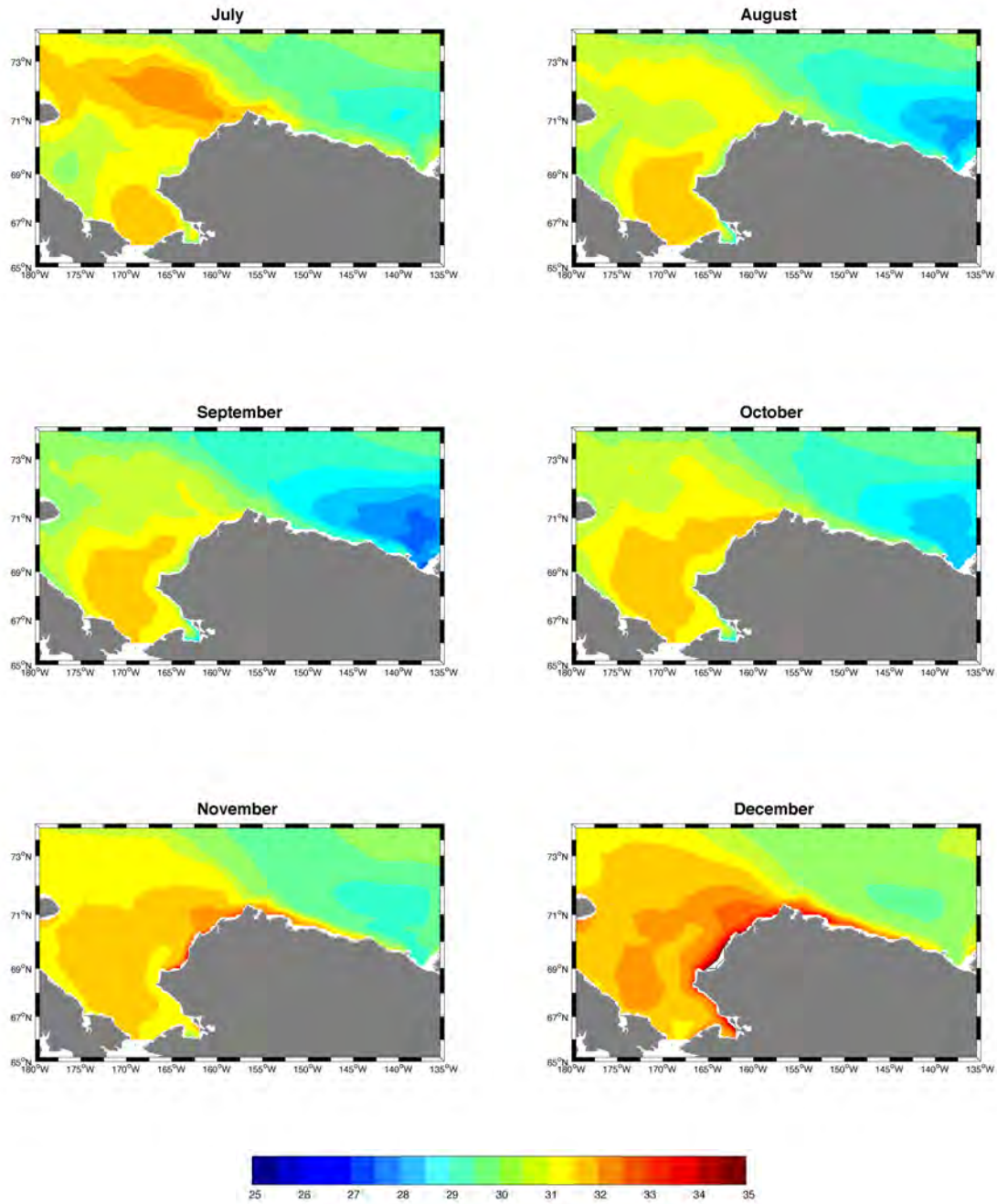


Figure 28: Hindcast monthly mean salinity at 5 m depth in the Chukchi and Beaufort Seas. Color scale varies from 25 to 35 (Continued).

A.5 Vertical cross-sections of velocity at 150°W

A.5 Vertical cross-sections of velocity at 150°W

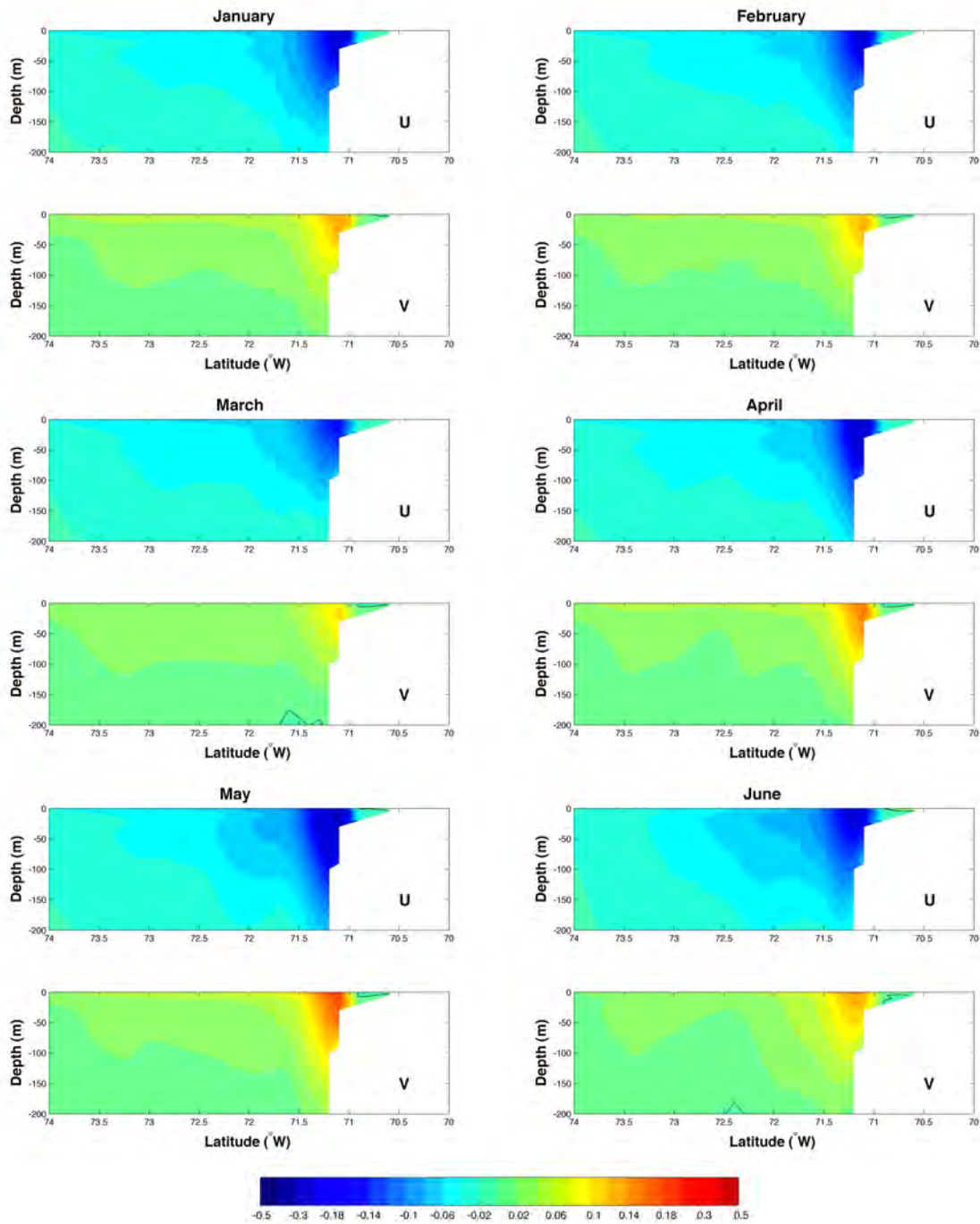


Figure 29: Hindcast monthly mean horizontal velocity components at 150°W in the Beaufort Sea. Color scale varies from -0.5 to $+0.5$ m/s.

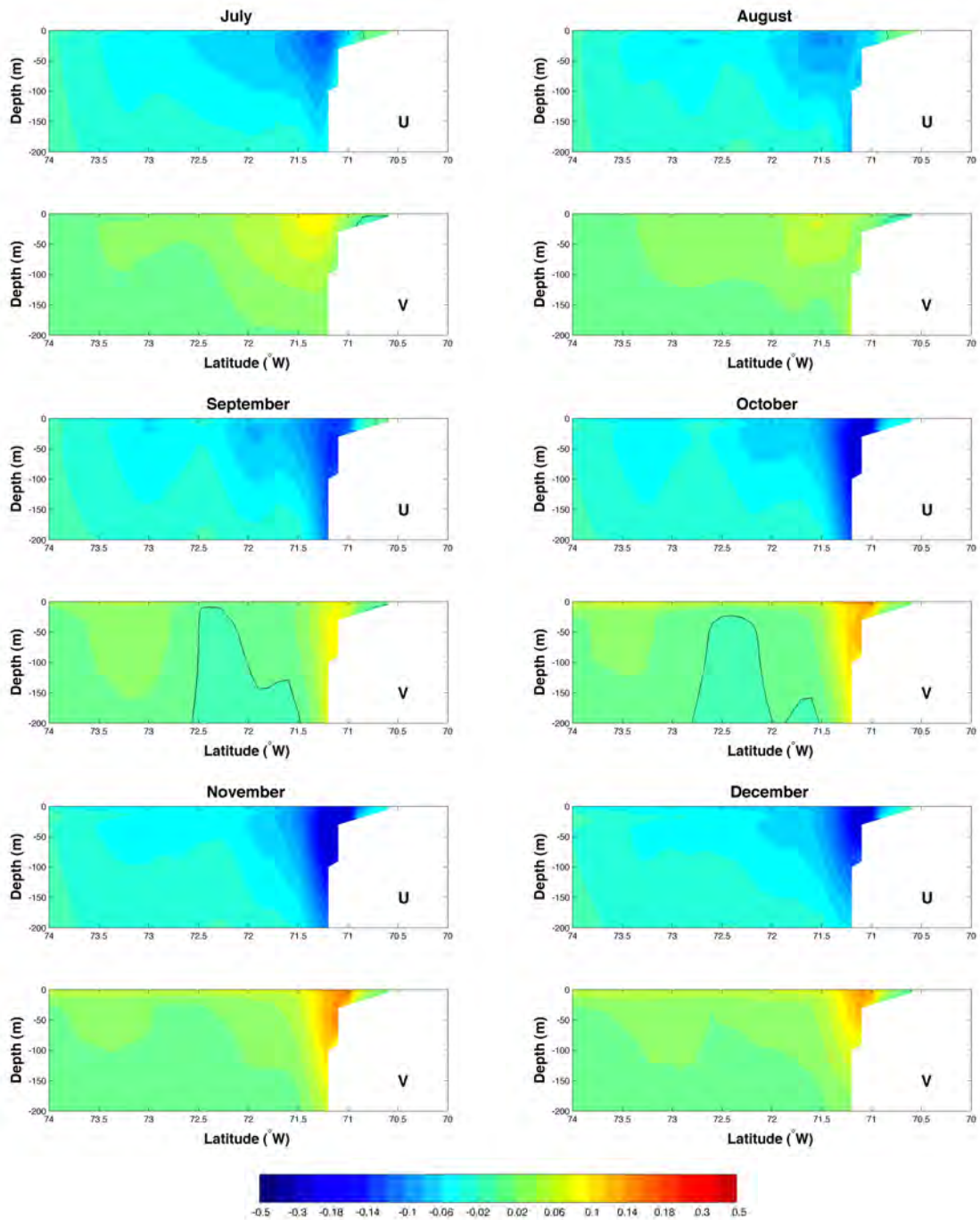


Figure 29: Hindcast monthly mean horizontal velocity components at 150°W in the Beaufort Sea. Color scale varies from -0.5 to $+0.5$ m/s (Continued).

A.6 Vertical cross-sections of temperature at 150°W

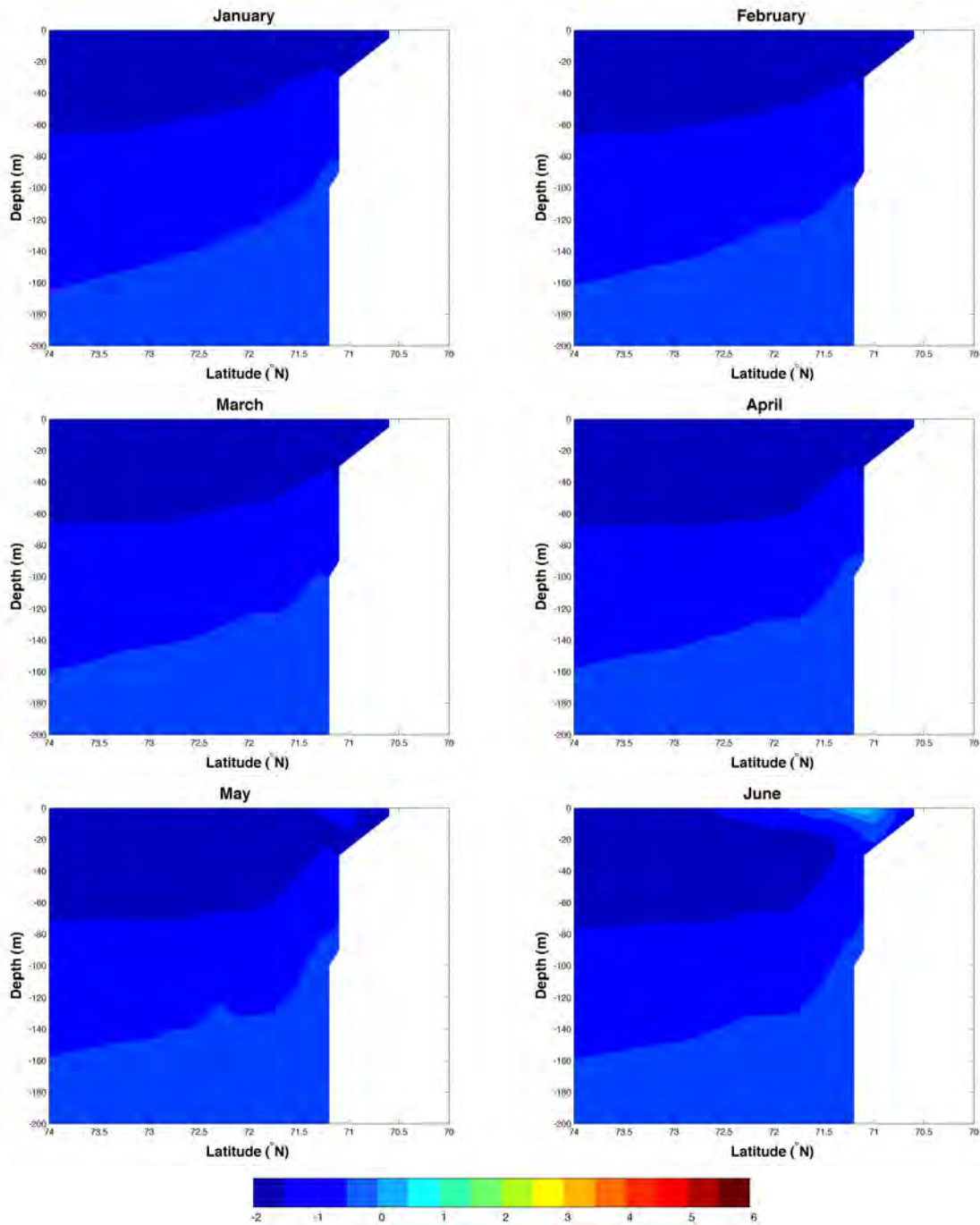


Figure 30: Hindcast monthly mean temperatures at 150°W in the Beaufort Sea. Color scale varies from -2 to +6°C.

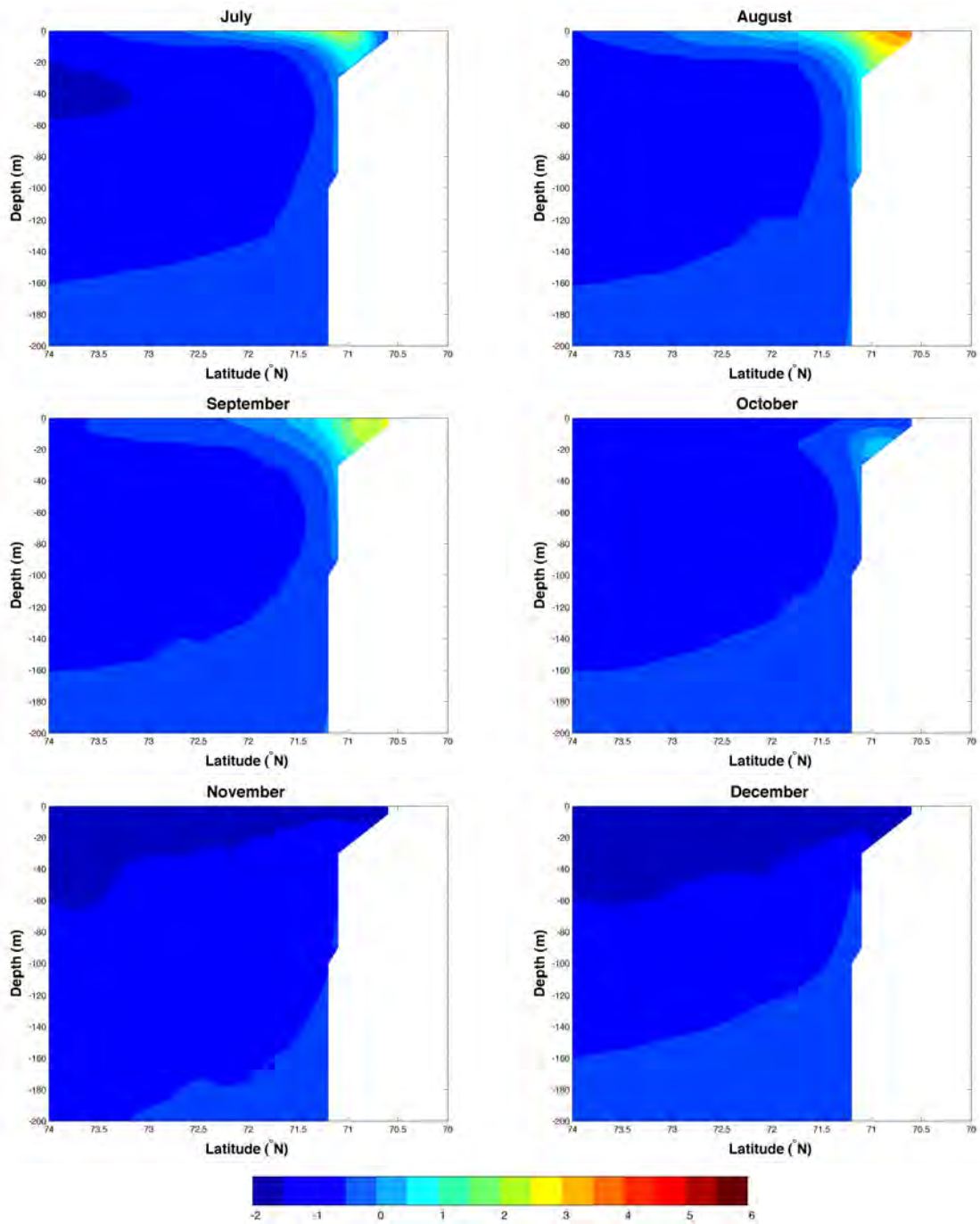


Figure 30: Hindcast monthly mean temperatures at 150°W in the Beaufort Sea. Color scale varies from -2 to $+6^{\circ}\text{C}$ (Continued).

A.7 Vertical cross-sections of salinity at 150°W

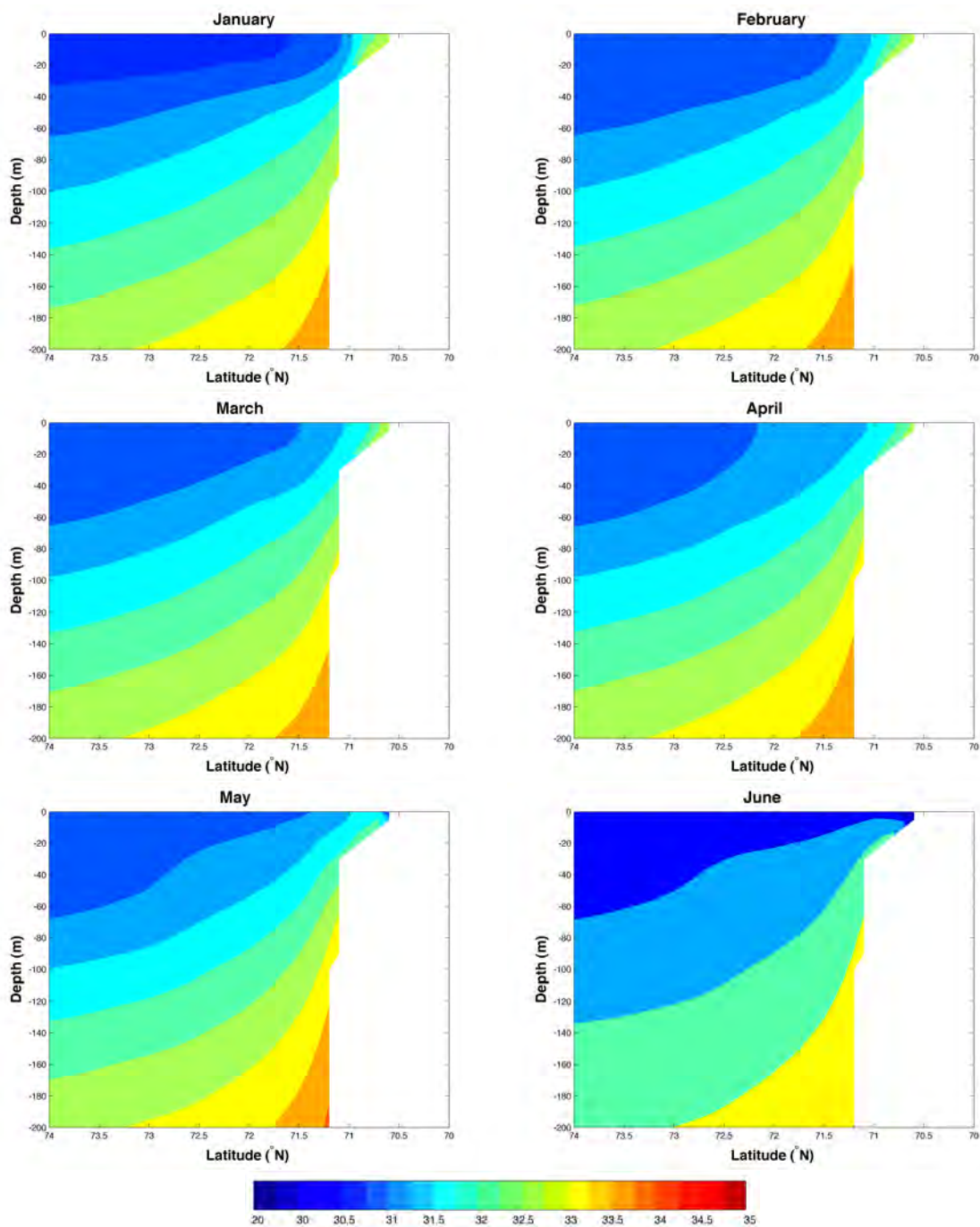
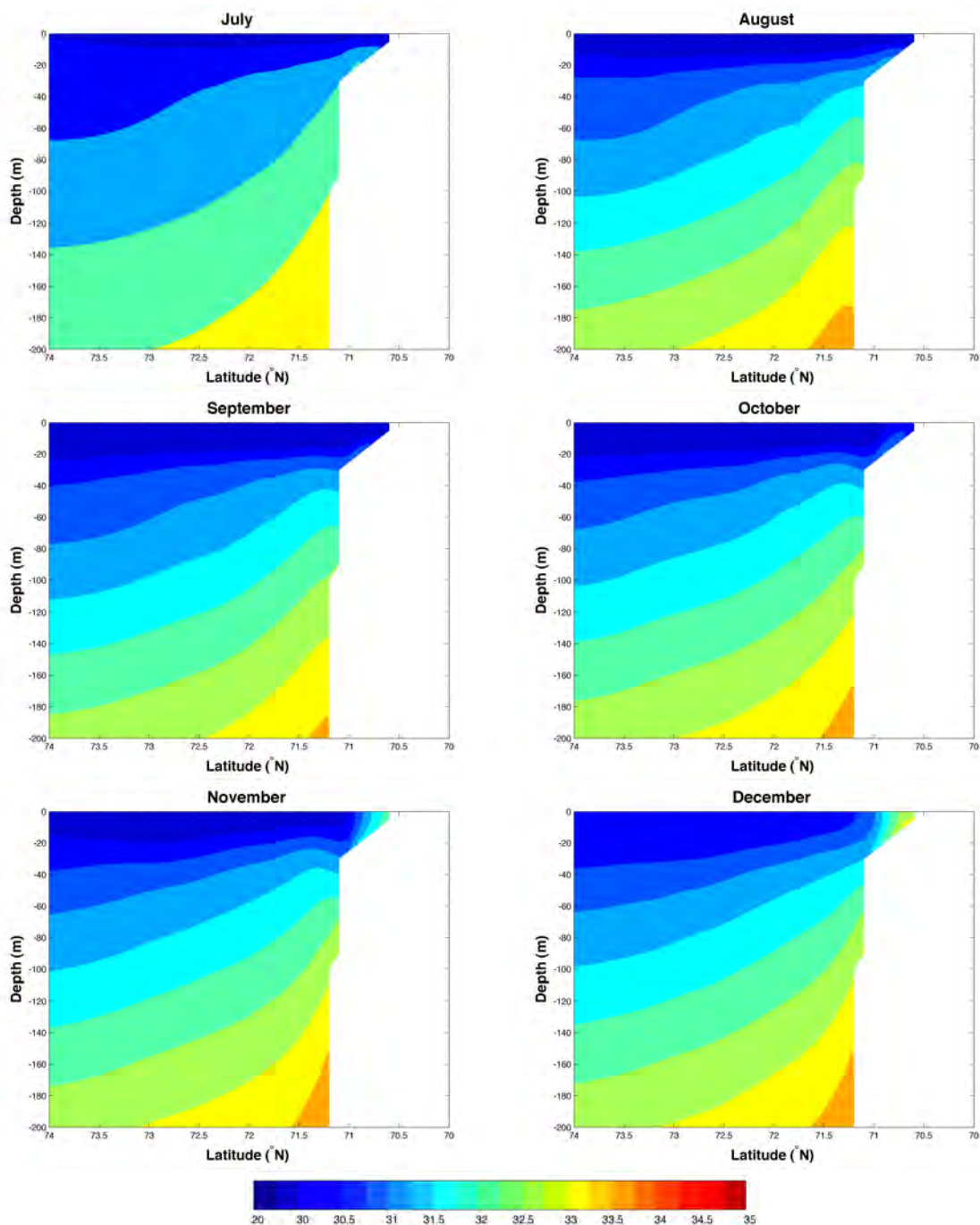


Figure 31: Hindcast monthly mean salinity at 150°W in the Beaufort Sea. Color scale varies from 20 to 35.



Hindcast monthly mean salinity at 150°W in the Beaufort Sea. Color scale varies from 20 to 35 (Continued).

A.8 Vertical cross-sections of velocity at 71°N

A.8 Vertical cross-sections of velocity at 71°N

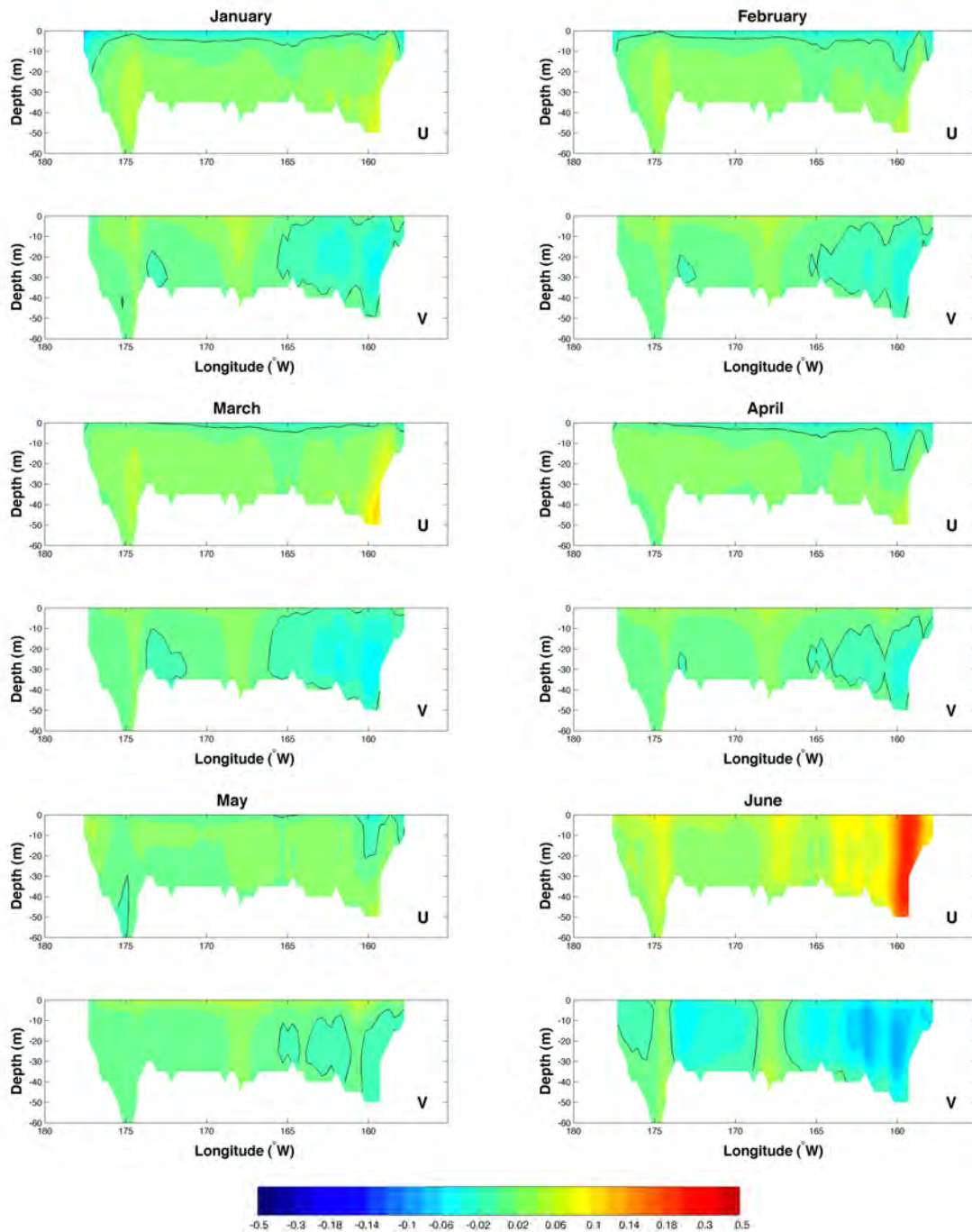


Figure 32: Hindcast monthly mean horizontal velocity components at 71°N in the Chukchi Sea. Color scale varies from -0.5 to $+0.5$ m/s.

A.8 Vertical cross-sections of velocity at 71°N

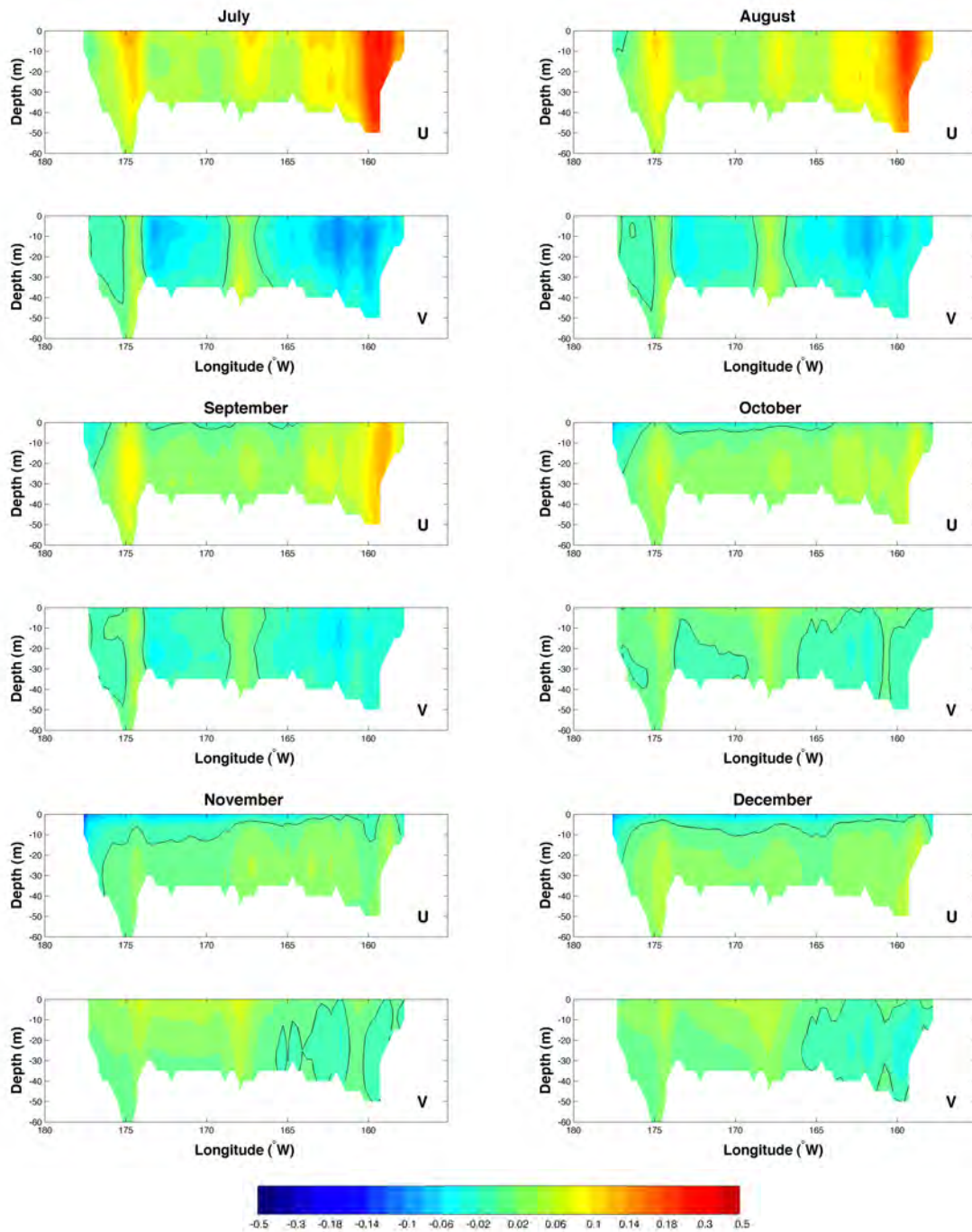


Figure 32: Hindcast monthly mean horizontal velocity components at 71°N in the Chukchi Sea. Color scale varies from -0.5 to +0.5 m/s (Continued).

A.9 Vertical cross-sections of temperature at 71°N

A.9 Vertical cross-sections of temperature at 71°N

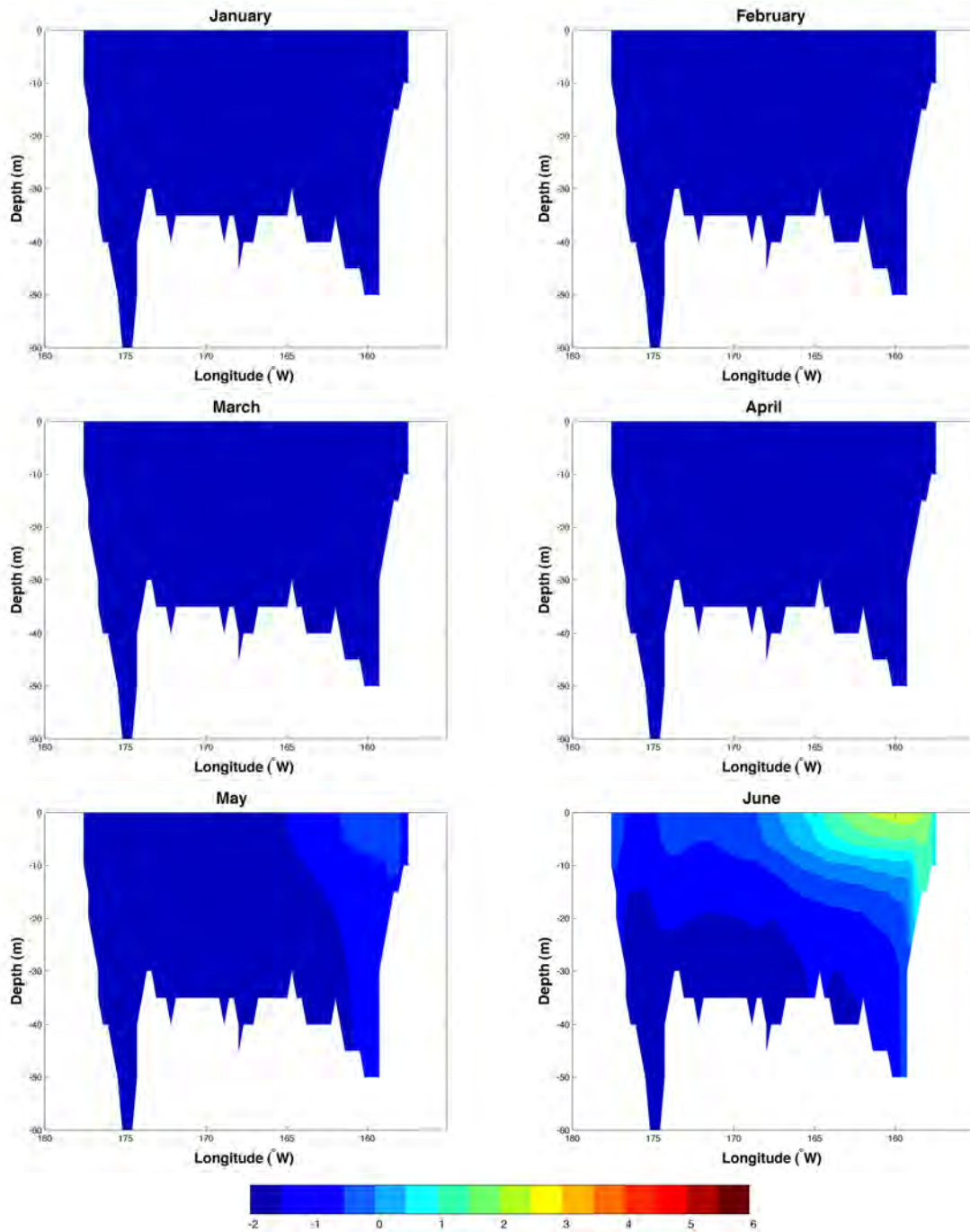


Figure 33: Hindcast monthly mean temperatures at 71°N in the Chukchi Sea. Color scale varies from -2 to $+6^{\circ}\text{C}$.

A.9 Vertical cross-sections of temperature at 71°N

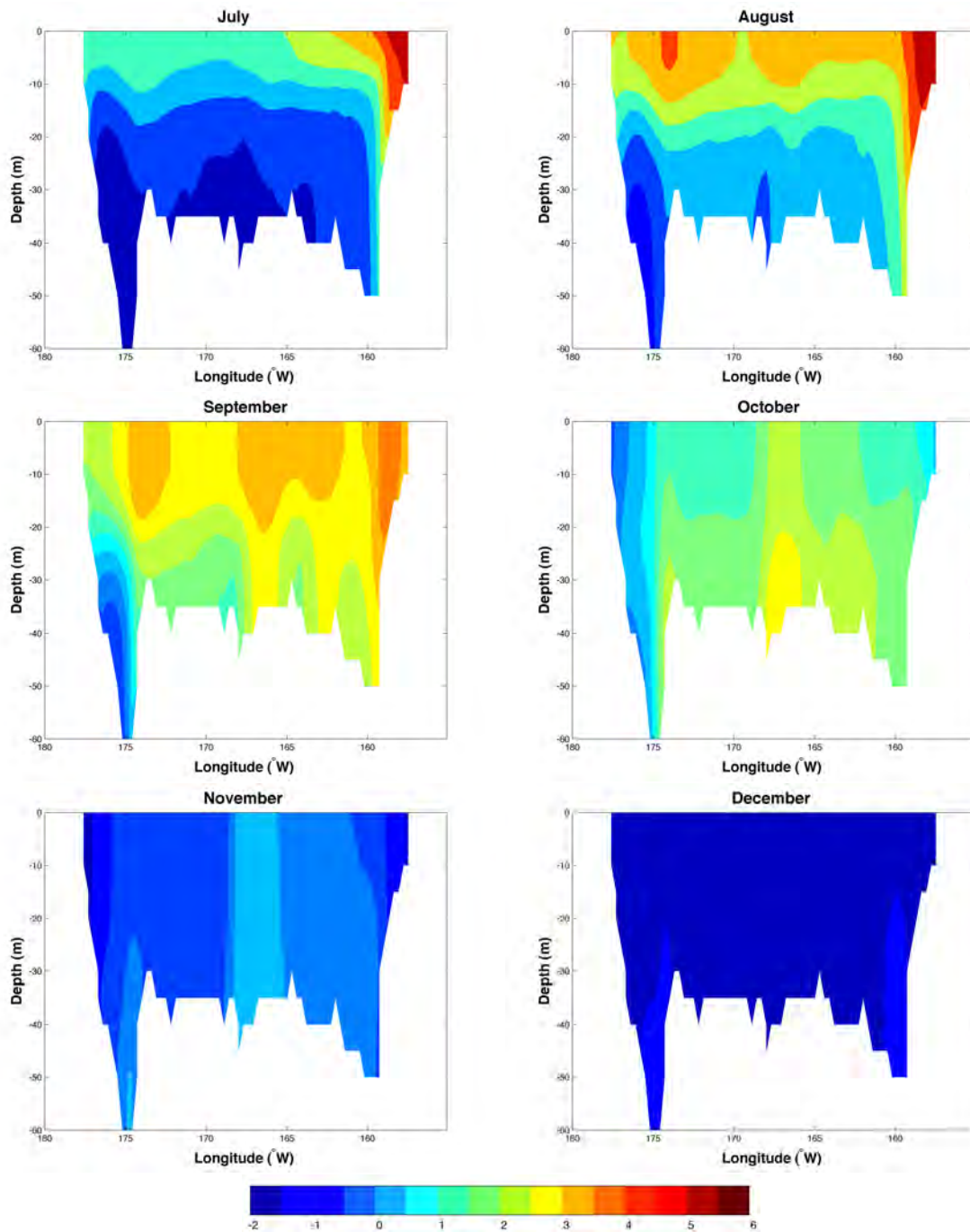


Figure 33: Hindcast monthly mean temperatures at 71°N in the Chukchi Sea. Color scale varies from -2 to +6°C (Continued).

A.10 Vertical salinity cross-sections at 71°N

A.10 Vertical salinity cross-sections at 71°N

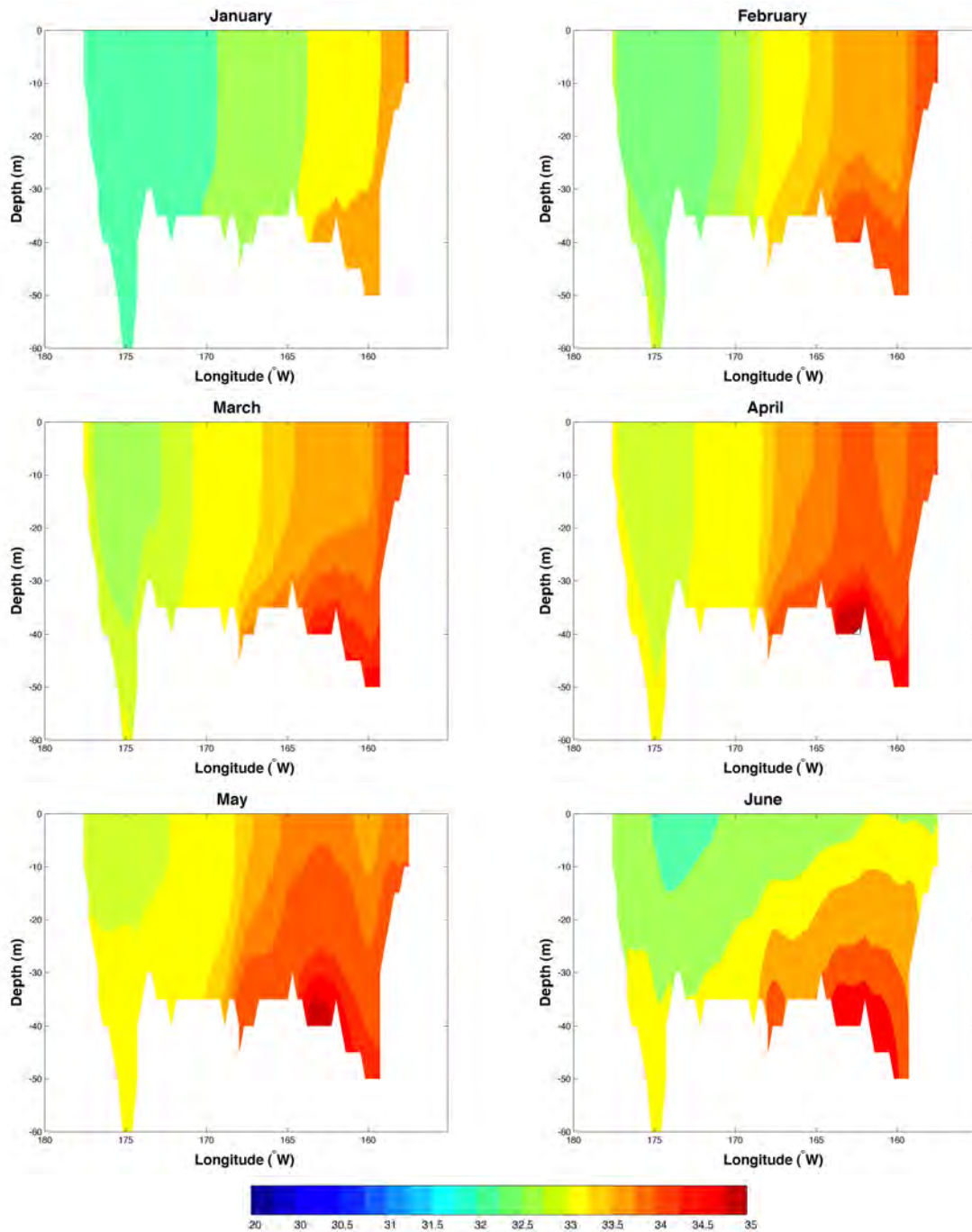


Figure 34: Hindcast monthly mean salinity at 71°N in the Chukchi Sea. Color scale varies from 20 to 35.

A.10 Vertical salinity cross-sections at 71°N

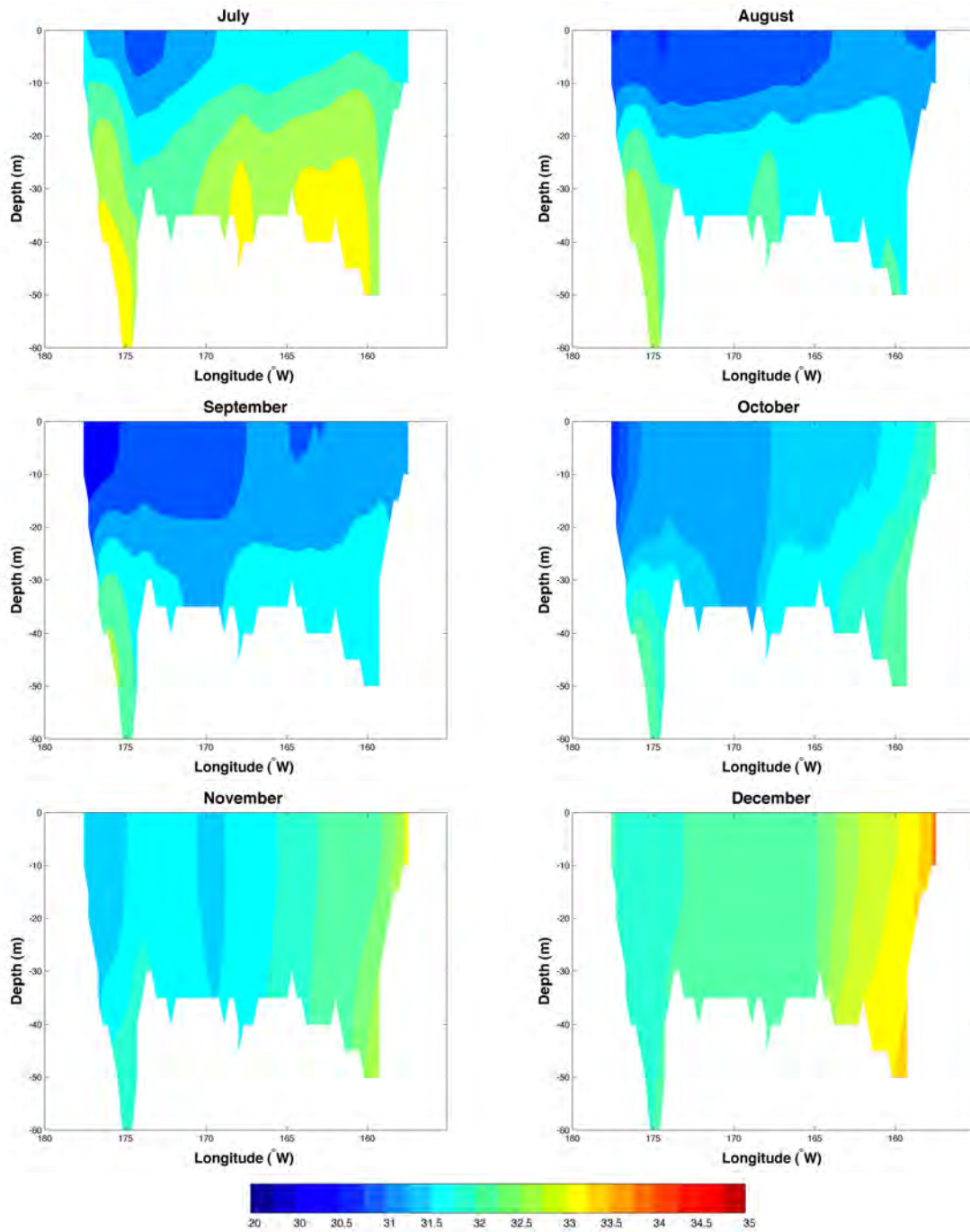


Figure 34: Hindcast monthly mean salinity at 71°N in the Chukchi Sea. Color scale varies from 20 to 35 (Continued).

References

- Aagaard, K. (1984), The beaufort undercurrent, in *The Alaskan Beaufort Sea: Ecosystems and Environment*, edited by P. W. Barnes, D. M. Schell, and E. Reimnitz, pp. 47–71, Academic Press, New York.
- Aagaard, K. (1988), Current, ctd, and pressure measurements in possible dispersal regions of the chukchi sea, outer continental shelf environmental research program, final rep., princ. invest., *Tech. rep.*, Dept. of Commerce/Dept. of Interior, Anchorage, AK.
- Aagaard, K., and Roach (1990), Arctic ocean-shelf exchange: Measurements in barrow canyon, *J. Geophys. Res.*, *95*, 18,163–18,175.
- Aagaard, K., A. T. Roach, and J. D. Schumacher (1985), On the wind-driven variability of the flow through bering strait, *J. Geophys. Res.*, *90*, 7213–7221.
- Aagaard, K., T. J. Weingartner, S. L. Danielson, R. A. Woodgate, G. C. Johnson, and T. E. Whitledge (2006), Some controls on flow and salinity in bering strait, *Geophys. Res. Lett.*, *33*, doi:10.10292006GL026612.
- Ahlnäs, K., and G. R. Garrison (1984), Satellite and oceanographic observations of the warm coastal current in the chukchi sea, *Arctic*, *37*, 244–254.
- Barnes, P. W., D. M. Schell, E. Reimnitz, Jr., J. L. .Wise, and L. Leslie (Eds.) (1984), *The Alaskan Beaufort Sea: Ecosystems and Environments*, Academic Press, Inc., 466 pp.
- Brower, W. A., Jr., R. G. Baldwin, C. N. Williams, Jr., J. L. .Wise, and L. Leslie (1988), *Climate atlas of the outer continental shelf waters and coastal regions of Alaska, Chukchi-Beaufort Sea*, vol. III, National Climatic Data Center, Asheville, NC, 28801, 497 pp.
- Budgell, W. (2005), Numerical simulation of ice-ocean variability in the barents sea region: Towards dynamical downscaling, *Ocean Dynamics*, doi:10.1007/s10236-005-0008-3.
- Carmack, E. C., R. W. Macdonald, and J. E. Papdakis (1989), Water mass structure and boundaries in the mackenzie shelf estuary, *J. Geophys. Res.*, *94*, 18,043–19,055.
- Carton, J. A., B. S. Giese, and S. A. Grodsky (2005), Sea level rise and the warming of the oceans in the soda ocean reanalysis, *J. Geophys. Res.*, *110*, doi:10.1029/2004JC002817.
- Cavalieri, D. J., and S. Martin (1994), The contributions of alaskan, siberian, and canadian coastal polynyas to the cold halocline layer of the arctic ocean, *J. Geophys. Res.*, *99*, 18,343–18,362.
- Coachman, L. K., and K. Aagaard (1981), Re-evaluation of water transports in the vicinity of bering strait., in *The Eastern Bering Sea Shelf: oceanography and resources*, vol. 1, edited by D. W. Hood and J. A. Calder, pp. 95–110, National Oceanic and Atmospheric Administration, Washington, DC, U.S.A.
- Coachman, L. K., K. Aagaard, and R. Tripp (1975), *Bering Strait: The Regional Physical Oceanography*, University of Washington Press, Seattle.

- Codispoti, L., C. Flagg, V. Kully, and J. H. Swift (2005), Hydrographic conditions during the 2002 sbi process experiments, *Deep Sea Res. II*, *52*, 3199–3226.
- Cooper, L. W., J. Grebmeier, T. Whitledge, and T. Weingartner (1997), The nutrient, salinity, and stable oxygen isotope composition of bering and chukchi sea waters in and near bering strait, *J. Geophys. Res.*, *102*, 12,563–12,578.
- Dai, A., T. Qian, K. E. Trenberth, and J. D. Milliman (2009), Changes in continental freshwater discharge from 1948–2004, *J. Climate*, *22*, 2773–2791.
- Danielson, S., K. Aagaard, T. Weingartner, S. Martin, P. Winsor, G. Gawarkiewicz, and D. Quadfasel (2006), The st. lawrence polynya and the bering shelf circulation: New observations and a model comparison, *J. Geophys. Res.*, *111*, doi:10.1029/2005JC003268.
- Ebert, E. E., and J. A. Curry (1993), An intermediate one-dimensional thermodynamic sea ice model for investigating ice-atmosphere interactions, *J. Geophys. Res.*, *98*, 10,085–10,109.
- Egbert, G. D., and S. Y. Erofeeva (2002), Efficient inverse modeling of barotropic ocean tides, *J. Atmos. Ocean. Tech.*, *19*, 183–204.
- Fairall, C. W., E. F. Bradley, D. P. Rogers, J. B. Edson, and G. S. Young (1996), Bulk parameterization of air-sea fluxes for tropical ocean-global atmosphere couple-ocean atmosphere response experiment, *J. Geophys. Res.*, *101*, 3747–3764.
- Gawarkiewicz, G. G., and D. C. Chapman (1995), A numerical study of dense water formation and transport on a shallow, sloping continental shelf, *J. Geophys. Res.*, *100*, 4489–4507.
- Grebmeier, J. M., and C. P. McRoy (1989), Pelagic-benthic coupling on the shelf of the northern bering and chukchi seas. iii. benthic food supply and carbon cycling, *Mar. Ecol. Prog. Ser.*, *53*, 79–91.
- Guay, C. K., and K. K. Falkner (1998), A survey of dissolved barium in the estuaries of major arctic rivers and adjacent seas, *Cont. Shelf Res.*, *8*, 859–882.
- Hansell, D., T. E. Whitledge, and J. J. Georing (1993), Patterns of nitrate utilization and new production over the bering-chukchi shelf, *Cont. Shelf Res.*, *13*, 601–627.
- Hunke, E. C. (2001), Viscous-plastic sea ice dynamics with the evp model: linearization issues, *J. Comp. Phys.*, *170*, 18–38.
- Hunke, E. C., and J. K. Dukowicz (1997), An elastic-viscous-plastic model for sea ice dynamics, *J. Phys. Oceanogr.*, *27*, 1849–1868.
- Johnson, W. R. (1989), Current response to wind in the chukchi sea: A regional coastal upwelling event, *J. Geophys. Res.*, *94(C2)*, 2057–2064, doi:10.1029/JC094iC02p02057.
- Kozo, T. L. (1980), Mountain barrier baroclinicity effects on surface winds along the alaskan arctic coast, *Geophys. Res. Lett.*, *7(5)*, 377–380.

- Kozo, T. L. (1982a), An observational study of sea breezes along the alaska beaufort sea coast, *J. Appl. Meteor.*, *21*, 891–905.
- Kozo, T. L. (1982b), A mathematical model of sea breezes along the alaska beaufort sea coast, *J. Appl. Meteor.*, *21*, 906–924.
- Kozo, T. L. (1984), Short term prediction (newcasting) of net daily sea ice movement in the bering strait with a mesoscale meteorological network, *Tech. rep.*, U.S. Dep. of COMmer., NOAA, OCSEAP Final Rep.
- Kwok, R., G. F. Cunningham, M. Wensnahan, I. Rigor, H. J. Zwally, and D. Yi (2009), Thinning and volume loss of the arctic ocean sea ice cover: 2003–2008, *J. Geophys. Res.*, *114*, C07005, doi:10.1029/2009JC005312.
- Large, W. G., and S. G. Yeager (2008), The global climatology of an interannually varying air-sea flux data set, *Clim. Dyn.*, *33*, 341–364, doi:10.1007/s00382-0008-0441-3.
- Large, W. G., J. C. McWilliams, and S. C. Doney (1994), Oceanic vertical mixing: a review and a model with a nonlocal boundary layer parameterization, *Rev. Geophys.*, *32*, 363–403.
- Liu, A. K., C. Y. Peng, and T. J. Weingartner (1994), Ocean-ice interaction in the marginal ice zone using sar, *J. Geophys. Res.*, *99*, 22,391–22,400.
- Macdonald, R. W., and E. C. Carmack (1991), The role of large-scale under-ice topography in separating estuary and ocean on an arctic shelf, *Atmosphere-Ocean*, *29*, 37–51.
- Macdonald, R. W., E. C. Carmack, F. A. McLaughlin, K. Iseki, D. M. Macdonald, and M. C. O'Brien (1989), Composition and modification of water masses in the mackenzie shelf estuary, *J. Geophys. Res.*, *94*, 18,057–18,070.
- Macdonald, R. W., E. C. Carmack, F. A. McLaughlin, K. K. Falkner, and J. H. Swift (1999), Composition and modification of water masses in the mackenzie shelf estuary, *Geophys. Res. Lett.*, *26*(15), 2223–2226.
- Marchesiello, P., J. C. McWilliams, and A. Shchepetkin (2001), Open boundary conditions for long-term integration of regional oceanic models, *Ocean Modelling*, *3*, 1–20.
- Martin, S., and R. Drucker (1997), The effect of possible taylor columns on the summer ice retreat in the chukchi sea, *J. Geophys. Res.*, *102*(C5), 10,473–10,482, doi:10.1029/97JC00145.
- Maslanik, J. A., M. C. Serreze, and T. Agnew (1999), On the record reduction in 1998 western arctic sea-ice cover, *Geophys. Res. Lett.*, *26*, doi:10.1029/1999GL900426.
- Mellor, G. L., and L. Kantha (1989), An ice-ocean coupled model, *J. Geophys. Res.*, *94*, 10,937–10,954.
- Mesinger, F., and Coauthors (2006), North american regional re-analysis, *Bull. Amer. Meteor. Soc.*, *87*, 343–360.

- Moore, A. M., H. G. Arango, E. DiLorenzo, B. D. Cornuelle, A. J. Miller, , and D. J. Neilsen (2004), A comprehensive ocean prediction and analysis system based on the tangent linear and adjoint of a regional ocean model, *Ocean Modelling*, *7*, 227–258.
- Mountain, D. G., L. K. Coachman, and K. Aagaard (1976), On the flow through barrow canyon, *J. Phys. Oceanogr.*, *6*, 461–470.
- Muench, R. D., M. G. McPhee, C. A. Paulson, and J. H. Morison (1992), Winter oceanographic conditions in the fram strait-yermaak plateau region, *J. Geophys. Res.*, *97*, 3469–3483.
- Münchow, A., and E. C. Carmack (1997), Synoptic flow and density observations near an arctic shelfbreak, *J. Phys. Oceanogr.*, *26*, 1402–1419.
- Münchow, A., T. Weingartner, and L. Cooper (1999), The summer hydrography and surface circulation of the east siberian shelf sea, *J. Phys. Oceanogr.*, *29*, 2167–2182.
- Münchow, A., E. C. Carmack, and D. A. Huntley (2000), Synoptic density and velocity observations of slope waters in the chukchi and east siberian seas, *J. Geophys. Res.*, *105*, 14,103–14,119.
- Nikolopoulos, A., R. S. Pickart, P. S. Fratantoni, K. Shimada, D. Torres, , and E. P. Jones (2009), The western arctic boundary current at 152°w: Structure, variability, and transport, *Deep Sea Res. II*, *56*, 1164–1181.
- Paquette, R. G., and R. H. Bourke (1974), Observations on the coastal current of arctic alaska, *J. Marine Res.*, *32*, 195–207.
- Paquette, R. G., and R. H. Bourke (1981), Ocean circulation and fronts as related to ice melt-back in the chukchi sea, *J. Geophys. Res.*, *86(C5)*, 4215–4230, doi:10.1029/JC086iC05p04215.
- Pickart, R. S. (2004), Shelfbreak circulation in the alaskan beaufort sea: Mean structure and variability, *J. Geophys. Res.*, *109*, doi:10.1029/2003JC001912.
- Pickart, R. S., T. J. Weingartner, S. Zimmermann, D. J. Torres, and L. J. Pratt (2005), Flow of winter-transformed water into the western arctic, *Deep Sea Res. II*, *52*, 3175–3198.
- Proshutinsky, A. Y. (1986), On the problem of calculating the storm surge fluctuations of sea level and water circulation in the chukchi sea, in *Soviet Meteorologia i Gidrologia*, pp. 54–61, Allerton Press Inc.
- Shchepetkin, A. F., and J. C. McWilliams (2005), The regional ocean modeling system (roms): A split-explicit, free-surface, topography-following coordinates oceanic model, *Ocean Modelling*, *9*, 347–404.
- Shimada, K., T. Kamoshida, M. Itoh, S. Nishino, E. Carmack, F. A. McLaughlin, S. Zimmermann, and A. Proshutinsky (2006), Pacific ocean inflow: Influence on catastrophic reduction of sea ice cover in the arctic ocean, *Geophys. Res. Lett.*, *33*, L08605, doi:10.1029/2005GL025624.

- Spall, M. A. (2007), Circulation and water mass transformation in a model of the chukchi sea, *J. Geophys. Res.*, *112*, C05025, doi:10.1029/2005JC003364.
- Spall, M. A., R. S. Pickart, P. S. Fratantoni, and A. J. Plueddemann (2008), Western arctic shelfbreak eddies: Formation and transport, *J. Phys. Oceanogr.*, *38*, 1644–1668.
- Springer, A. M., and C. P. McRoy (1993), The paradox of pelagic food webs in the northern bering sea. iii. patterns of primary production, *Cont. Shelf Res.*, *13*, 575–579.
- Steele, M., G. L. Mellor, and M. G. McPhee (1989), Role of the molecular sublayer in the melting or freezing of sea ice, *J. Phys. Oceanogr.*, *19*, 139–147.
- Steele, M., J. Morison, W. Ermold, I. Rigor, M. Ortmeyer, and K. Shimada (2004), Circulation of summer pacific halocline water in the arctic ocean, *J. Geophys. Res.*, *109*, C02027, doi:10.1029/2003JC002009.
- Umlauf, L., and H. Burchard (2003), A generic length-scale equation for geophysical turbulence models, *J. Marine Res.*, *61*, 235–265.
- Walsh, J. E., W. L. Chapman, and D. H. Portis (2009), Arctic cloud fraction and radiative fluxes in atmospheric reanalyses, *J. Climate.*, *22*, 2316–2334, doi:10.1175/2008JCLI2213.1.
- Walsh, J. J., and . Coauthors (1989), Carbon and nitrogen cycling within the bering chukchi seas: source regions for organic matter effecting aou demands of the arctic ocean., *Prog. Oceanogr.*, *22(4)*, 277–358.
- Warner, J. C., C. R. Sherwood, H. G. Arango, and R. P. Signell (2005), Performance of four turbulence closure models implemented using a generic length scale method, *Ocean Modelling*, *8*, 81–113.
- Weingartner, T. J., D. J. Cavalieri, K. Aagaard, and Y. Sasaki (1998), Circulation, dense water formation, and outflow on the northeast chukchi shelf, *J. Geophys. Res.*, *103*, 7647–7661.
- Weingartner, T. J., S. Danielson, Y. Sasaki, V. Pavlov, and M. Kulakov (1999), The siberian coastal current: A wind- and buoyancy-forced arctic coast current, *J. Geophys. Res.*, *104*, 26,697–29,713.
- Weingartner, T. J., K. Aagaard, R. Woodgate, S. Danielson, Y. Sasaki, and D. Cavalieri (2005a), Circulation on the north central chukchi sea shelf, *Deep Sea Res. II*, *52*, 3150–3174.
- Weingartner, T. J., S. Danielson, and T. C. Royer (2005b), Freshwater variability and predictability in the alaska coastal current, *Deep Sea Res. II*, *52*, 169–192.
- Weingartner, T. J., S. L. Danielson, J. L. Kasper, and S. R. Okkonen (2009), Circulation and water property variations in the nearshore alaskan beaufort sea, final Report, OCS Study MMS 2005-028, 155pp.

- Winsor, P., and D. C. Chapman (2002), Distribution and interannual variability of dense water production from coastal polynyas on the chukchi shelf, *J. Geophys. Res.*, *107*(C7), doi:10.1029/2001JC000984.
- Winsor, P., and D. C. Chapman (2004), Pathways of pacific water across the chukchi sea: A numerical model study, *J. Geophys. Res.*, *109*, C03002, doi:1029/2003JC001962.
- Woodgate, R. A., K. Aagaard, and T. Weingartner (2005), Monthly temperature, salinity, transport variability for the bering strait throughflow, *Geophys. Res. Lett.*, *32*, L04601, doi:10.1029/2004GL021880.
- Woodgate, R. A., K. Aagaard, and T. Weingartner (2006), Interannual changes in the bering strait fluxes of volume, heat and freshwater between 1991 and 2004, *Geophys. Res. Lett.*, *33*, doi:10.1029/2006GL026931.



The Department of the Interior Mission

As the Nation's principal conservation agency, the Department of the Interior has responsibility for most of our nationally owned public lands and natural resources. This includes fostering the sound use of our land and water resources, protecting our fish, wildlife and biological diversity; preserving the environmental and cultural values of our national parks and historical places; and providing for the enjoyment of life through outdoor recreation. The Department assesses our energy and mineral resources and works to ensure that their development is in the best interests of all our people by encouraging stewardship and citizen participation in their care. The Department also has a major responsibility for Americal Indian reservation communities and for people who live in island communities.

The Bureau of Ocean Energy Management

The Bureau of Ocean Energy Management (BOEM) works to manage the exploration and development of the nation's offshore resources in a way that appropriately balances economic development, energy independence, and environmental protection through oil and gas leases, renewable energy development and environmental reviews and studies.

www.boem.gov

